Title
Design, Fabrication, and Characterization of a High-Frequency Microwave Cavity for HAYSTAC

Author
Simanovskaia, Maria

Publication Date
2020

Peer reviewed|Thesis/dissertation

Design, Fabrication, and Characterization of a High-Frequency Microwave Cavity for HAYSTAC

by

Maria Simanovskaia

A dissertation submitted in partial satisfaction of the

requirements for the degree of

Doctor of Philosophy

in

Engineering - Nuclear Engineering

in the

Graduate Division

of the

University of California, Berkeley

Committee in charge:

Professor Karl van Bibber, Chair
Professor Lee Bernstein
Professor Surjeet Rajendran

Fall 2019

Design, Fabrication, and Characterization of a High-Frequency Microwave Cavity for HAYSTAC

Abstract

Design, Fabrication, and Characterization of a High-Frequency Microwave Cavity for HAYSTAC

by

Maria Simanovskaia

Doctor of Philosophy in Engineering - Nuclear Engineering

University of California, Berkeley

Professor Karl van Bibber, Chair

The nature of dark matter is one of the most outstanding mysteries in science today. Possibilities for its composition range from black holes to heavy particles that can be detected by their collisions with atomic nuclei to light particles that act like a coherent field. Sensitive experiments have not yet been able to detect dark matter. A case can be made that the most promising dark matter candidate is the axion, which was invented to solve the strong charge-parity problem in the standard model of particle physics. If the axion exists, it could be produced in abundance and constitute a major component of dark matter.

In the presence of a magnetic field, axions will be converted to an oscillating electromagnetic field with a frequency approximately corresponding to the axion mass. We can detect this electromagnetic field as a power excess spectrally coincident with the resonance of a microwave cavity. Each microwave cavity can provide good sensitivity in the search for axions over a limited frequency range, but we must consider new technologies to probe the full axion parameter space in a reasonable amount of time. Both as a testbed for innovative cavity and amplifier concepts and as a data pathfinder for higher frequencies, the Haloscope at Yale Sensitive to Axion Cold dark matter (HAYSTAC) was the first cavity experiment to use a dilution refrigerator and commission a squeezed-state receiver to circumvent the Standard Quantum Limit. The HAYSTAC Phase I and II cavity is a cylinder with an internal rod that rotates off-center and tunes the mode-of-interest resonance frequency between 3.4 and 5.8 GHz in a volume of 1.5 L. Recent theoretical work favors axions between 4 and 12 GHz.

I examined various cavity designs to access higher frequencies in this range and determined that a seven-rod cavity design would be optimal with a volume of 1.7 L for a frequency range between approximately 5.5 and 7.5 GHz. I designed this seven-rod cavity, constructed it, and characterized it in detail for use on HAYSTAC. My cavity design allows access to this well-motivated axion mass range with high sensitivity by increasing accessible frequencies without sacrificing performance. This seven-rod concept can be extended to higher frequencies.

To my family

Contents

List of Figures

List of Tables

Acknowledgments

I am grateful for the numerous people who have been instrumental in making graduate school a challenging, yet positive, experience.

Thanks to my advisors and committee members! Karl van Bibber, thank you for your guidance, encouragement, and optimism. Surjeet Rajendran and Lee Bernstein, thank you for your interest and contribution. Dmitry Budker, thank you for setting my scientific foundation as an undergraduate in your lab and continuing to support me in graduate school.

Thanks to the HAYSTAC collaboration! Thank you to the talented younger students with whom I have had the pleasure of working, most notably Isabella Urdinaran, Alex Droster, and Heather Jackson. Bella, Alex, and Heather, this work would have taken infinitely longer to finish without you. Nicholas Rapidis, thank you for entertaining and informative discussions and for reading this thesis, twice. Sami Lewis, thank you for introducing me to numerical simulations. Thanks as well to the rest of the HAYSTAC PIs, postdocs, and graduate students, including Kelly Backes, Ben Brubaker, Sid Cahn, Yulia Gurevich, Al Kenany, Steve Lamoreaux, Alex Leder, Konrad Lehnert, Maxime Malnou, Reina Murayama, Dan Palken, Danielle Speller, and Ling Zhong.

Thanks to the people who helped make the seven-rod cavity a reality! Jesse Lopez provided exceptional advice and support with precision machining, Ed Chubak machined most of the cavity components and adjusted designs as necessary, Emilio Nanni and Andy Haase made the copper plating and baking possible. Also thanks to members of the materials group in the nuclear engineering department who are always available to cut alumina axles, including David Frazer, Joey Kabel, and Jeff Graham.

Thanks to friends, roommates, and even some of their families, who kept me in good spirits and supported me throughout the duration of graduate school! It's impossible to list you all, but here's a start: Mauricio Ayllon Unzueta, Nick Brickner, Jorge Carrera, Neetha Iyer, Ishak Johnson, Joey Kabel, Leo Kirsch, Austin Lo, Hannah Trumbo, Andrew Voyles, and Cory Waltz. Milos Atz, James Kendrick, and Sandra Bogetic, thank you for providing motivation and joining me in writing. Mark Kowarsky, thank you for your patience and help throughout these past few years.

Thanks to my family! Natalia and Dmitri, thank you for supporting, encouraging, and comforting me throughout my life. I would have had a hard time doing this without you. Anna, thank you for fulfilling and exceeding your role as my sister. Nina Okuneva, thank you for the inspiration. Thanks to my family and friends in Russia for always reminding me that I also have a home there.

The work presented here was supported under the auspices of the National Science Foundation, under grant PHY-1607417, and the Heising-Simons Foundation under grant 2016-044.I am personally grateful to have been supported by the Berkeley Fellowship and the National Science Foundation Graduate Research Fellowship Program under grant DGE-1745016.

Chapter 1

Structure of this thesis

I begin by introducing the context for my thesis work in Ch. 2. Section 2.1 describes the strong charge-parity problem in the standard model of particle physics and outlines a few reasons for the existence of dark matter. Then, Sec. 2.2 presents the axion solution to the strong charge-parity problem and characteristics of the proposed particle. Section 2.3 describes astrophysical limits on the axion mass, and Sec. 2.4 outlines experiments working towards setting further limits on the axion mass. Finally, Sec. 2.5 describes the Haloscope at Yale Sensitive to Axion Cold dark matter (HAYSTAC), for which the following cavities were designed.

In Ch. 3, I focus on resonant microwave cavities. First, Sec. 3.1 discusses these modes in the context of the cavity figure of merit. Then, Sec. 3.2 describes the various resonant modes in cylindrical cavities that are characterized by the profiles of their electric and magnetic fields. The cavity figure of merit depends on the cavity quality factor, volume, and resonant mode form factor, which are the cavity-related characteristics that affect the HAYSTAC scan rate. Section 3.3 introduces the approximations and simulations we perform to model and analyze cavity designs. Finally, Sec. 3.4, Sec. 3.5, and Sec. 3.6 present one-rod, two-rod, and distributed Bragg resonator cavity designs, respectively, analyzed in the context of the cavity figure of merit.

In Ch. 4, I present detailed design decisions of a cavity with seven rods, six of which rotate symmetrically away from their innermost position. Section 4.1 describes the design details and manufacturing process of this seven-rod cavity. Then, Sec. 4.2 presents results from testing this seven-rod design throughout the tuning range of the mode-of-interest.

In Ch. 5, I review the presented information and discuss future work.

Chapter 2

Motivation and status of axion searches

In the following sections, I briefly describe the motivation for the existence of the axion (Sec. 2.1 and Refs. [1, 2]), axion interactions (Sec. 2.2 and Ref. [3]), the astrophysical bounds for axions (Sec. 2.3 and Ref. [4]), and the current status of axion searches (Sec. 2.4 and Ref. [5, 6]). In the final section of this chapter, I give context for my dissertation work by introducing relevant details of a specific axion search (Sec. 2.5).

2.1 Motivation

Dark matter

Initial hints of dark matter appeared in the 1930s, when Jan Oort, Horace Babcock, and Fritz Zwicky observed rotation speeds of the Milky Way galaxy, Andromeda galaxy (also known as M31), and Coma galaxy cluster, respectively [7]. This initial evidence was confirmed and more generally accepted in the 1960's when Vera Rubin performed rigorous spectroscopic measurements of the Andromeda rotational velocities [8]. These works showed that objects far from the center of the rotating disk are traveling at a speed much higher than we expected. We expected an object rotating in an orbit of radius r around a collection of luminous objects of mass $M\left(r_{\mathrm{MAX}}\right) = 4\pi \int_0^{r_{\mathrm{MAX}}} \rho\left(r\right) r^2\, dr$, where r_{MAX} is the approximate distance at which the luminous matter ends, to have velocity

$$v \sim \sqrt{\frac{GM}{r}}, \tag{2.1}$$

where G is the gravitational constant. When $r > r_{\mathrm{MAX}}$, M stays constant and r increases so v should decrease significantly. Instead, we find that v plateaus and the object moves faster that we predicted. Figure 2.1a shows rotation curves of the dwarf spiral galaxy NGC 6503 that we expect from the visible disk components, the gas, and a possible dark matter halo,

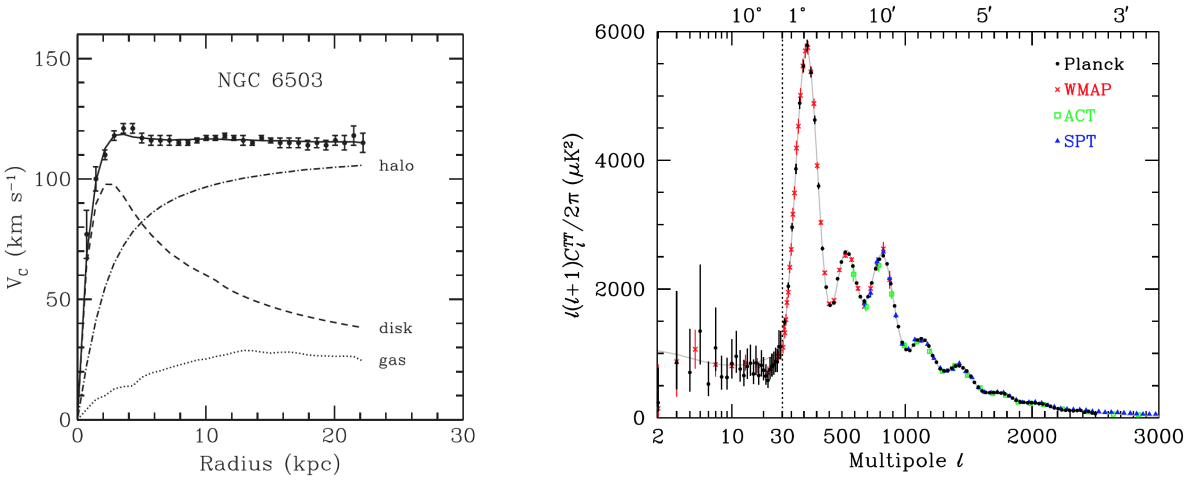

Figure 2.1: (a) Examples of expected and measured galactic rotation curves: dashed curve from visible disk components, dotted curve from gas, and dash-dot curve from a possible dark matter halo. Data points and uncertainties come from measured rotation velocities of the field dwarf spiral galaxy NGC 6503 [9]. (b) CMB temperature anisotropy [10]. Curve is best-fit Planck ΛCDM model.

which add up to the observed rotation curve. The presence of a dark matter halo in the galaxy explains the discrepancy between measured rotation curves and those expected from visible matter.

After rotation curves provided the preliminary evidence for missing matter in the universe, other types of observations supported this hypothesis including: gravitational lensing, Big Bang nucleosynthesis, and the Cosmic Microwave Background (CMB). Gravitational lensing occurs when large masses in the universe act as convex lenses by bending light towards themselves. A larger amount of mass has a larger effect on the traveling light. We observe more gravitational lensing than we expect from the visible mass distributions, which makes us believe that there is some dark matter making up the missing mass. Understanding Big Bang nucleosynthesis and the CMB requires a basic understanding of the history of the universe and can give us more insight into the amount of mass in the universe and a few other concepts.

The universe begins with the Big Bang. A broadly-accepted idea for the first few moments is inflation because it explains the smoothness of the universe and the primordial density fluctuations, which eventually contribute to structure formation. After inflation, the universe expands and cools. At $T \sim 1\,\mathrm{MeV}$ ($t = 1\,\mathrm{s}$), temperature and density conditions allow Big Bang nucleosynthesis; protons and neutrons fuse together to create light nuclei. The ratios of light nuclei formed in the first three minutes are determined by the early universe conditions. Based on these ratios, we know that there is much more non-baryonic matter than baryonic

matter in the universe, so dark matter must be non-baryonic. Baryons are particles that are composed of an odd number of quarks. At $T \sim 1$ eV ($t = 50,000$ years), the universe reaches a state of matter-radiation equality. After this time, the universe becomes matter-dominated and cool enough to allow for gravitational structure formation. At $T \sim 0.3$ eV ($t = 380,000$ years), the universe becomes transparent when electrons and nuclei bind to form neutral atoms in a process called recombination. The CMB originates from this period, and its power spectrum gives us information on the conditions of the early universe.

In the present day, we can measure the temperature $T(\theta, \phi)$ of the CMB all around us. The CMB spectrum is that of a blackbody at 2.7 K, which corresponds to $T \sim 0.23$ meV ($t = 13.7$ billion years). There are slight deviations $\mathcal{O}(10^{-5})$ from the average temperature. We can quantify these anisotropies by expanding the CMB thermal behavior as spherical harmonics Y_{lm} with amplitudes a_{lm}:

$$\frac{\delta T}{T}(\theta, \phi) = \sum_{lm} a_{lm} Y_{lm}(\theta, \phi), \tag{2.2}$$

where l identifies the angular size and m describes the angular orientation of a fluctuation mode. We express amplitude variances as $C_l \equiv \left\langle |a_{lm}|^2 \right\rangle \equiv \frac{1}{2l+1} \sum_{m=-l}^{l} |a_{lm}|^2$. Since the temperature fluctuations are gaussian, the CMB information can be summarized by the power spectrum. The power summed over all m at each l is $(2l+1) C_l / (4\pi)$. Fig. 2.1b shows this power summed in the temperature-temperature correlation spectrum C_l^{TT}. The plot also shows a best-fit model, which is determined by eight parameters including the baryon density Ω_b and the matter density Ω_m. The Planck collaboration recently determined $\Omega_b = 0.0486 \pm 0.0010$ and $\Omega_m = 0.3089 \pm 0.0062$ [11], so there must exist in the universe $\Omega_m - \Omega_b$ non-baryonic dark matter.

These observations give information about the approximate quantity of non-baryonic dark matter, but do not specify its non-gravitational interactions. The Weakly-Interacting Massive Particle (WIMP) has been a popular candidate since it is favored by supersymmetry and would be thermally produced in the correct abundance with the expected cross-section. However, many sensitive experiments have recently excluded most of the parameter space and came close to reaching an irreducible background, i.e. solar neutrinos. Since excitement is shifting away from WIMPs, other dark matter candidates are gaining popularity.

Strong charge-parity (CP) problem

There exists a term in the QCD Lagrangian, predicted in part by the nontrivial topological structure of the QCD ground state (QCD vacuum is characterized by θ_{QCD}) and in part by the nontrivial phase of the quark mass matrix M_q:

$$\mathcal{L}_{\bar{\theta}} = \bar{\theta} \frac{\alpha_s}{8\pi} G_b^{\mu\nu} \tilde{G}_{b\mu\nu}, \tag{2.3}$$

where $\bar{\theta} \equiv \theta_{QCD} + \arg\det M_q$ is expected to be $\mathcal{O}(1)$ [12], $\alpha_s = g_s^2/4\pi$ is the fine structure constant of strong interactions, and $G_b^{\mu\nu}$ is the color field strength tensor with dual $\tilde{G}_{b\mu\nu} = \frac{1}{2}\epsilon_{\mu\nu\rho\sigma} G_b^{\rho\sigma}$ [4].

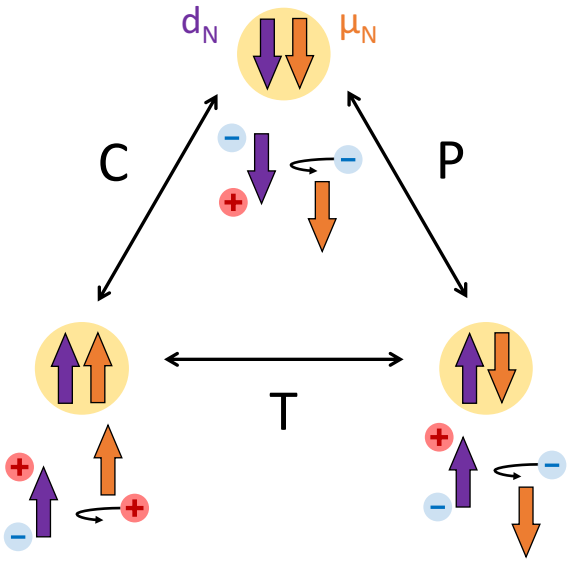

Figure 2.2: Electric and magnetic dipole moments, d_N and μ_N, respectively, under transformations of charge conjugation C, parity transformation P, and time reversal T. The CPT theorem states that all physical phenomena are symmetric under simultaneous transformations of C, P, and T.

Since the $\mathcal{L}_{\bar{\theta}}$ term in Eq. 2.3 is CP-odd, it leads us to expect some violation of the CP symmetry in the strong interaction, which is determined by the value of $\bar{\theta}$. Specifically, this strong CP symmetry violation will manifest itself in a nontrivial neutron electric dipole moment, as illustrated in Fig. 2.2. If the neutron has a nontrivial electric dipole moment, applying C and P transformations anti-aligns its electric and magnetic dipole moments compared to the original state, violating strong CP symmetry. The theory predicts a neutron electric dipole moment of

$$d_N = \frac{e}{m_N^2} \frac{m_u m_d}{m_u + m_d} \bar{\theta} \sim 10^{-16}\, \bar{\theta}\, e \cdot \text{cm [13]}, \tag{2.4}$$

where $\bar{\theta}$ is from Eq. 2.3, e is the electron charge, and m_N, m_u and m_d are the neutron, up, and down quark masses, respectively. The current experimental upper-bound on the neutron electric dipole moment is $3 \times 10^{-26}\, e \cdot \text{cm}$ [14]. Given the dependence of d_N on $\bar{\theta}$ in Eq. 2.4, this experimental evidence imposes that $\bar{\theta} \lesssim 10^{-10}$. We expect $\bar{\theta} \sim \mathcal{O}(1)$ since the standard model allows $0 \leq \bar{\theta} \leq 2\pi$. The strong CP problem is the lack of explanation for this fine-tuning of $\bar{\theta}$.

2.2 The axion

Roberto Peccei and Helen Quinn proposed in 1977 the Peccei-Quinn (PQ) mechanism to solve the strong CP problem [15, 16]. The PQ mechanism adds a $U(1)_A$ symmetry to

the standard model, which is spontaneously broken at a scale f_a. This new spontaneously-broken symmetry allows us to consider $\bar{\theta}$ as a dynamic variable with a classical potential that is minimized by $\bar{\theta} = 0$ instead of as a fixed parameter. The presence of this dynamic field introduces a term $\mathcal{L}_a$ to cancel the CP-violating $\mathcal{L}_{\bar{\theta}}$ in Eq. 2.3:

$$\mathcal{L}_a = \frac{1}{2}\left(\partial_\mu a\right)^2 - \frac{\alpha_s}{8\pi}\frac{a}{f_a}G\tilde{G}. \tag{2.5}$$

Steven Weinberg [17] and Frank Wilczek [18] realized the proposed mechanism leads to a new light pseudoscalar Nambu-Goldstone boson particle called the axion[1], associated with the spontaneously-broken symmetry.

The axion gains an effective mass through interaction with gluons:

$$\begin{aligned} m_a &= \frac{f_\pi m_\pi}{f_a}\left(\frac{1}{(1+z+w)(1+z)}\right)^{1/2} \\ &= 6\,\mathrm{eV}\,\frac{10^6\,\mathrm{GeV}}{f_a}, \end{aligned} \tag{2.6}$$

where the quark mass ratios [20] are

$$\begin{aligned} z &\equiv m_u/m_d = 0.568 \pm 0.042 \\ w &\equiv m_u/m_s = 0.0290 \pm 0.0043. \end{aligned} \tag{2.7}$$

Axion Models

The original PQWW axion model [15, 16, 17, 18] was predicted to have a symmetry breaking scale on the order of the electroweak scale $f_a \sim 250\,\mathrm{GeV}$. Since couplings are proportional to mass, this axion model predicts strong couplings. It was therefore quickly ruled out by accelerator experiments and astrophysical bounds [21].

After the original PQWW axion was ruled out, new theories were formed called invisible axion models with $f_a \gg f_{weak}$. Currently, the most popular axion models are the Kim, Shifman, Vainshtein, and Zakharov (KSVZ) model [22, 23] which allows coupling only to quarks, and the Dine, Frischler, Srednicki, and Zhitnitsky (DFSZ) model [24, 25] which allows coupling to quarks and lighter leptons.

These axion models describe a light particle with minimal coupling to the standard model. Such a particle can partially or fully make up the dark matter described in Sec. 2.1 and therefore solve both the strong CP problem and the dark matter mystery. For some intuition on the relationship between the axion's symmetry breaking scale, mass, couplings, and abundance, refer to Ref. [26].

[1]The axion, originally called the higglet by Steven Weinberg, was named eventually after a brand of detergent because it cleans up a problem with an axial current [19].

Axion interactions

Axions are predicted to couple to various particles in the standard model. Below are the predicted axion interactions that have clear experimental observables. Ref. [27] and Ref. [28] give more detailed descriptions of these interactions, which can be used to search for axions. The coupling strengths are inversely proportional to the axion decay constant; $g_{a\gamma\gamma}$, g_{aNN}, g_{aee}, $g_d \sim 1/f_a$.

- Axions couple to two photons, which is an interaction with electromagnetic fields. Currently, the most-sensitive experiments use this interaction to search for axions. The associated Lagrangian is the following:

$$\mathcal{L}_{\mathrm{EM}} = g_{a\gamma\gamma} a F_{\mu\nu} \tilde{F}^{\mu\nu} = -4 g_{a\gamma\gamma} a \vec{E} \cdot \vec{B}, \tag{2.8}$$

  where

$$g_{a\gamma\gamma} = \frac{g_\gamma \alpha}{\pi f_a} = \frac{g_\gamma \alpha}{\pi \Lambda^2} m_a,$$

  where g_γ is a model-dependent constant $\mathcal{O}(1)$. Useful benchmarks for the two most popular families of axion models, KSVZ and DFSZ, are $g_\gamma = -0.97$ and $g_\gamma = 0.36$, respectively. The uncertainties in these predicted constants span at least an order of magnitude, so the two models partially overlap in their predictions. Note that $\Lambda^2 = \sqrt{\chi} = m_a f_a$, and χ is the zero-temperature QCD susceptibility.

- Axions also couple to nucleons and nuclear spins:

$$\mathcal{L}_{\mathrm{spin}} = g_{aNN} \left(\partial_\mu a\right) \bar{N} \gamma^\mu \gamma_5 N, \tag{2.9}$$

  where N is the nucleon wave function, and γ^μ and γ_5 are the usual gamma matrices.

- Axions interact with electrons, described by the Lagrangian

$$\mathcal{L}_{\mathrm{electron}} = g_{aee} \partial_\mu a \left(\bar{e}\, \gamma_5\, \gamma^\mu\, e\right). \tag{2.10}$$

- The oscillating axion field can induce an oscillating nuclear electric dipole moment (EDM) and therefore axions also couple to the nucleon EDM operator. The Lagrangian term for this interaction is given by:

$$\mathcal{L}_{\mathrm{EDM}} = -\frac{i}{2}\, g_d\, a\, \bar{N} \sigma_{\mu\nu}\, \gamma_5\, N F^{\mu\nu}. \tag{2.11}$$

  This coupling arises from the original coupling of the QCD axion to gluons.

Axions as dark matter

For the purpose of studying axions as dark matter, we assume that axions constitute all the dark matter. We also assume that the axions constituting the cold dark matter in the galactic halo have virialized; they have settled to a state in which the virial theorem relates the time-averaged kinetic and potential energies. Their virial velocity is $\langle v^2 \rangle^{1/2} \approx 270\,\mathrm{km/s} \approx 10^{-3}c$.

Axion searches traditionally assume a local dark matter density of $\rho_a \approx 0.45\,\mathrm{GeV/cm^3}$, which is within the uncertainty of current predictions [29].

For an axion of mass $m_a \sim 20\,\mu\mathrm{eV}$, the deBroglie wavelength is $\lambda_a = h/m_a v \sim 3 \times 10^{-8}\,\mathrm{eV}^{-1} \sim 70\,\mathrm{m}$ and is approximately equal to the axion coherence length. We can also define a coherence time $\tau_a = \lambda_a/v \sim 200\,\mu\mathrm{s}$. And, finally, an axion quality factor $Q_a = m_a c^2 \tau_a / h = 1/v^2 \sim 10^6$. This quality factor measures the expected width of the frequency peak of axion field oscillations.

2.3 Bounds on axion parameter space

We can gain some knowledge about axions from their predicted interactions and astrophysical observations, some of these are mentioned below [4]. These observations place limits on the various axion coupling constants, which can be converted to constraints on the axion mass since the coupling constants are proportional to axion mass.

Globular cluster stars

A globular cluster is a gravitationally-bound collection of stars that all formed at approximately the same time. Stars with similar masses to our sun undergo various stages in their stellar evolution, including the horizontal branch and the red giant branch. If we compare the number of horizontal branch stars to the number of red giants in a globular cluster, we can gain a sense of the horizontal branch star lifetime. Axion-photon coupling accelerates the helium burning of a horizontal branch star and a larger coupling would greatly decrease the horizontal branch star lifetime. Observations of stars in globular clusters constrains axion-photon coupling [4]

$$g_{a\gamma\gamma} \leq 0.6 \times 10^{-10}\,\mathrm{GeV}^{-1}. \tag{2.12}$$

This exclusion is represented by a horizontal line in Fig. 2.3.

SN1987a

The size and duration of the detected neutrino pulse from supernova SN1987a places a limit on the axion luminosity. In the supernova, axions are theoretically emitted by nucleon bremsstrahlung, involving the axion-nucleon coupling described by Eq. 2.9. Since the coupling is proportional to the axion mass, SN1987a excludes axion masses of approximately [4]

$$10^{-2}\,\text{eV} < m_a < 10\,\text{eV}. \tag{2.13}$$

Outside of this range, axions would not interfere with the observed neutrino signals. Axions of masses below $10^{-2}\,\text{eV}$ correspond to low coupling constants and exist in the free streaming regime, in which they are emitted from the entire star volume. However, such weakly coupled axions are not created in sufficient abundance to significantly drain energy from the supernova. Axions of mass above 10 eV correspond to high coupling constants, so axion production is an efficient cooling mechanism. However, these axions exist in the trapping regime, in which they have too small of a mean free path compared to the diameter of the star and therefore can only be emitted from the surface area of an effective axion sphere. In both the free streaming and trapping regimes, axions don't interfere with the neutrino signal and therefore are not excluded by the neutrino signal observed from SN1987a. We note that higher-mass axions are constrained by other astrophysical observations.

Overclosure

The axion density is $\Omega_a \propto m_a^{-7/6}$ [30, 31, 32], and the universe would be overclosed if $\Omega_a > 1$, so we can place a lower limit on the axion mass

$$m_a \gtrsim 6\,\mu\text{eV}. \tag{2.14}$$

This mass limit corresponds to an upper limit of $f_a \sim 10^{12}\,\text{eV}$. This helped motivate the originally-favored axion mass range, where the first experiments began searching. More recent work has been done that shows it is an unnecessary bound [33, 34] due to the incorrect assumptions made about the early universe. This new result makes extremely low-mass axions more favorable. Several new axion searches are sensitive to this previously-excluded region.

2.4 Experimental searches for the axion

Axions are predicted to be relatively light particles and therefore be present in a high density in the universe. This means that it is favorable for detectors to look for an oscillating background wave behavior rather than interaction with individual particles. Each range of axion masses has a preferred method of interaction. Certain types of detectors are limited in size, since the detector size must match the axion wavelength. For example, an axion of mass $m_a \approx 20\,\mu\text{eV}$ has a wavelength of $\lambda = c/\nu_a = hc/\left(m_a c^2\right) \approx 6\,\text{cm}$.

Haloscopes

Haloscopes search for axions present in the dark matter halo. Most experiments rely on axion coupling to photons for detection, although there are some new experiments that will utilize some of the other couplings discussed in Sec. 2.2.

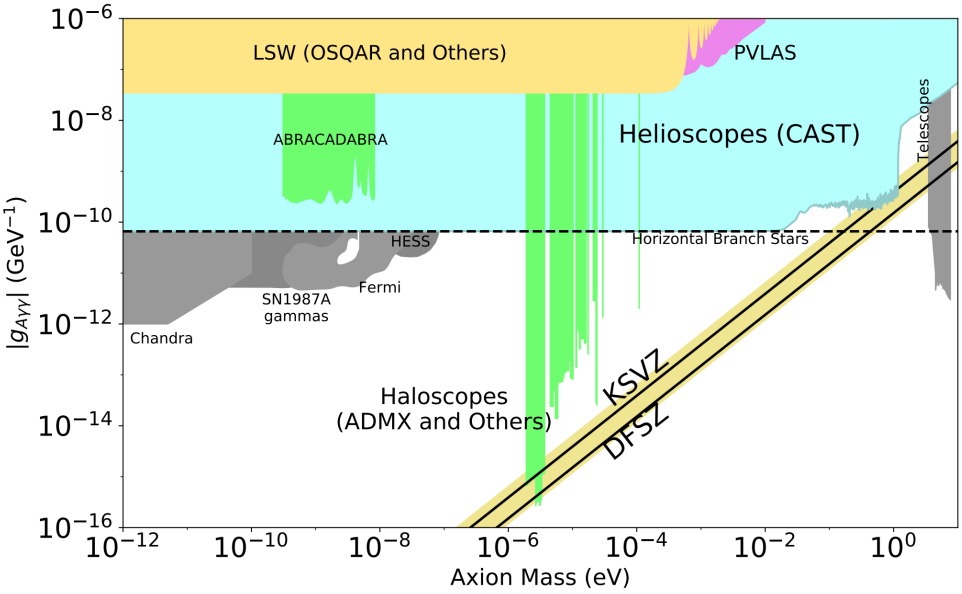

Figure 2.3: Axion-like particle parameter space and exclusions. Only the diagonal KSVZ and DFSZ lines and their uncertainty band are axion models; the rest of the space is for axion-like particles (ALPs). The plot is reproduced from Ref. [10].

The pseudoscalar nature of the axion implies that it can decay into two photons. The lifetime for this decay [4] is

$$\tau_{a\to\gamma\gamma} \sim 10^{47}\,\text{years}\left(\frac{1}{g_\gamma}\right)\left(m_a\,[\mu\text{eV}]\right)^5\,, \tag{2.15}$$

where $g_\gamma \sim \mathcal{O}(1)$. This lifetime is much greater than the age of the universe of approximately 10^{10} years, so searching for a quasi-monochromatic line corresponding to this decay with a telescope does not promise sufficient sensitivity for popular axion models at masses $m_a \lesssim 1\,\text{eV}$. Pierre Sikivie proposed to enhance the conversion probability by a Primakoff process, whereby the axion can couple to two photons, one real and one virtual. In Sikivie's concept, this takes place in a resonant microwave cavity immersed in a magnetic field [35]. The resonant conversion condition is that the axion mass is within the bandwidth of the microwave cavity at its resonance frequency. Since the axion mass is unknown, the cavity resonance frequency must be tuned to access different axion masses. A standard detection schematic is illustrated in Fig. 2.4. Several collaborations are implementing this method. These include the Axion Dark Matter eXperiment (ADMX) and Haloscope At Yale Sensitive To Axion Cold dark matter (HAYSTAC)[2], the Center for Axion and Precision Physics (CAPP) Ultra Low Temperature Axion Search in Korea (CULTASK), and the CryOgenic Resonant Group Axion CoNverter (ORGAN) [36]. These modern experiments derived from

[2]previously known as ADMX - High Frequencies (ADMX-HF)

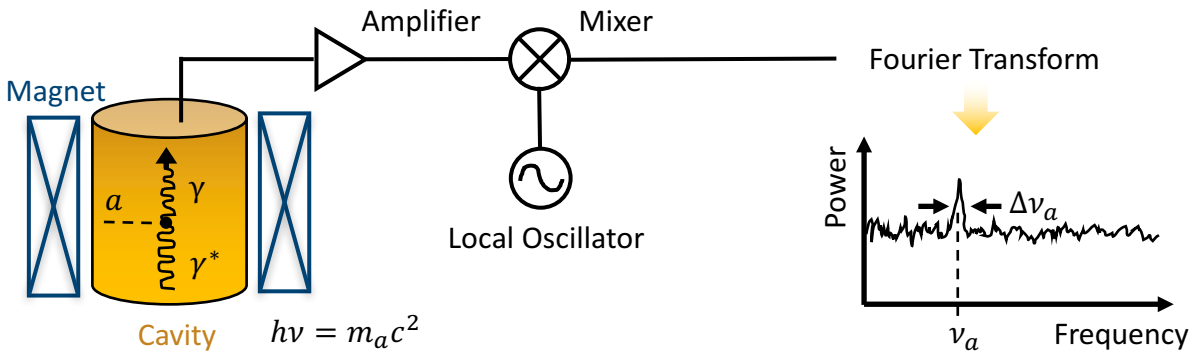

Figure 2.4: Simplified haloscope axion detection schematic of cavity experiments. The axion a interacts with a virtual photon γ^* of the magnetic field to convert the full axion energy into a real photon γ when the axion mass m_a matches the cavity resonance frequency ν. As mentioned in Sec. 2.2, the width of the axion signal is expected to be $\Delta\nu_a \approx 10^{-6}\,\nu_a$.

the early pilot experiments of the Rochester-Brookhaven-Fermilab (RBF) [37] and University of Florida (UF) [38] collaborations. These cavity experiments use similar detection techniques, but have unique designs and mostly operate at different frequency ranges. The current axion exclusions from haloscopes are shown in Fig. 2.3 in green.

The intermediate mass range $10^{-9}\,\text{eV} < m_a < 10^{-7}\,\text{eV}$ is best detected with tunable resonant LC circuits in searches such as Dark Matter Radio (DM Radio) [39] and A Broadband/Resonant Approach to Cosmic Axion Detection with an Amplifying B-field Ring Apparatus (ABRACADABRA) [40]. DM Radio uses a toroidal magnetic field, and axions within the field create an effective AC current that generates an oscillating, quasi-static effective magnetic field. This effective magnetic field induces screening currents to run on a superconducting sheath surface. A slit in the sheath with a superconducting quantum interference device (SQUID) allows detection of these screening currents. The signal is enhanced using a resonant circuit with an inductor and a tunable capacitor. These experiments can also search for hidden photons if they cut a slit in a different orientation. ABRACADABRA is using a broadband detector, while DM Radio is using the resonant approach. A comparison by equivalent circuit models shows that the resonant approach is optimal [41].

Finally, the lightest axions with masses $m_a < 10^{-9}\,\text{eV}$ are best detected by probing the axion-nucleon interactions with the Cosmic Axion Spin Precession Experiment (CASPEr) [27, 42]. There are two components to this experiment: CASPEr-wind and CASPEr-electric. Both of these aim to detect an axion-induced nuclear magnetic spin precession by ramping a magnetic field and using SQUIDS as magnetometers. CASPEr-wind uses the coupling to nuclear spins, as in Eq. 2.9. The gradient of the axion field generates an oscillating effective magnetic field, around which nucleon spins precess. CASPEr-electric takes advantage of the axion coupling to nuclear EDM, as in Eq. 2.11. The oscillating axion field causes an oscillating nuclear EDM, which in turn causes the precession of nuclear spins in the presence

of an electric field.

Many other axion searches have been proposed and are also underway. The Axion Resonant Interaction Detection Experiment (ARIADNE) [43] plans to detect the magnetic field created by axion coupling to spin in the axion mass range $0.1\,\text{meV} < m_a < 10\,\text{meV}$. The MAgnetized Disk and Mirror Axion eXperiment (MADMAX) [44] plans to use a stack of dielectric layers in a magnetic field to enhance the axion signal from interaction with photons, aiming to probe axion masses $40\,\mu\text{eV} < m_a < 200\,\mu\text{eV}$. QUaerere AXion (QUAX) [45] plans to instead study the axion coupling to electrons in magnetized samples, looking for axions of mass around $200\,\mu\text{eV}$.

Helioscopes

Helioscopes search for axions generated by the sun [46]. Helioscopes are pointed at the sun and search for axions by using a magnetic field. The most sensitive of these is the CERN Axion Solar Telescope (CAST), which set the limit on the axion-photon coupling for $m_a < 0.02\,\text{eV}$ of $g_{a\gamma\gamma} < 6.6 \times 10^{-11}\,\text{GeV}^{-1}$ [47]. To improve sensitivity at the higher frequencies, the chamber is filled with helium gas to match the dispersion relationship (energy-momentum) of a massive particle with that of a photon in a medium. This extends the path length over which coherent axion-photon conversion takes place. Specifically, one endows the photon with an effective mass, selecting the gas pressure such that the plasma frequency equals the axion mass. Another helioscope, International AXion Observatory (IAXO) [48], has been proposed and is projected to improve the helioscope exclusion.

Light-shining-through-walls (LSW)

There exist several experiments in which the axions or axion-like particles are created and detected in the laboratory. Photons traveling through a transverse magnetic field may convert to axions, which would travel through an optical barrier in the beam path. On the other side is another magnet which supports the conversion of axions back into photons, regenerating them. The Optical Search for QED Vacuum Birefringence, Axions, and Photon Regeneration (OSQAR) set the most-competitive limit using this method of $g_{a\gamma\gamma} < 3.5 \times 10^{-8}\,\text{GeV}^{-1}$ for $m_a \lesssim 0.3\,\text{meV}$ using LHC 9 T magnets [49]. This limit is shown in the axion-like particle exclusion plot in Fig. 2.3. The most advanced such experiment in preparation is Any Light Particle Search II (ALPS II) [50].

2.5 HAYSTAC

My thesis work is for HAYSTAC, which was originally conceived as an innovation testbed and data pathfinder for higher-frequency axion haloscope searches. It is a collaboration of three universities: University of California at Berkeley, University of Colorado at

Boulder, and Yale University[3]. Results from Runs 1 (approximately $5.7 - 5.8\,\mathrm{GHz}$) and 2 (approximately 5.6-5.7 GHz) of Phase I are summarized in Refs. [51, 52] with detailed analysis procedure and technical design presented in Refs. [53] and [54], respectively. In Phase I, HAYSTAC became the first cavity axion haloscope to use a dilution refrigerator and a Josephson parametric amplifier (JPA) to achieve noise performance near the Standard Quantum Limit (SQL). Photos of the experiment are shown in Fig. 2.5, and the Phase I results are reproduced in Fig. 2.6. As of late 2019, a squeezed-vacuum state reciever (SSR), incorporating two JPAs, has been commissioned and data-taking is well-underway. The SSR enables a significant speed up of data taking by circumventing the SQL. The feasibility of improving scan rate by squeezing the quantum vacuum with two JPAs has already been validated in a mock-axion set-up [55]. The microwave cavity used in Phases I and II is a copper-coated cylinder with a rod inside that can rotate off-center. The resonance frequency of our mode-of-interest is between 3.4 and 5.8 GHz with a volume of 1.5 L.

Signal power

The expected signal power in HAYSTAC is given by

$$P_{\mathrm{sig}} = \left(g_{a\gamma\gamma}^2 \frac{\hbar^3 c^3 \rho_a}{m_a^2}\right) \times \left(\frac{1}{\mu_0} B_0^2 \omega_c V C_{mn\ell} Q_L \frac{\beta}{1+\beta} \frac{1}{1+\left(2\Delta\nu_a/\Delta\nu_c\right)^2}\right), \tag{2.16}$$

where the terms in the first set of parentheses involve theoretical parameters and the terms in the second set of parentheses are determined by experimental parameters. Theoretical parameters include the model-dependent coupling constant g_γ, fine structure constant α, local dark matter density $\rho_a \approx 0.45\,\mathrm{GeV/cm^3}$ (commonly used in axion searches [56] and consistent with recent measurements [29]), and $\Lambda = 78\,\mathrm{MeV}$ encodes the dependence of axion mass on hadronic physics. The relevant experimental parameters are external magnetic field strength B_0, cavity resonance frequency $\omega_c = 2\pi\nu_c$, cavity volume V, mode-specific cavity form factor C_{nml}, cavity loaded quality factor $Q_L = Q_0/\left(1+\beta\right)$, cavity linewidth $\Delta\nu_c$, and β, which parameterizes the cavity coupling to the receiver ($\beta = 1$ corresponds to critical coupling). Cavity parameters are discussed in detail in Sec. 3.1.

Typical values for our detector are $B_0 = 9\,\mathrm{T}$, $\omega_c = 2\pi\,5\,\mathrm{GHz}$, $V = 1.5\,\mathrm{L}$, $C_{nml} = 0.5$, $Q_L = 10^4$, $\beta = 2$, $\Delta\nu_a = 5\,\mathrm{kHz}$, and $\Delta\nu_c = \nu_c/Q_L = \omega_c/\left(2\pi Q_L\right)$. Altogether, the expected power for these parameters at $g_\gamma = -0.97$ (the benchmark for KSVZ) is $P_{\mathrm{sig}} \simeq 10^{-24}\,\mathrm{W}$.

Noise considerations

The Dicke radiometer equation [57] gives our signal-to-noise ratio Σ:

$$\Sigma = \frac{P_{\mathrm{sig}}}{k_B T_{\mathrm{sys}}} \sqrt{\frac{\tau}{\Delta\nu_a}}, \tag{2.17}$$

[3]HAYSTAC is funded primarily by the National Science Foundation and the Heising Simons Foundation.

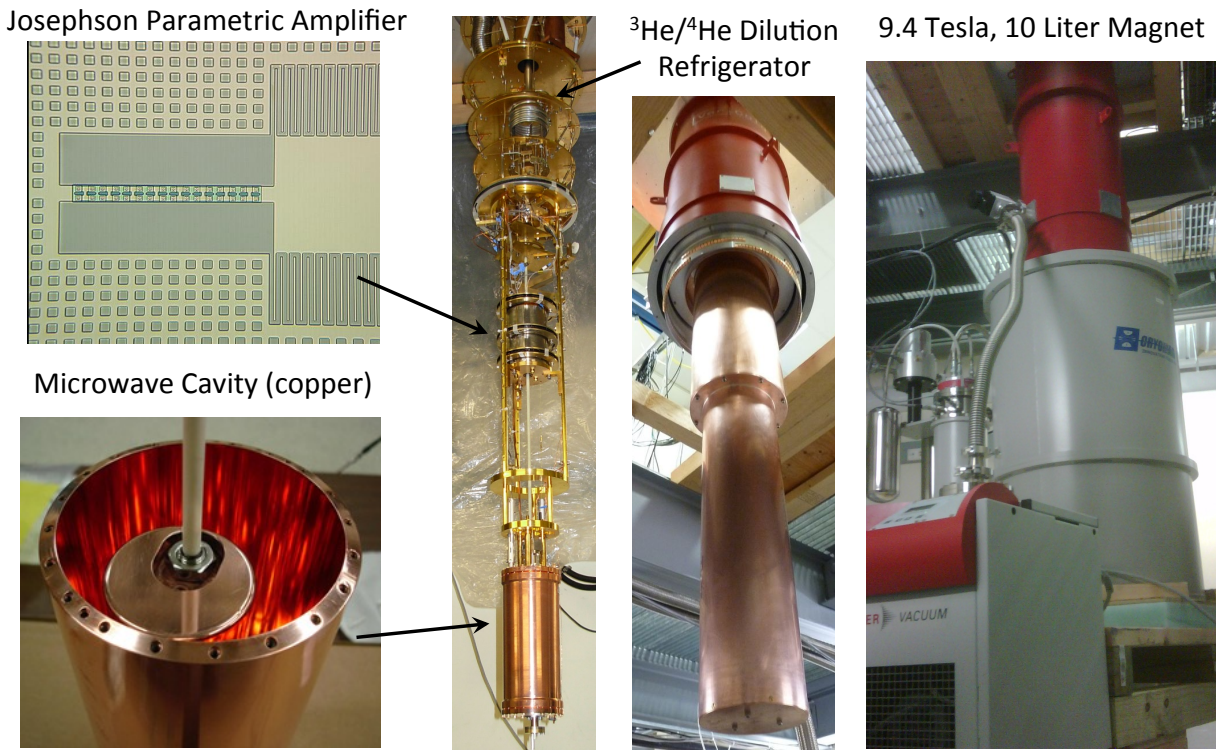

Figure 2.5: Photos of the HAYSTAC experiment in the Wright Lab in New Haven, CT. Top left is an image of the JPA, bottom left is a top-view photo of the resonant microwave cavity with its tuning rod. Moving rightwards, we see the canister housing the JPA surrounded by magnetic shielding, and the cavity at the bottom of the gold-plated gantry. This dilution refrigerator gantry is surrounded by copper thermal shields shown on the next image over, and the assembly is placed into the magnet bore. This figure is reproduced from Ref. [54].

where $T_{\rm sys}$ is the system noise temperature, τ is the integration time, and $\Delta\nu_a$ is the expected linewidth of the axion. Note that it is much more effective to increase power $P_{\rm sig}$ or decrease noise $T_{\rm sys}$ rather than to improve Σ by longer integration times. We can increase power by increasing the applied magnetic field or by improving cavity parameters, as suggested by Eq. 2.16. We can also work to decrease noise, as we are trying to do in Phase II of HAYSTAC currently by implementing a squeezed-state receiver.

For any phase-insensitive linear receiver the system noise temperature $T_{\rm sys}$ may be written

$$k_B T_{\rm sys} = h\nu N_{\rm sys} = h\nu \left(\frac{1}{e^{h\nu/k_B T} - 1} + \frac{1}{2} + N_A \right), \tag{2.18}$$

where the three additive contributions correspond respectively to a blackbody gas in equilibrium with the cavity at temperature T, the zero-point fluctuations of the blackbody gas, and the input-referred added noise of the receiver. The latter two terms combine to form the SQL. In Phase I of HAYSTAC, we used one near-quantum-limited JPA as an amplifier.

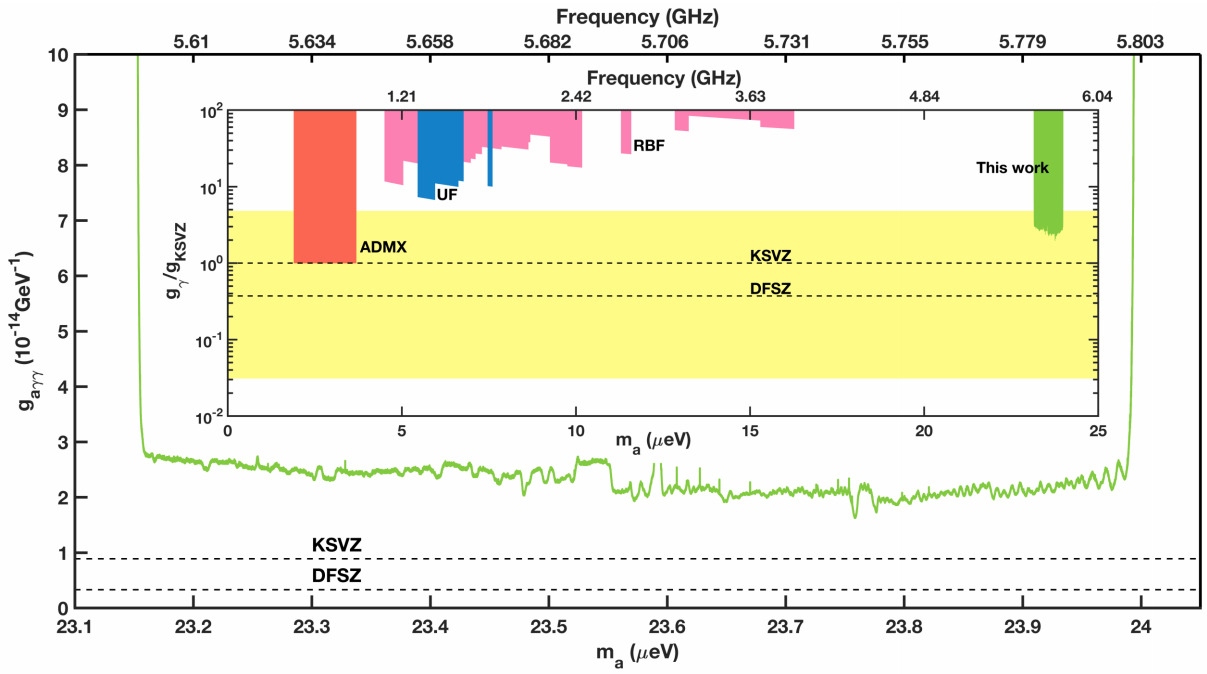

Figure 2.6: Exclusion plot from 2018 showing the Phase I HAYSTAC data. Refer to relevant articles (such as Ref. [10]) for updated results from various experiments. This plot is reproduced from Ref. [52].

In the ongoing Phase II, we are using a system of two JPAs that prepares the cavity in a squeezed vacuum state before amplifying with a second JPA, making sure that the amplified quadrature is 90° out of phase with the quadrature amplified by the first JPA. The basic squeezing configuration is illustrated in Fig. 2.7. The axion signal ϵ_a enters the cavity at a rate of κ_a, some energy leaves the cavity as losses at rate κ_l, and the electronics inject a squeezed state and measure the result at rate κ_m. The noise in our cavity comes from fluctuations of the electromagnetic field. At each frequency ω, these fluctuations can be expressed in their Fourier components as

$$\vec{E}_\omega = \vec{E}_0 \left(\hat{X} \cos \omega t + \hat{Y} \sin \omega t \right), \tag{2.19}$$

where the amplitudes of the cosine and sine components are called quadratures. They correspond to non-commuting quantum operators. The Heisenberg uncertainty principle therefore implies that the vacuum state off-cavity resonance can be represented as a circle with equal contributions in $\hat{X}$ and $\hat{Y}$ as in Fig. 2.7a. In the case with squeezing, the vacuum state is squeezed in the $\hat{Y}$ direction by the squeezer JPA, labeled as SQ, before it is injected into the cavity as in Fig. 2.7b. Then the signal accumulates, represented by the green outline in Fig. 2.7c. Then, Fig. 2.7d shows the relative sizes of the the noise and signal after they are amplified in the $\hat{X}$ direction by the amplifier JPA, labeled as AMP. In the case without squeezing, the unmodified circle of uncertainty in Fig. 2.7e is injected into the cavity. The

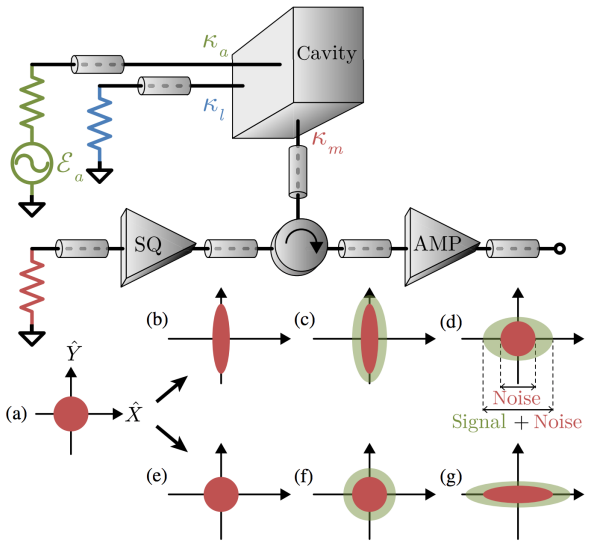

Figure 2.7: Squeezing set-up. The (a) vacuum state quadrature representation traveling through the system (b,c,d) with and (e,f,g) without squeezing is represented below the stages. The final state in the configuration (d) with squeezing has a higher signal-to-noise ratio than (g) without squeezing. This figure is reproduced from Ref. [55].

signal accumulates around this circle, giving the green outline in Fig. 2.7f. Finally, the amplifying JPA amplifies both signal and noise in the $\hat{X}$ direction, giving the configuration in Fig. 2.7g. As the illustrations show, preparing the vacuum state using a squeezer improves our signal-to-noise ratio over the non-squeezed case [55].

Scan rate

The ultimate figure of merit of our axion search is the scan rate, which incorporates the expected signal power and noise considerations, and quantifies how quickly we can scan through different frequencies at a given sensitivity

$$R \equiv \frac{\mathrm{d}\nu}{\mathrm{d}t} \approx \frac{4}{5}\frac{Q_L Q_a}{\Sigma^2}\left(g_{a\gamma\gamma}^2 \frac{\hbar^3 c^3 \rho_a}{m_a^2}\right)^2 \times \left(\frac{1}{\hbar\mu_0}\frac{\beta}{1+\beta}B_0^2 V C_{mn\ell}\frac{1}{N_{\mathrm{sys}}}\right)^2. \tag{2.20}$$

Most of these terms are recognizable from the expression of the signal power in Eq. 2.16. Using typical values for HAYSTAC, to achieve the benchmark KSVZ sensitivity $g_{a\gamma\gamma}^{\mathrm{KSVZ}}$, the Phase I scan rate would have been approximately 40 MHz/yr. Since the scan rate scales as the fourth power of the coupling constant, the scan rate would have been 600 MHz/yr to achieve twice the KSVZ sensitivity $2g_{a\gamma\gamma}^{\mathrm{KSVZ}}$.

We can improve the scan rate by buying or building a magnet with a stronger magnetic field and/or larger volume, by decreasing noise in the receiver, or by improving cavity parameters. These improvements allow us to search through a mass range more quickly, but we

are still limited by the tuning range of the cavity and amplifier electronics. The frequency range we can probe depends on the resonance frequency of the microwave cavity. Specifically, we are interested in accessing higher frequencies since recent theoretical work favors axions in the $20 - 50\,\mu\text{eV}$ range. In general, higher frequency cavities have a smaller volume and therefore suffer from a smaller expected signal power as well as an increase in operational complexity due to a higher intruder mode density. My work involves developing new cavity designs that expand the accessible frequency range while improving sensitivity. This requires me to investigate various geometries using electromagnetic simulations, prototypes, and microwave testing.

Chapter 3

Exploration of cavity designs

In the present chapter, I introduce the necessary background for understanding resonant microwave cavity design, including the cavity figure of merit relevant for HAYSTAC (Sec. 3.1), resonant cavity modes (Sec. 3.2), and the simulation tools we use to study cavities (Sec. 3.3). Then, I describe the characterization of the HAYSTAC Phase I and II cavity in the context of the cavity figure of merit (Sec. 3.4), as well as details of a few designs I considered for accessing higher frequencies (Sec. 3.5 and Sec. 3.6).

3.1 Figure of merit components

The cavity figure of merit is determined by the scan rate, as in Eq. 2.20, and is partially composed of cavity geometry and resonant mode characteristics. The components include the quality factor Q, which quantifies losses, the form factor C, which describes the alignment of the resonant mode electric field to the external magnetic field, and the cavity volume V. The scan rate depends on these quantities as

$$R \equiv \frac{d\nu}{dt} \propto Q\, C^2\, V^2. \tag{3.1}$$

HAYSTAC aims to optimize cavities for this figure of merit while considering mode purity throughout the tuning range. Each component and the resonant mode frequency can be calculated for empty cylindrical cavities and approximated for cylindrical cavities with a central conductor, as described below. For the following discussion, suppose the cavity has radius R_{cav}, height L, conductivity σ, permeability $\mu \approx \mu_0$, and vacuum permittivity ϵ_0. We choose a resonant mode with a radially-varying electric field in the longitudinal direction $\vec{E} = E(r)\hat{z}$, from which we calculate the magnetic field $\vec{H}$:

$$\vec{H} = \frac{1}{\mu}\vec{B} = \frac{1}{\mu}\frac{\vec{\nabla}\times\vec{E}}{\omega} = \frac{1}{\mu}\frac{\vec{\nabla}\times E(r)\hat{z}}{\omega} = \frac{1}{\mu\,\omega}\frac{\partial}{\partial r}E(r)\hat{\phi} = \frac{\sqrt{\mu_0\epsilon_0}}{\mu\,k_0}\frac{\partial}{\partial r}E(r)\hat{\phi} = H(r)\hat{\phi}. \tag{3.2}$$

Frequency

Each cavity geometry can support an infinite number of modes of various electric and magnetic field profiles. As we begin considering optimizing the figure of merit, we remember that the figure of merit applies to a single resonant mode with an associated resonance frequency, which is related to the axion mass by $E = m_a c^2 = h\nu$. A rule of thumb for calculating axion mass m_a from a resonance frequency f is

$$m_a\,[\mu\text{eV}] = 4.136\, f\,[\text{GHz}] \tag{3.3}$$

Changing the cavity geometry (for example, by moving a tuning rod) changes the mode frequencies. To track these changes, we can make mode maps that show mode frequencies at each cavity geometry change.

Quality factor

The quality factor of a cavity is given by the ratio of the stored energy U to the dissipated power P_d, multiplied by the resonant mode frequency ω:

$$Q = \omega\,\frac{U}{P_d}. \tag{3.4}$$

The stored energy in the cavity is proportional to the square of the electric field integrated over the cavity volume

$$\begin{aligned} U &= \frac{1}{2}\epsilon_0 \int_{\text{cavity volume}} |\vec{E}|^2\, dV \\ &= \frac{1}{2}\epsilon_0 \int_0^{R_{\text{cav}}} 2\pi r L\, |E(r)|^2\, dr. \end{aligned} \tag{3.5}$$

The power loss in the cavity is proportional to the square of the magnetic field integrated over the metallic surfaces inside the cavity. Although these surfaces realistically include contributions from the ends of the rods (the rod caps), for the purposes of these calculations, we assume that the bulk of the rod losses originate from the rod walls. Then, we have

$$\begin{aligned} P_d &= \frac{\omega\,\mu\,\delta}{4} \int_{\text{cavity surfaces}} |\vec{H}|^2\, dA \\ &= \frac{\omega\,\mu\,\delta}{4} \left(\int_{\text{cavity wall}} |\vec{H}|^2\, dA + \int_{\text{rod wall}} |\vec{H}|^2\, dA + 2\int_{\text{endcap}} |\vec{H}|^2\, dA \right) \\ &= \frac{\omega\,\mu\,\delta}{4} \left(2\pi R_{\text{cav}} L\, |H(R_{\text{cav}})|^2 + 2\pi R_{\text{rod}} L\, |H(R_{\text{rod}})|^2 + 2\int_0^{R_{\text{cav}}} 2\pi r |H(r)|^2\, dr \right), \end{aligned} \tag{3.6}$$

where the skin depth δ is the distance that electric fields are allowed to penetrate into the metallic surfaces. The classical skin depth is given by

$$\delta = \sqrt{\frac{2}{\omega\,\mu\,\sigma}}. \tag{3.7}$$

Since the conductivity σ improves with decreasing temperature, the classical skin depth is expected to improve as well. However, at sufficiently low temperatures, the skin depth reaches an asymptote. In HAYSTAC, we find that cooling the cavities from room temperature to 4 K gives an improvement of the quality factor by approximately a factor of four at a frequency around 1 GHz. For comparison, the conductivity σ improves by a factor of over a hundred in that temperature range. The classical behavior becomes invalid when the skin depth decreases below the electron's mean free path. In this regime, the skin depth depends on the electron density instead of the normal conductivity. This anomalous skin depth [58] is given by

$$\delta_a = \left(\frac{\sqrt{3}\, c^2 m_e v_F}{8\pi^2 \omega n e^2} \right)^{1/3}, \tag{3.8}$$

where m_e is the electron mass, v_F is the Fermi velocity, n is the conduction electron density, and e is the electron charge [59].

The quality factor is determined primarily by the material and geometry of the cavity, and also can vary greatly between resonant modes. Materials with a higher conductivity typically have smaller skin depths and therefore higher quality factors. The desire to have higher conductivity motivates us to plate the cavities with oxygen-free high-conductivity (OFHC) copper and anneal them for further conductivity improvement.

Form factor

The form factor is a measure of how well the electric field of the mode $\vec{E}_{nml} = \vec{E}$ aligns with the external magnetic field $\vec{B}_0 = B_0 \hat{z}$. It is given by the equation

$$C_{mnp} = \frac{\left(\int \vec{E} \cdot \vec{B}_0 \, dV \right)^2}{B_0^2 V \int \epsilon_r E^2 \, dV} = \frac{\left(\int E_z B_0 \, dV \right)^2}{B_0^2 V \int E^2 \, dV} = \frac{\left(\int E_z \, dV \right)^2}{V \int E^2 \, dV} = \frac{2\pi L \int_0^{R_{\text{cav}}} E_z(r) r \, dr}{V 2\pi L \int_0^{R_{\text{cav}}} E(r)^2 r \, dr}, \tag{3.9}$$

where V is the cavity volume not occupied by a metallic object. Earlier experiments, such as the ones performed by the RBF and UF collaborations, defined the form factor using V as the cavity volume without subtracting the space occupied by metallic objects. Although this discrepancy does not impact the overall figure of merit QC^2V^2, we must be careful comparing quoted form factor values between past experiments and those presented here.

The form factor C_{nml} is maximized when $\vec{E}_{nml} \cdot \vec{B}_0$ is maximized. Since the applied magnetic field in HAYSTAC is in the $\hat{z}$ direction, all resonant modes without electric field components in the $\hat{z}$ direction have form factors that are identically zero.

Volume

The volume in the cavity figure of merit involves the internal cavity space through which electric fields penetrate. It is the same volume V as in the form factor calculation in Eq. 3.9. In our examples, it includes the volume taken up by vacuum and dielectric materials, but

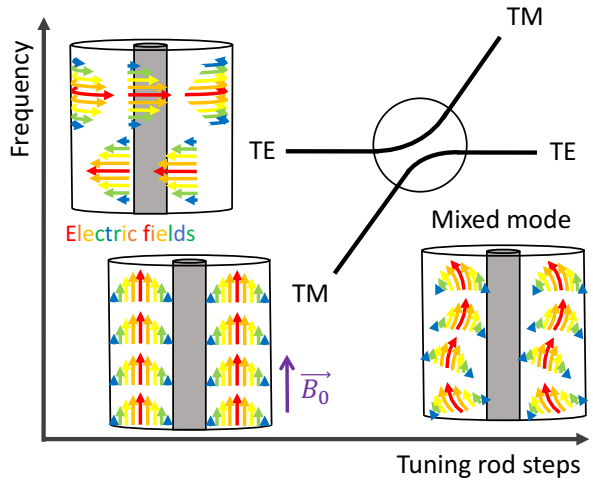

Figure 3.1: Electric field profile cartoons of a TE mode, TM mode, and a mixed mode. The small violet arrow represents $\vec{B}_0$, the external applied magnetic field. The plot shows the effect of rod rotation on resonance mode frequency. When the TE and TM modes are sufficiently close in frequency, they mix and create a mixed hybrid mode.

excludes metal pieces. Using the same mode and geometry, the volume generally decreases with increasing frequency. This volume decrease with increasing frequencies causes one of the main challenges in designing higher-frequency cavities.

Mode density

Quality factor, form factor, and volume quantitatively describe the behavior of interest of a single resonant mode at a given frequency. These quantities are useful for getting a general sense of performance across a tuning range, but if the range is full of intruder modes, it will be interrupted. Figure 3.1 shows the electric field profiles of three example resonant modes labeled "TE", "TM" mode, and "mixed mode". Out of the three, the TM mode has the highest form factor. The TM mode resonance frequency is denoted by the black curve, and the frequency increases with increasing tuning rod steps. In comparison, the TE mode resonance frequency does not change significantly. When the TE and TM mode frequencies approach each other, the two modes mix, producing two hybrid modes, in complete analogy with two-level mixing in quantum mechanics. If the mode of interest hybridizes significantly, it will be difficult or impossible to interpret the results of the experiment, thus leading to a notch in frequency coverage of the experiment. Mode density is difficult to quantify, but it is a key consideration for cavity design. As will be seen from the detailed discussion of cavity modes below, the problem of intruder mode density worsens for cavities of too large an aspect ratio L/R_{cav}; practically one is constrained to stay with cavity designs of $L/R_{\text{cav}} \sim 5$ or lower.

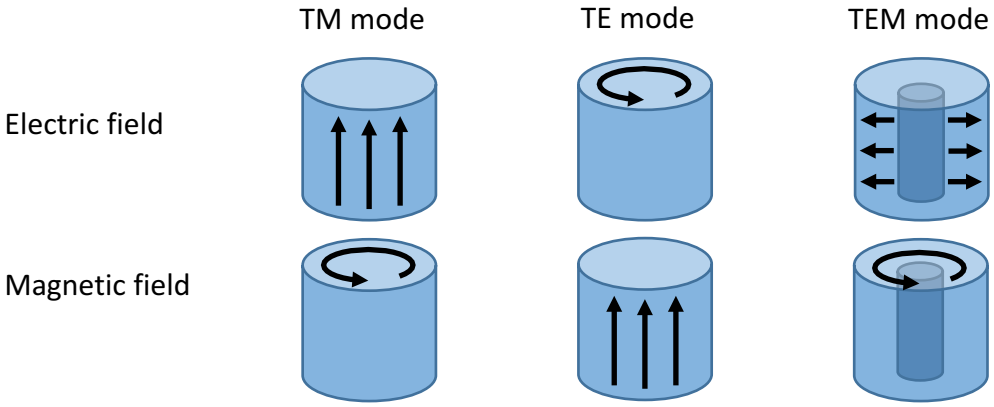

Figure 3.2: Electric and magnetic field vectors of TM, TE, and TEM modes in a cylindrical geometry, without describing magnitude. The darker profile in the TEM mode sketches is the central conductor.

3.2 Resonant cavity modes

The figure of merit quantifies the usefulness of a resonant mode in a cavity for an axion search at a certain frequency. There are many resonant modes in the cavity of various profiles. Some of these can tune by moving rods and some have approximately stationary resonance frequencies upon changing the position of the rod. HAYSTAC cavities involve central conductors and have transverse magnetic (TM), transverse electric (TE), and transverse electric and magnetic (TEM) modes. The resonant modes are characterized by the profiles of their electric and magnetic fields, summarized in Fig. 3.2. Each TE and TM mode is classified by three numbers m, n, and p that describe the variation in the azimuthal, radial, and longitudinal directions, respectively. For example, TM_{020} and TM_{011} have one extra radial node and longitudinal node, respectively, in the electric field compared to TM_{010}.

All resonant modes describe profiles of electromagnetic fields that obey the Maxwell equations and the usual boundary conditions. The Maxwell equations in vacuum are

$$\begin{aligned}
\nabla \times \vec{E}\,(\rho,\phi,z,t) &= -\frac{\partial \vec{B}\,(\rho,\phi,z,t)}{\partial t} \\
\nabla \times \vec{H}\,(\rho,\phi,z,t) &= \vec{J}\,(\rho,\phi,z,t) + \frac{\partial \vec{D}\,(\rho,\phi,z,t)}{\partial t} \\
\nabla \cdot \vec{D}\,(\rho,\phi,z,t) &= \rho \\
\nabla \cdot \vec{B}\,(\rho,\phi,z,t) &= 0,
\end{aligned} \tag{3.10}$$

where $\vec{E}$ is the electric field, $\vec{B}$ is the magnetic field, $\vec{D} = \epsilon_0 \vec{E}$, $\vec{H} = \vec{B}/\mu_0$, $\vec{J}$ is the electric current density, and ρ is the electric charge density. Near a metallic surface, we can only have normal $\vec{E}$ and tangential $\vec{B}$. This means that at a perfect electric conductor (PEC)

surface, we must have the tangential electric fields and normal magnetic fields vanish, the tangential component of magnetic field match the surface current density $\vec{j}_s$, and the normal component of electric field match the surface charge density ρ_s. These boundary conditions are respectively summarized in the following equations:

$$\begin{aligned} \hat{n} \times \vec{E} &= 0 \\ \hat{n} \cdot \vec{B} &= 0 \\ \hat{n} \times \vec{H} &= \vec{j}_s \\ \hat{n} \cdot \vec{D} &= \rho_s, \end{aligned} \tag{3.11}$$

where $\hat{n}$ is the vector normal to the PEC surface s.

In an empty cylindrical cavity, we can assume that the electric and magnetic fields have time dependence $e^{-i\omega t}$, so Eqs. 3.10 reduce to

$$\begin{aligned} \nabla \times \vec{E}\left(\rho, \phi, z\right) &= i\frac{\omega}{c}\vec{B}\left(\rho, \phi, z\right) \\ \nabla \times \vec{B}\left(\rho, \phi, z\right) &= -i\mu\epsilon\frac{\omega}{c}\vec{E}\left(\rho, \phi, z\right) \\ \nabla \cdot \vec{E}\left(\rho, \phi, z\right) &= 0 \\ \nabla \cdot \vec{B}\left(\rho, \phi, z\right) &= 0. \end{aligned} \tag{3.12}$$

We can then use the identity

$$\vec{\nabla} \times \left(\vec{\nabla} \times \vec{A}\right) = \vec{\nabla}\left(\vec{\nabla} \cdot \vec{A}\right) - \vec{\nabla}^2\vec{A}, \tag{3.13}$$

and take the cylindrical cavity to be oriented in the $\hat{z}$ direction to rewrite Eqs. 3.12 as

$$\left(\nabla^2 + \mu\epsilon\frac{\omega^2}{c^2}\right)\vec{E}\left(\rho, \phi, z\right) = \left(\frac{1}{\rho}\frac{\partial}{\partial\rho}\left(\rho\frac{\partial f}{\partial\rho}\right) + \frac{1}{\rho^2}\frac{\partial^2 f}{\partial\phi^2} + \frac{\partial^2 f}{\partial z^2} + \mu\epsilon\frac{\omega^2}{c^2}\right)\vec{E}\left(\rho, \phi, z\right) = 0. \tag{3.14}$$

The equation for $\vec{B}\left(\rho, \phi, z\right)$ is of the same form. Next, given the symmetrical geometry, we can assume

$$\vec{E}\left(\rho, \phi, z\right) = E_0 R\left(\rho\right) e^{\pm im\phi} e^{\pm ikz}\hat{z}, \tag{3.15}$$

where $k = p\pi/L$ and $p = 0,\ 1,\ 2, ...$

We plug this form into Eq. 3.14 and rearrange to obtain Bessel's differential equation

$$\rho^2\frac{\partial^2}{\partial\rho^2}R\left(\rho\right) + \rho\frac{\partial}{\partial\rho}R\left(\rho\right) + \left(\left(\omega^2\mu\epsilon - k^2\right)\rho^2 - m^2\right)R\left(\rho\right) = 0. \tag{3.16}$$

The solutions to this equation are given by Bessel functions of the first kind

$$R\left(\rho\right) = J_m\left(\gamma_{mn}\rho\right), \tag{3.17}$$

where $\gamma_{mn}^2 = \omega^2\mu\epsilon - k^2$ is imposed to satisfy boundary conditions. This solution can describe the electric or magnetic field profiles in the $\hat{z}$ direction of TM or TE modes, respectively.

TM modes

TM modes are characterized by a transverse magnetic field and longitudinal electric field, as in Fig. 3.2 and as summarized by the conditions:

$$B_z = 0 \text{ everywhere; boundary condition, } E_z(\rho = s) = 0.$$

The longitudinal electric field profile in an empty cylindrical cavity is described by Eq. 3.15 with $R(\rho)$ given by Eq. 3.17. Then γ_{mn} in Eq. 3.17 becomes $\gamma_{mn} = x_{mn}/R_{\text{cav}}$ where x_{mn} is the nth root of $J_m(x) = 0$. Consequently, the empty-cavity TM resonance frequencies are

$$\omega_{mnp} = \frac{c}{\mu\epsilon}\sqrt{\frac{x_{mn}^2}{R_{\text{cav}}^2} + \frac{p^2\pi^2}{L^2}}, \tag{3.18}$$

where m, $p = 0, 1, 2, ...$ and $n = 1, 2, 3, ...$ Figure 3.3 shows the first few TM mode frequencies for an empty cavity with $R_{\text{cav}} = 2''$ and various lengths. TM_{mn0} mode frequencies are not affected by changing length. TM modes optimize our figure of merit, described in detail in Sec. 3.1. Specifically, we are most interested in the TM_{010} mode since it gives the largest form factor. Other TM modes have components that will cancel to result in smaller form factors. We describe tricks to minimize these negative contributions in Sec. 3.6. The TM_{010} mode in an empty cavity has the lowest frequency of all TM modes and is described by the fields

$$\begin{aligned} E_z &= E_0 J_0\left(\frac{2.405\rho}{R_{\text{cav}}}\right) e^{-i\omega t}, \\ H_\phi &= -i\sqrt{\frac{\epsilon}{\mu}} J_1\left(\frac{2.405\rho}{R_{\text{cav}}}\right) e^{-i\omega t}. \end{aligned} \tag{3.19}$$

In terms of volume, for empty cylindrical cavities, note that the TM_{010} mode resonance frequency is $f \propto 1/R_{\text{cav}}$. More specifically, the TM_{010} mode resonance frequency in an empty cavity is given by

$$f_{010} = \frac{0.115\,\text{GHz}}{R_{\text{cav}}[\text{m}]}. \tag{3.20}$$

Empty cavities are simple geometries that can be solved analytically, but they are not tunable. Since we do not know the correct resonance frequency to match the axion mass, we need to modify the geometry in order to be able to tune the resonance frequency of our mode of interest. Most of our cavity designs include a central conductor rod that is rotated off-center to change the TM_{010}-like resonance frequency, as in Fig. 3.4. Section 3.3 describes how we can approximate the TM_{010}-like mode profile as sinusoidal when the rod is in the center. Rotating around a tuning rod changes the resonance frequencies of all the TM modes.

TE modes

TE modes are characterized by a transverse electric field and longitudinal magnetic field, as in Fig. 3.2 and as summarized by the conditions:

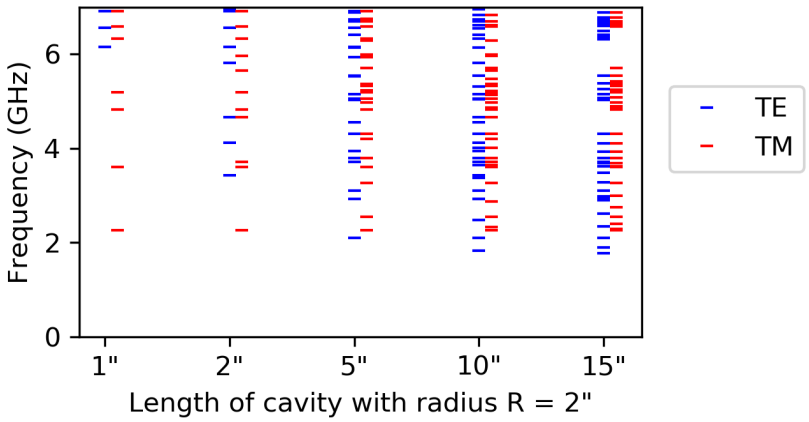

Figure 3.3: Radius $R = 2''$ empty cavity TE (blue, left columns) and TM (red, right columns) resonance frequencies for varying cavity lengths. Calculated using Eq. 3.21 and Eq 3.18. Note that the TM_{010} mode is the lowest-frequency TM mode and does not change in frequency with changing cavity lengths.

$$E_z = 0 \text{ everywhere; boundary condition, } \frac{\partial B_z}{\partial n}(\rho = s) = 0.$$

The longitudinal magnetic field in an empty cylindrical cavity is described by Eq. 3.15 with $R(\rho)$ given by Eq. 3.17. The boundary condition specifies $\frac{\partial B_z}{\partial \rho}(R_{\text{cav}}) = 0$. Then γ_{mn} in Eq. 3.17 becomes $\gamma_{mn} = x'_{mn}/R_{\text{cav}}$ where x'_{mn} is the nth root of $J'_m(x) = 0$. The empty-cavity TE resonance frequencies are given by

$$\omega_{mnp} = \frac{c}{\mu\epsilon}\sqrt{\frac{x'^2_{mn}}{R^2_{\text{cav}}} + \frac{p^2\pi^2}{L^2}}, \tag{3.21}$$

where m, n, $p = 1, 2, 3, \ldots$ so TE_{111} is the lowest-frequency TE mode. Figure 3.3 shows the first few TE mode frequencies for an empty cavity of radius $R_{\text{cav}} = 2''$ and various lengths. Notice that the density of TE modes below 7 GHz increases dramatically with increasing cavity length. Specifically, the density of TE modes around the lowest-frequency TM mode, the TM_{010}, increases with increasing cavity length. Due to the profile of the TE modes, this same behavior occurs in cavities with a central conductor. TM mode frequency increases with decreasing cavity radius, but we cannot make up for the loss of volume by increasing cavity length since the TE mode density increases significantly with increasing length.

When the conducting rod is rotated off-center, the TE mode resonance frequencies do not change significantly compared to the TM mode resonance frequencies. When two modes have approximately the same resonance frequency, they can form a hybrid mixed mode, as discussed in Sec. 3.1 and represented as a cartoon in Fig. 3.1.

TEM modes

Transverse electric and magnetic (TEM) modes only exist in structures with a central conductor. TEM mode characteristics are shown in Fig. 3.2 and are summarized by the following:

$$E_z = 0 \text{ and } B_z = 0 \text{ everywhere.}$$

A drawing of electric and magnetic field vectors for TEM modes are shown in Fig. 3.2. The axial wavenumber of the TEM mode in an infinite medium with permeability μ and permittivity ϵ is:

$$k = \frac{1}{c}\omega\sqrt{\mu\epsilon}. \tag{3.22}$$

TEM mode frequencies can be calculated by considering a standing wave between the two endcaps. Take the cavity with a central conductor to be of length L. Then, the TEM mode resonance frequencies in vacuum can be predicted by the simple relationship:

$$\nu = \frac{c}{\lambda} = \frac{c}{2L/n} = \frac{c}{50.8\,\text{cm}/n} = n\,\frac{3\times10^{10}\,\text{cm/s}}{50.8\,\text{cm}} = 0.591\,n\,\text{GHz}. \tag{3.23}$$

For approximately a relevant size cavity, these TEM modes are predicted to be at 4.13 GHz, 4.72 GHz, 5.31 GHz, 5.91 GHz, 6.50 GHz, and 7.09 GHz. Since the TEM frequencies are primarily determined by the length of the cavity, they do not change significantly when the central conductor moves or changes in size.

3.3 Approximations and simulations

Calculations

We can approximately calculate the TM_{0n0}-like mode frequency and its associated figure of merit of an azimuthally-symmetric cavity by hand. To do these calculations, we must have a closed form of the electric and magnetic field behavior. Cylindrical cavities with large central conductors can be considered as wrapped 2D planar resonators. The electric field between these two planes is

$$E(\rho) = E_0 \sin\left(k_0\left(\rho - R_{\text{rod}}\right)\right), \tag{3.24}$$

$$k_0 = \frac{2\pi n}{2\left(R_{\text{cav}} - R_{\text{rod}}\right)}. \tag{3.25}$$

We can take these as the radially-varying electric field magnitude in the $\hat{z}$ direction of the TM_{0n0}-like mode in a cylindrical cavity of radius R_{cav} with a central conductor of radius R_{rod}. Comparisons between different formulae and EM functions are shown in Table 3.1.

Sinusoidal functions are good approximations for the TM_{0n0} modes in cylindrical cavities with central conductors. Sample calculations for such geometries involving a dielectric shell as well as a central tuning rod are described in Appendix A.

Table 3.1: Comparison of calculations of various factors of interest. Numerical examples are given for the TM_{010} mode in an empty cavity and a TM_{010}-like mode in a cavity with a central conducting rod assuming copper surfaces, $R_{\text{cav}} = 2''$, $R_{\text{rod}} = 1''$, and $L = 10''$. All electric fields are $\vec{E} = E(\rho)\,\hat{z}$.

EM field profiles description	ν (GHz)	Q	C
CST microwave studio simulation, empty cavity	2.26	3.03×10^4	0.693
$E(\rho) = J_0(2.405\,\rho/R_{\text{cav}})$	2.26	3.07×10^4	0.692
$Q_{010} = \frac{2}{1+L/R_{\text{cav}}}\frac{L}{\delta}$ from Ref. [60]	2.26	3.07×10^4	
Experimental test of Cu-coated steel barrel (7-rod cavity)	2.26	2.75×10^4	
CST μwave studio simulation, central conductor	5.83	1.58×10^4	0.814
$E(\rho) = \sin(k_0(\rho - R_{\text{rod}}))$ for $R_{\text{rod}} < \rho < R_{\text{cav}}$	5.91	1.42×10^4	0.811

Simulations

After we predict a resonance frequency with calculations, we can perform finite-element numerical simulations using a rough geometry that includes large features with a significant impact on the resonance frequency and figure of merit, such as the rod in Fig. 3.4a. Next, if the cavity figure of merit, defined in Eq. 3.1, performs acceptably in the tuning frequency range, we can do precise simulations, taking into account more details that can affect the mode crossing sizes (gaps and alumina axles in Fig. 3.4a).

The finite-element numerical simulations discussed throughout this thesis were performed in CST microwave studio (MWS). CST MWS divides the defined geometry into a tetrahedral mesh and solves the Maxwell equations numerically in each mesh cell. For our purposes, we define the inside of the cavity as vacuum and use a background of PEC or copper to approximate the barrel. All metal parts are assumed to be the same as the background, and axles are taken to be loss-free alumina.

After CST MWS finds numerical solutions of resonant mode profiles and frequencies in a given structure, we can integrate the electric and magnetic fields accordingly to calculate the values of interest described in Sec. 3.1. The frequencies of any mode, including the TM_{010}-like mode, can be tracked at various rod rotations. Simulated mode maps show all possible resonant frequencies in a chosen frequency range at each desired rod location. Simulated

modes do not always appear in measurements since not all resonant modes couple to our antennas equally. Also, not all modes interact with the TM_{010}-like mode significantly. Some mode crossing are more severe than others, and if the cavity were machined to mathematical perfection, no mixing would occur. Imperfections that are necessary for an operational cavity, including antennas and gaps between rod and endcaps, increase mode mixing. The intensity of mode crossings is apparent in the mode maps and in the figure of merit components as well.

3.4 One-rod cavity

In HAYSTAC Phases I and II, we used the TM_{010}-like mode of a copper-coated stainless steel one-rod cavity, as shown by the simplified schematic and photograph in Fig. 3.4. The barrel has inner radius $2''$ and height $10''$, and the rod has radius $1''$ and height $9.98''$, making the gaps between the rod and endcaps $0.01''$ on each side. The rod rotates around an axle which is partially composed of $0.25''$ outer-diameter (OD) alumina tubes centered $0.475''$ away from the cavity and rod centers. The axles extend through the endcaps, turrets, bearings, and collars. The bearings provide frictionless rod rotation and the collars fix the gaps on either side of the rod, otherwise the rod would rest on the bottom endcap. We use two dowel pins on either side of the barrel to align the endcaps. This cavity was used in HAYSTAC Phases I and II and was experimentally characterized in detail [61].

During operation in Phase I, we found that the large $2''$ OD rod did not cool efficiently compared to the rest of the cavity. To improve thermal linkage, we used tubes for the axles and inserted a copper rod with $0.125''$ OD into the tubes. The proximity of the copper rod to the $2''$ OD rod could improve thermal linkage, but the risk is that it might become an antenna and increase losses in the cavity. We found that when the copper rod is inserted through the bottom of the cavity, the quality factor does not significantly change. When the copper rod is inserted through the top of the cavity, the quality factor decreases as it enters the cavity, but then improves again, reaching approximately its original value. This was defined as the optimal insertion depth of the copper rod since it maximized proximity to the rod while minimizing the losses it introduced.

Tuning range

Simulations of the Phase I and II one-rod HAYSTAC cavity help us gain insight into cavity behavior throughout the tuning range of the TM_{010}-like mode of interest. The simulated mode map in Fig. 3.6 shows resonance frequencies of all possible modes and mode crossings. As the rod is rotated away from the center of the cavity in steps of half a degree, the resonance mode frequencies change in different ways. Throughout the full rotation, the TM_{010}-like mode tunes in the range $3.4 - 5.8\,\mathrm{GHz}$, mixing with a few modes in the frequency ranges highlighted by red boxes in Fig. 3.6. In this cavity, TE mode crossings were found to be much wider than TEM mode crossings [61]. To mitigate the effects of mode crossings

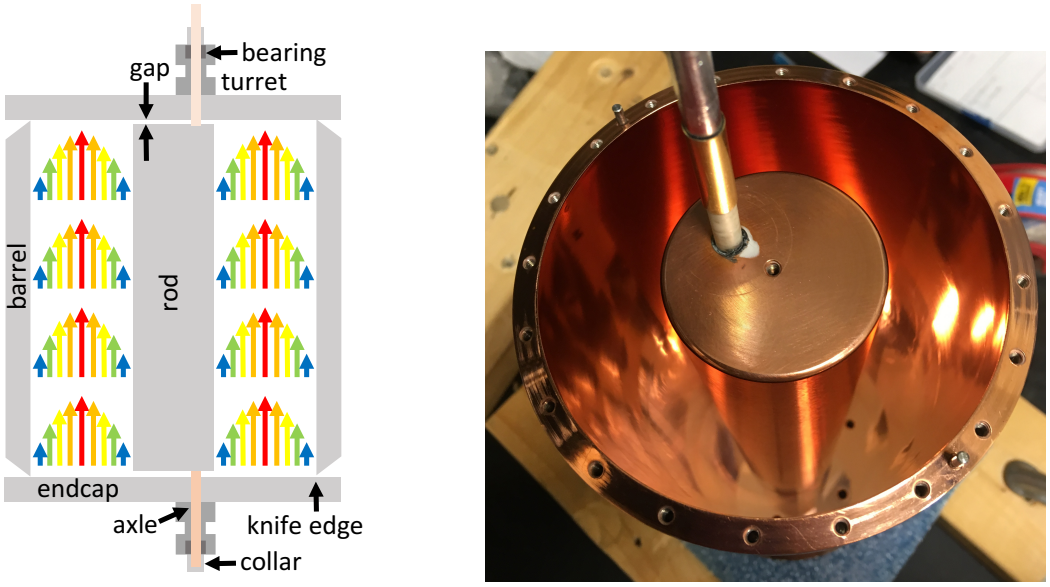

(a) Cavity sketch.

(b) Phase I and II HAYSTAC cavity.

Figure 3.4: one-rod cavity (a) cartoon image with spatially-dependent electric field strength of the TM_{010}-like mode (electric field intensity ranges between maxima denoted by long red arrows and minima denoted by short blue arrows) and (b) top-view photographic image with top endcap removed.

on our tuning range, we partially insert a vernier, which is a dielectric rod that changes the resonance mode frequencies differently than the movement of the metal tuning rod. This vernier provides a way to finely tune the mode frequencies.

As mentioned in Sec. 3.3, the CST MWS simulations involve a copper rod with 0.010″ gaps on either side with 0.25″ OD alumina axles at the pivot point surrounded by vacuum and then a copper background marking the inner surface of the cavity. A part of the same mode map appears with axes flipped in Fig. 3.7. Note that every predicted mode crossing in the mode map corresponds to a decrease in TM_{010}-like mode form factor. Some mode crossings are too narrow to cause significant disruption in the tuning range, since we do not see them appear in the experimentally observed mode crossing red regions. Since Phase I of HAYSTAC involved the frequency range $5.6-5.8\,\mathrm{GHz}$, we went through detailed simulations of form factor for those regions. Simulated form factors enter into our calculated sensitivity, so it is crucial to carefully map the frequency-dependent quantity.

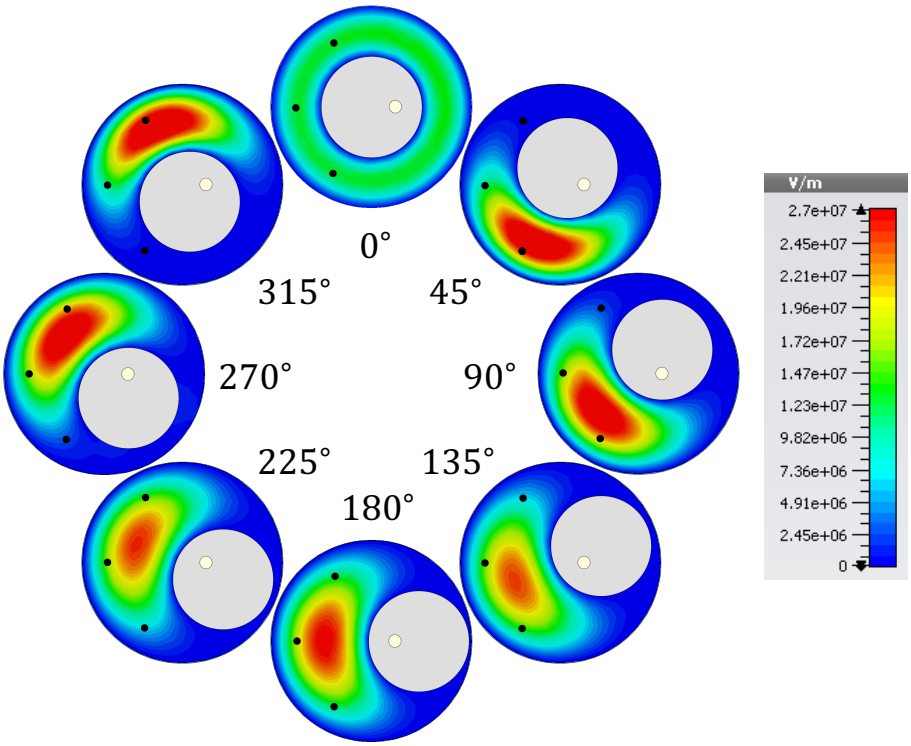

Figure 3.5: Top-view simulated electric field intensity plots of the TM_{010}-like mode at various rod rotations in the one 2″ OD rod design. Red corresponds to areas of high electric field and blue corresponds to areas of low electric field, as in Fig. 3.4a. Three holes available for antennas are marked by black dots.

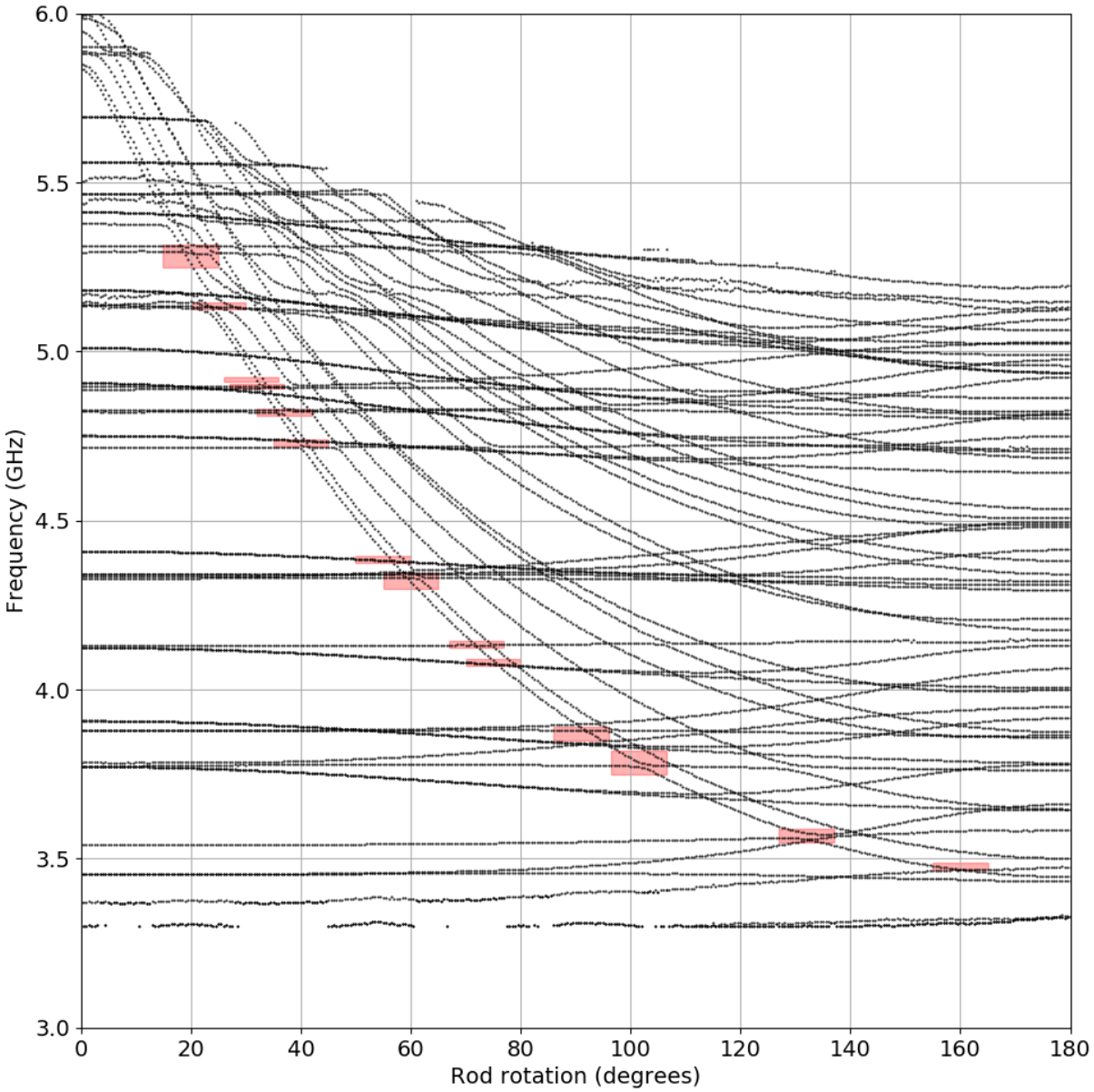

Figure 3.6: Simulated mode map shows a black dot at each possible mode frequency at discrete rod locations in a cavity matching the one used in HAYSTAC Phases I and II, described at the start of Sec. 3.4. TM mode frequencies change significantly with rod rotation compared to those of TE and TEM modes. TM_{010}-like mode frequencies correspond to the lowest-frequency TM mode at all rod rotations. Red boxes correspond to experimentally-observed mode crossings of the TM_{010}-like mode. The box heights reflect mode crossing ranges observed during cavity characterization, while box lengths and horizontal positions are arbitrary.

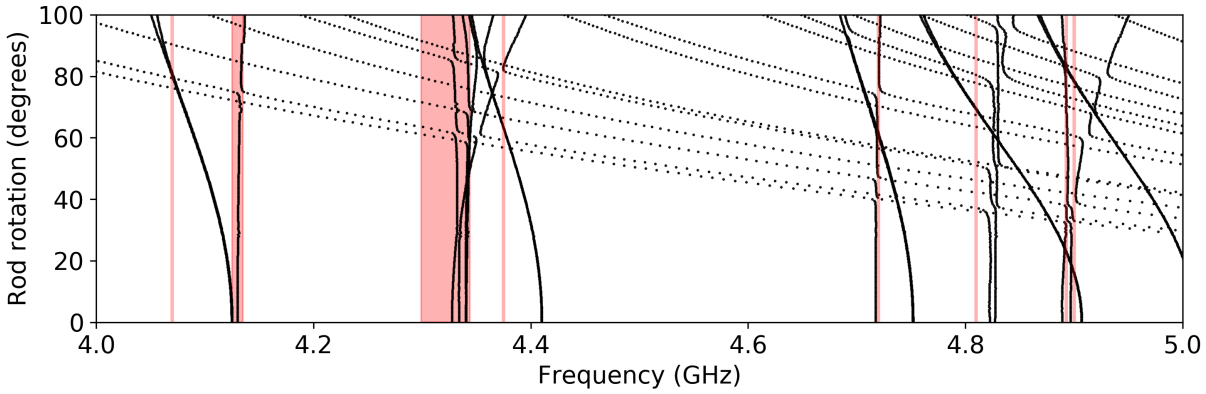

(a) Mode map with flipped axes. TM_{010}-like mode frequencies correspond to points on lowest sloping line.

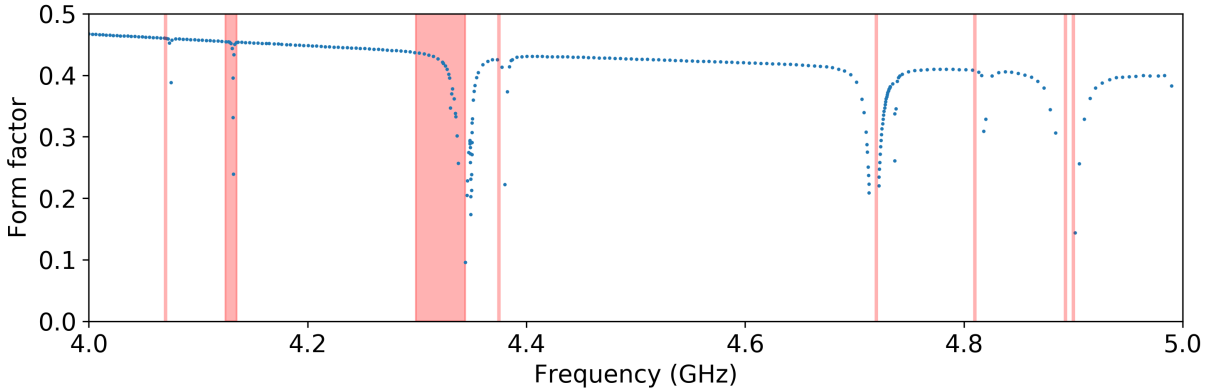

(b) One-rod form factor calculations.

Figure 3.7: HAYSTAC Phase I and II cavity (a) mode map and (b) form factor. Red areas denote experimentally-observed mode crossing regions, same as in Fig. 3.6.

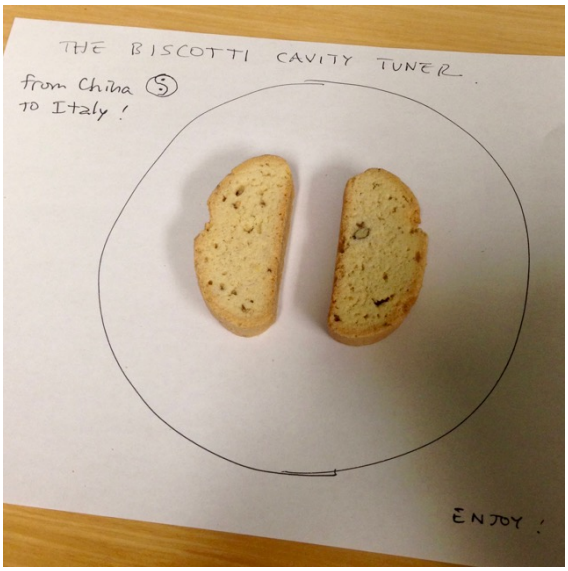

Figure 3.8: An introduction to the biscotti cavity design idea by Prof. Karl van Bibber.

3.5 Multi-rod cavities

The TM_{010}-like mode behavior in the one-rod cavity suggests that the form factor is optimized in azimuthally-symmetric geometries; when the rod is in the center of the cavity. Since the quality factor behavior is difficult to predict, we can motivate our designs by improving the form factor and volume. Based on this concept, we would optimally have a rod in the center which changes in radius without breaking symmetry. Our multi-rod cavity ideas are trying to approximate this ideal.

One concept involves dividing the rod in two pieces and tuning the TM_{010}-like mode resonance frequency by moving the two rods apart. The two designs we considered are the "yin-yang" and "biscotti" cavities. The biscotti cavity concept is shown in Fig. 3.8. We simulated both designs with 10 mil gaps and without axles to find the cavity figure of merit across the tuning ranges. Simulation results are summarized in Fig. 3.9. We originally expected the TM_{010}-like mode frequency to increase as the rods moved apart and as the space between the rod and cavity wall shrunk. However, as the bottom row of electric field heat maps in Fig. 3.9e shows, the TM_{010}-like mode resonance frequency decreases as the electric field begins to occupy the space between the rods instead. The top row of Fig. 3.9e also shows that although the electric fields behave as expected for a limited rotation of the rods, increasing rotating angles allows the electric field to occupy the space between the rods and the frequency of the TM_{010}-like mode to decrease (in the left-most image). Although the performance of these two cavities is approximately the same as that of the familiar one-rod cavity, these two-rod designs do not provide a promising concept for accessing higher frequencies.

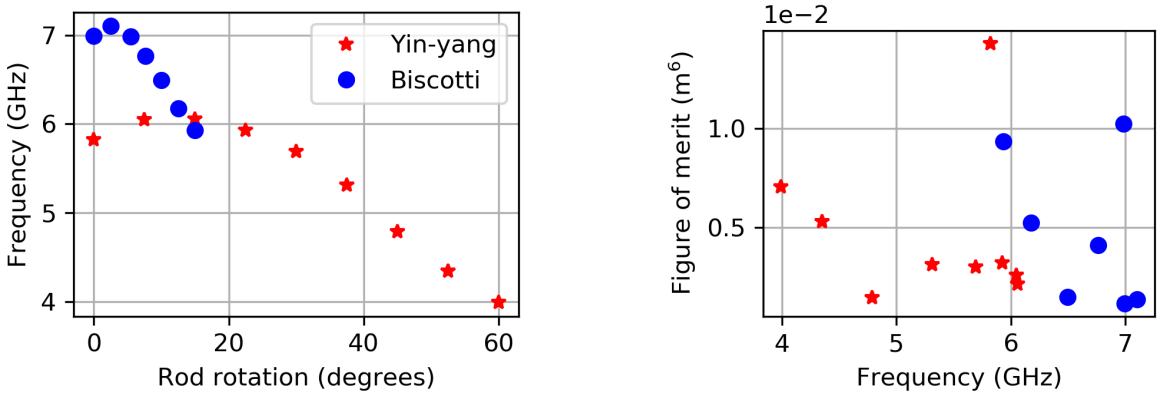

(a)

(b)

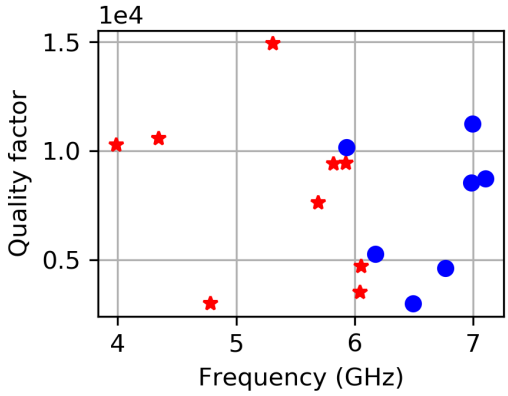

(c)

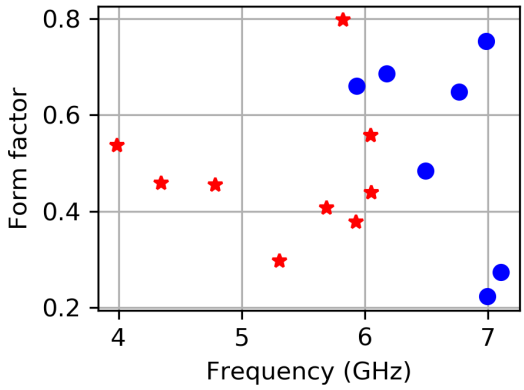

(d)

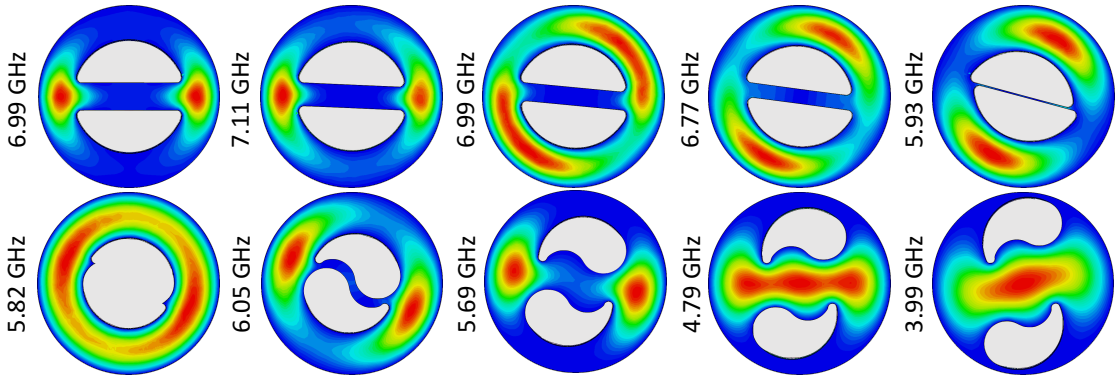

(e)

Figure 3.9: Two-rod simulation results; (a) TM_{010}-like mode resonance frequency for varying rod rotations, (b) cavity figure of merit QC^2V^2, (c) quality factor Q, and (d) form factor C as functions of resonance frequency. Also, the (e) electric field intensity plots.

Table 3.2: Frequency and form factor for empty-cavity higher-order modes. Values were calculated assuming a copper cavity matching the barrel used in Runs I and II of HAYSTAC.

Mode	Frequency	Form Factor
TM_{010}	2.26 GHz	0.69
TM_{020}	5.19 GHz	0.14
TM_{030}	8.13 GHz	0.05

3.6 Higher-order modes with a cavity incorporating a dielectric shell

One strategy for higher-frequency searches is using higher-order modes of an existing cavity geometry. Higher-order modes in the same cavity have higher frequencies, as in the few examples in Table 3.2. Although TM_{mnp} modes always have a longitudinal electric field orientation in the direction of the external magnetic field, modes of higher order than TM_{010} have negatively-contributing components to the form factor, as shown by the electric field profile of the TM_{030}-like mode in Fig. 3.10a and as also noted by the decreasing form factor with increasing n in Table 3.2. In fact, in a cylindrical geometry, the TM_{0n0} mode form factor scales inversely with the square of the frequency: $C_{0n0} \sim \nu_n^{-2}$ [62, 63, 64]. These negative contributions can be suppressed by adding dielectric elements into the cavity. For example, as the electric field profile of the TM_{030}-like mode in Fig. 3.10b shows, an optimized dielectric shell can improve the form factor of a TM_{030}-like mode from 0.09 to 0.6 while only slightly decreasing the resonance frequency. Such distributed Bragg reflector microwave resonators have achieved room-temperature quality factors of 10^5 at resonance frequencies around 10 GHz [65].

For any cylindrical central conductor, there is a dielectric shell that optimizes the form factor, predicted by the calculations in Appendix A. We must be able to tune the resonance frequency, and ideally, re-optimize the dielectric shell for every rod configuration. Since each dielectric shell can improve the TM_{030}-like mode form factor for several rod sizes, we decided to use a single shell and to tune the resonance frequency by changing the rod configuration. We considered one-rod and seven-rod geometries. Figure 3.11 shows simulation results of the TM_{030}-like mode at various tuning positions of one-rod and seven-rod geometries with a dielectric shell of 1.15″ inner radius and 0.2″ thickness. These eigenmode simulations do not include gaps or axles in the one-rod case and include only 0.01″ gaps in the seven-rod case. The approximately constant form factor in Fig. 3.11c suggests that preservation of symmetry in the seven-rod design allows the dielectric shell to continue to provide improvement throughout the tuning range better than the off-center single tuning rod. This symmetry

of the seven-rod design and lack of symmetry in the one-rod design can also be seen in the electric field heat maps in Fig. 3.11d. In the images, the weaker second ring of the electric field corresponds to the negative contribution to the form factor. We minimize this second ring by optimizing the dielectric shell dimensions. Based on the promising simulation results of the TM_{030}-like mode in the seven-rod design, we built a prototype and experimentally characterized the performance of this geometry.

Design and testing of prototype

One of the constraints for the prototype was a barrel that matched the barrel used in Phases I and II of HAYSTAC of 10″ length and 2″ radius. From the simulations presented in Fig. 3.11, a shell of inner radius 1.15″ and thickness 0.2″ promised at least a form factor of $C_{030} \sim 0.5$ across the frequency range $8.3\,\text{GHz} < \nu_a < 10.3\,\text{GHz}$ accessible using two sets of rods. For the first prototype, we chose to make seven aluminum 0.375″ OD rods. The closest readily-available size of alumina shell[1] was approximately 1.1875″ inner radius and 0.1875″ thickness. The length of the shell is 10.188″, which was longer than the cavity barrel, so grooves were machined in the endcaps to fit this shell. Since the shell was warped on the edges, special care was taken to machine the ends of the shell and match them to the grooves on the endcaps. Figure 3.12 shows photos of various assembly stages. Six aluminum rods are designed to rotated away from their inner-most position together since they're connected by gears to a central rotating shaft. The gears are on two levels, as in Fig. 3.12c. The rod axles are composed of an alumina piece that connects to an aluminum shaft which is aligned by a bearing.

This seven rod design was successful mechanically; the six rods rotated together with only a slight stiction, which can be mitigated by improving alignment and using finer gears. Electromagnetically, we found that the presence of the dielectric shell significantly complicated the resonance mode structure of the cavity. We were not successful in identifying the TM_{030}-like mode in this geometry. Instead of investigating the complicated structure at high frequencies in the tuning range of the TM_{030}-like mode at $9.35 - 10.05\,\text{GHz}$, we simplified the geometry by taking out the six tuning rods and studying the effect of inserting the dielectric shell. We found that the shell introduces many extra modes even around the TM_{010}-like mode at around 3 GHz. We also studied the behavior of the familiar TM_{010}-like mode with seven rods in the range $4 - 4.5\,\text{GHz}$. We found that the TM_{010}-like mode performed well throughout its tuning range. This inspired building a seven-rod cavity with larger rods and without a dielectric shell for the purpose of studying the TM_{010}-like mode.

Although the dielectric shell with seven rods design had a mode density that was too high to operate, this method of using higher-order modes is promising if we could reduce the number of intruder modes. One idea for to decrease mode density uses a photonic band gap (PBG) structure that is designed to confine only certain types of modes [66, 67]. For example, the structure could confine TM modes while the TE modes in a certain frequency

[1] CoorsTek, Inc. 600 9th Street, Golden, CO 80401 USA

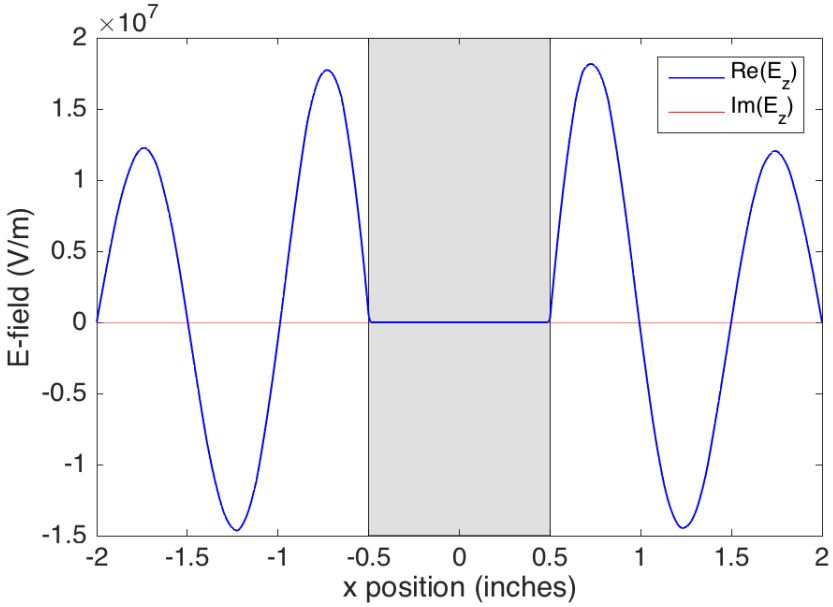

(a) Without shell: $f_{030} \sim 11.7\,\text{GHz}$, $C_{030} \sim 0.09$.

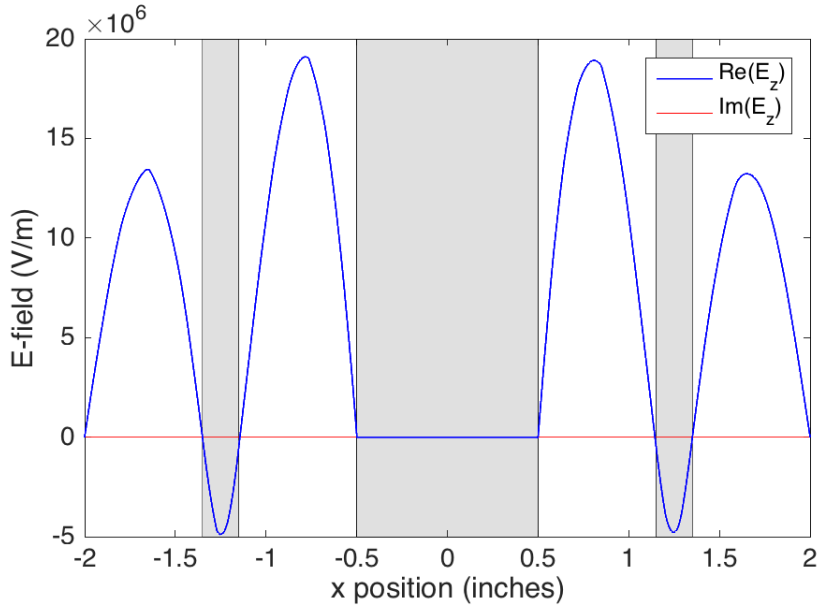

(b) With shell: $f_{030} \sim 9.08\,\text{GHz}$, $C_{030} \sim 0.6$.

Figure 3.10: Simulated longitudinal electric fields of the TM_{030}-like mode in cavity with centered $1''$ diameter rod. Addition of a dielectric shell ($1.15''$ inner radius and $0.2''$ thick) improves the form factor. For more details on this geometry, see Fig. A.2.

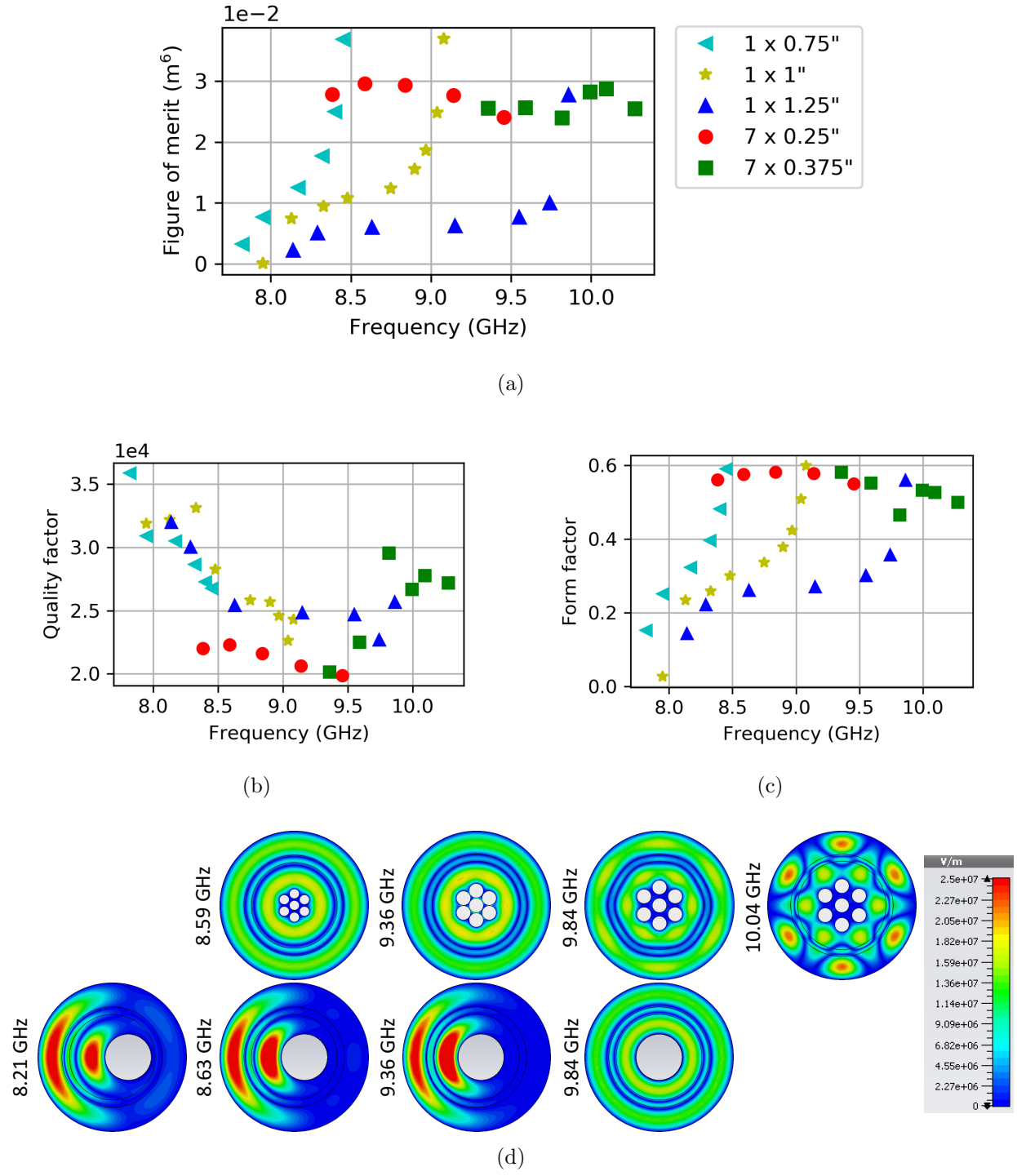

Figure 3.11: Comparison of TM_{030}-like mode behavior in seven-rod and one-rod designs with a 0.2″-thick dielectric shell of 1.15″ inner radius. Plots of (a) figure of merit QC^2V^2, (b) quality factor Q, (c) form factor C, and (d) a selection of electric field intensity plots.

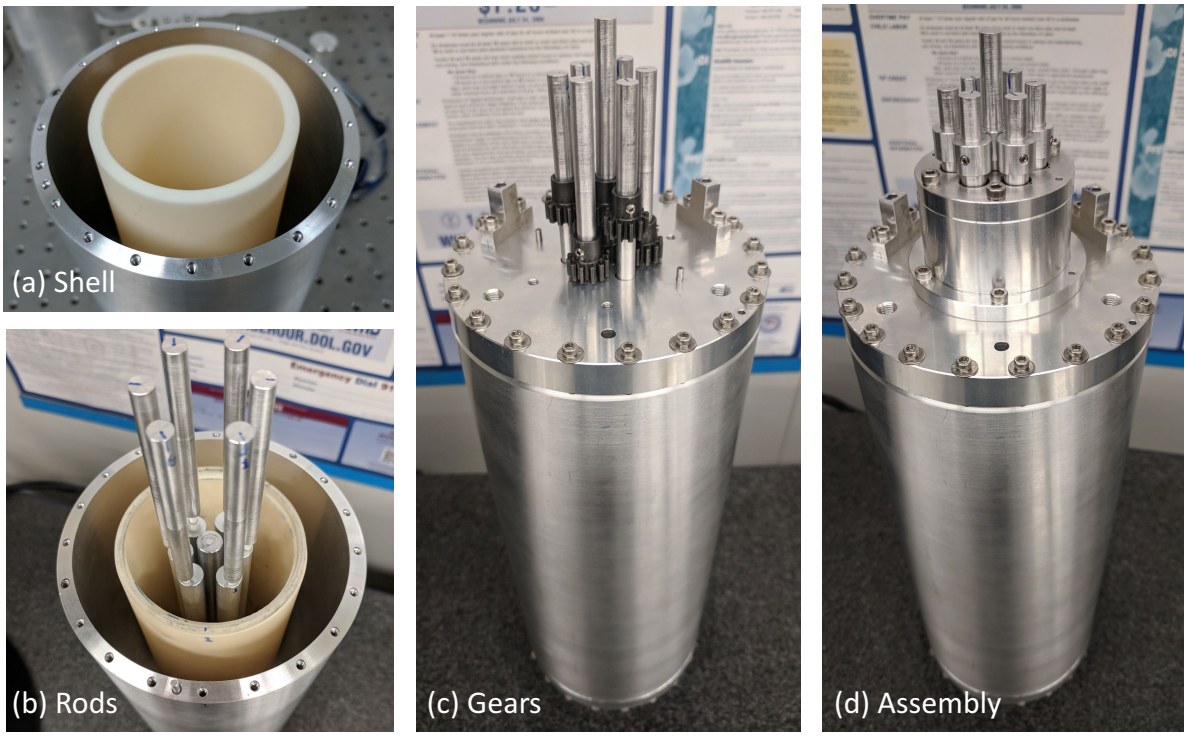

Figure 3.12: Seven rod with shell design photos. This prototype cavity is machined from aluminum with (a) an alumina shell, (b) six aluminum rods that rotate symmetrically and are connected by (c) gears to each other to create (d) the complete assembly.

range would radiate out. Such a structure has an array of rods instead of a cylindrical barrel. If we were to encase the seven-rod with shell design in a PBG structure, we could take advantage of the reasonable figure of merit of these higher-frequency designs.

Chapter 4

Seven-rod cavity

The axion mass is unknown, so we must be able to search through various mass ranges. Recent theoretical work motivates higher-mass axions [68]. We found that the best cavity design for the frequency range of approximately 5.5 to 7.5 GHz is a symmetrically-tuning seven-rod design. This design focuses on preserving symmetry, which is beneficial for keeping a higher form factor throughout the tuning range and allows us to probe higher frequencies without sacrificing volume. In this chapter, I describe the design and construction of a seven-rod cavity (Sec. 4.1), then discuss the testing and characterization (Sec. 4.2).

4.1 Design and construction

As in Ch. 3, the cavity barrel size is constrained in width by the size of the magnet bore and in length by the density of TE and TEM modes we choose to allow in our frequency range of interest. To probe higher frequencies with a TM_{010}-like mode, we must increase the rod size. Increasing the rod size exaggerates the electric field asymmetry when the rod is off-center and decreases the cavity volume.

In a seven-rod design, the six peripheral rods move symmetrically away from the central rod. The central rod keeps the electric field of the TM_{010}-like mode from entering the space between the rods. Figure 4.1 shows heat maps of the TM_{010}-like mode electric field magnitudes for several rod rotations in the seven-rod design. For comparison, the one-rod design heat maps are in Fig. 3.5. The presented simulated heat maps are cross sections taken at the center of the $4''$ diameter cavity use seven $0.625''$ OD rods. The 0° rotation in the seven-rod design (seven rods are closest to each other) corresponds to the minimum frequency of the TM_{010}-like mode, while the 0° rotation in the one-rod design (rod is in the center of the cavity) corresponds to the maximum frequency of the TM_{010}-like mode in that design. These rod rotations give the most rotationally-symmetric electric field shape. Throughout the whole tuning range, the seven-rod design preserves symmetry better than the one-rod design.

Figure 4.2 and Table 4.1 compare the simulated performance of one-rod cavities to that

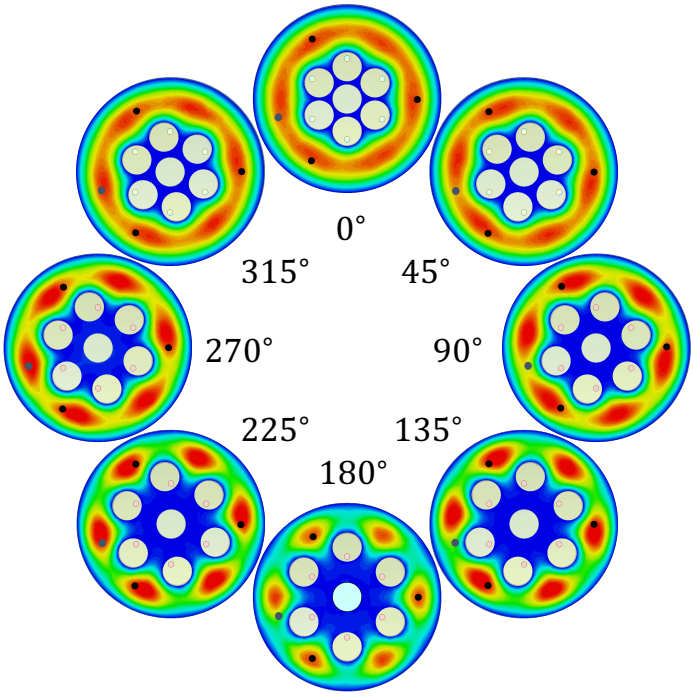

Figure 4.1: Top-view heat maps of TM_{010}-like mode electric field strength at various rod rotations in the seven 0.625″ OD rod design. Three holes available for antennas are marked by black dots.

of seven-rod cavities, both incorporating 0.01″ gaps between the rods and endcaps as well as appropriately-sized alumina axles. In case of later comparisons with measured data, the final gap sizes of in the seven-rod cavity are much smaller than 0.01″, which in some cases correspond to better performance than the simulations with larger gaps. To compare cavity designs, we focus on the figure of merit QC^2V^2 described in Sec. 3.1, its components, and the accessible frequency range of the TM_{010}-like mode in the designs. As presented in Table 4.1, the TM_{010}-like mode in a seven-rod design reaches a higher frequency in a larger volume compared to the one-rod design. This behavior of larger volumes with the seven-rod design could potentially be extended higher in frequency.

The plots in Fig. 4.2 show the figure of merit QC^2V^2 variation across the TM_{010}-like mode frequency range in one 2″ OD rod, one 2.46″ OD rod, seven 0.625″ OD rods, and seven 0.875″ OD rods cavity designs. The form factor is maximized in the 0° rotation for all designs, which correspond to the top of the frequency range in the one-rod designs and to the bottom of the frequency range in the seven-rod designs, respectively. As suggested by the symmetry in the seven-rod design throughout the tuning range, the form factor only slightly decreases as the TM_{010}-like mode is confined to smaller volumes at higher frequencies. In

Table 4.1: Comparison of cavity volume and maximum frequency of the TM_{010}-like mode for one-rod and seven-rod designs.

Design	Volume	Maximum frequency
$1 \times 2''$ OD	1.55×10^{-3} m^3	5.8 GHz
$7 \times 0.625''$ OD	1.71×10^{-3} m^3	7.4 GHz
$1 \times 2.46''$ OD	1.37×10^{-3} m^3	7.8 GHz
$7 \times 0.875''$ OD	1.28×10^{-3} m^3	9.9 GHz

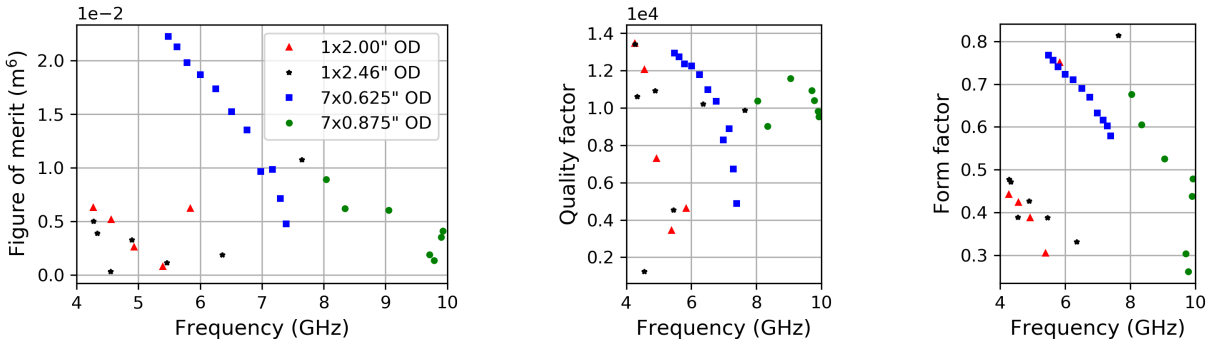

(a) (b) (c)

Figure 4.2: Comparison of TM_{010}-like mode behavior in seven-rod and one-rod cavity designs. Plots of (a) figure of merit QC^2V^2, (b) quality factor Q, and (c) form factor C. Simulations take into account $0.01''$ gaps on either side of the rods and appropriately-sized alumina axles.

contrast, the form factor for most of the tuning range in a one-rod design is significantly lower than its maximum. Overall, other than the instances when the single rod is in the middle of the cavity, the seven-rod designs give a higher figure of merit than the one-rod designs up to at least around 9 GHz. Higher frequencies are difficult to obtain since in the seven rod case, the electric field begins to occupy the space between the central rod and six moving rods. To avoid this and to keep increasing TM_{010}-like mode frequencies, we must turn to larger rods, which limit our tuning range.

Design decisions

Seven-rod cavity design decisions were motivated by a combination of electromagnetic simulations and preliminary testing. A few of the design decisions are outlined in the bullet points below:

- **Pivot points:** Although theoretically a seven 0.625″ OD rod design in our current barrel can access 5.3−7.8 GHz, practical construction requires some room for machining imprecision and space for axles. We chose a pivot point 0.875″ from the cavity center, which is 0.188″ from a rod center. This pivot point allows for an alumina axle of 0.125″ OD, a 0.062″ space between rods at their innermost positions, and gears of a standard pitch diameter.

- **Gears:** We chose a standard pitch diameter of 0.875″. The satellite gears connect to the center anti-backlash gears on the driveshaft.

- **Bearings, antenna ports, and collars:** We chose to keep the bearings, antenna ports, and collars to stay the same as in the current HAYSTAC cavity.

- **Antenna placement:** We placed three antenna holes rotated 120° from each other at a radius of 3″, as marked by black dots in Fig. 4.1b.

- **Teflon washers:** Originally, the idea was to put teflon washers in the gaps to prevent the rod from scraping the endcap, but we have found that the presence of a teflon washer significantly increases mode localization in the gaps. We also found that these smaller rods can be easily aligned to not scrape during rotation.

- **Step on top endcap:** The 0.0125″ gaps on each end were deemed unduly large, and given the well-established performance benefits of smaller gaps, we decided to reduce the gaps by machining down the thickness of one endcap by 0.015″ at a radius of 1.9″ from the endcap center, leaving a positive step inside that radius. This has the effect of bringing the two endcap surfaces closer together by 0.015″, or equivalently reducing each gap by 0.0075″, to 0.005″. This machined step can be seen in the right endcap of Fig 4.3a.

- **Materials:** We used steel for the barrel and endcaps and alumina for the axles, as in the current HAYSTAC cavity. The rods are made out of aluminum for improved thermal properties over steel and for ease of machining. The outer rod axles are made of steel.

- **Thermal contact:** In case we need to implement a similar thermal link as the HAYSTAC cavity, we made sure to use tubes as axles and leave room for a 0.0625″ OD copper rod.

Plating and baking

To improve electromagnetic performance and to decrease the gaps between the rods and endcaps, we copper-plated the seven-rod cavity with a thickness of several skin depths. The skin-depth of copper at 5 GHz, given by Eq. 3.7 and using parameters specified in Table A.1,

is approximately $\delta_{\mathrm{Cu}} \approx 1\,\mu$m. Therefore, a copper layer of thickness $0.006''$ (around $150\,\mu$m) is sufficient.

After plating, annealing the copper should improve its electromagnetic performance by lowering its resistivity. For this purpose, the rods and barrel were heated to 270°C and the endcaps were heated to 350°C in an H_2 environment. Although the cavity was not tested at each stage of manufacturing, the quality factor of the empty cavity after plating and annealing was approximately 2.74×10^4 at weak coupling, compared to the theoretically-predicted 3.07×10^4.

Cavity assembly

A procedure describing the assembly of the seven-rod cavity is outlined in Appendix B using components listed in Table B.1. We use a torque wrench for attaching the endcaps to the barrel and tighten the screws in a star pattern to avoid damaging the fine threads and to ensure a good seal with the barrel knife edge. Another key aspect of assembling the cavity is to take steps for aligning the rod correctly. This requires using an alignment tool to keep rods approximately in the correct rotation and fixing the rod axles in the bearings before engaging the gears. Several photos of the copper-plated, annealed, and re-machined parts and assembly are shown in Fig. 4.3. Fig. 4.3a shows the top (left) and bottom (right) endcaps, Fig. 4.3b shows the assembled rods with alumina and stainless steel axle components glued together, Fig. 4.3c shows one of the antenna ports attached to the top endcap, Fig. 4.3d show the removal of the alignment tool after the gears have been fixed, Fig. 4.3e shows the gears in approximately their correct locations, Fig. 4.3f is a side view of the fully-assembled cavity, Fig. 4.3g shows the uncovered rod axles sticking out of the bottom of the cavity, Fig. 4.3h is the same view as the previous one with the bottom endcap and collars in place, Fig. 4.3i is an angled view of the assembled cavity with the top-hat and collars in place, and Fig. 4.3j show the bead-line and bead strung through one of the holes available as an antenna port in other configurations. The final coated and re-machined parts leave approximately $0.007 \pm 0.001''$ total for the two gaps between the rods and endcaps, which was measured using leaf gauges. Overall, the rotation is smooth throughout the tuning range except a slight resistance in parts most likely due to the tight fit and slight deformation of the bearings.

4.2 Testing and characterization

We have several tools available to us for cavity characterization. Our vector network analyzer (Keysight E5071C, ENA Series Network Analyzer, 300 kHz - 20 GHz) can measure reflection and transmission of microwave signals in the frequency range of interest. When the coaxial antennas couple to a resonant mode, more signal is transmitted. By measuring the scattering parameters between two ports S_{11} (reflection), S_{12} (transmission), S_{21} (transmission), and S_{22} (reflection), we can observe the frequencies and quality factors of resonant modes in our cavity. Traditionally, we choose to focus on the S_{21} scattering parameter, which

Figure 4.3: Seven-rod cavity photos after copper-plating and re-machining.

measures the transmission from port 1 to port 2. All measurements are done with weak coupling to our coaxial antennas to minimize perturbations due to the antenna presence in the cavity. Unfortunately, in our existing set-up, we can calibrate effects of cables, but not the effects of reflections from within the antennas.

Scattering parameter measurements give us information on the frequencies and quality factors of resonant modes, but not on their profiles. To get insight on the resonant mode shape, we pull a relatively (compared to the cavity size) small bead through the length of the cavity, measuring the resonance frequency at each step. An example setup and bead pull measurement are shown in Fig. 4.4. The presence of the bead inside the cavity perturbs the electromagnetic field and shifts the resonance frequency by a magnitude proportional to the square of the strength of the electric field at the bead location [54, 69]. If the bead is only slightly perturbing the electric field, the frequency shift we expect is given by

$$\frac{\Delta\omega}{\omega} = \frac{-(\epsilon-1)}{2}\frac{V_{\text{bead}}}{V_{\text{cav}}}\frac{E(r)^2}{\langle E(r)^2\rangle_{\text{cav}}}, \tag{4.1}$$

where V_{bead} and V_{cav} are the volumes of the bead and cavity, respectively [70]. This bead perturbation technique is commonly used in the microwave engineering community, although it has only recently entered the axion haloscope world. Bead perturbation measurement results at several rod locations of the seven-rod cavity are shown in Fig. 4.5 for rods rotating in one direction. The top left corner and bottom right corner show the bead perturbation measurements of the TM_{010}-like mode at its minimum and maximum frequency in this cavity, respectively. Throughout the tuning range, the TM_{010}-like mode electric field is consistently stronger on one end of the cavity compared to the other.

Tuning range

The TM_{010}-like resonant mode frequency is tunable over $5.529-7.440$ GHz in the copper-plated cavity. The simulated and measured mode maps in Fig. 4.6 show several resonant mode frequencies as a function of rod rotation away from the inner most position. The measured mode map gives a slightly higher frequency tuning range for the TM_{010}-like mode than the simulated case since the copper coating was thicker than designed. Heat maps of the electric field at several of these rotation locations are shown in Fig. 4.1. The measured mode map is generated by recording the S_{21} scattering parameter at each half-degree rotation step of the rods and plotting the signal magnitude as a heat map. Lighter areas correspond to higher magnitude of signals and therefore resonant mode frequencies. These measurements are only sensitive to resonant modes that couple to our antennas, so we are not able to see the TE or TEM modes until they couple to the TM modes and cause mode crossings. In Fig. 4.6, the lowest-frequency line increasing in frequency with increasing rod angle corresponds to the TM_{010}-like mode.

Throughout the tuning range, the TM_{010}-like mode passes several intruder modes, as is apparent in the mode maps. As mentioned in Sec. 3.2, TEM resonant mode frequencies in

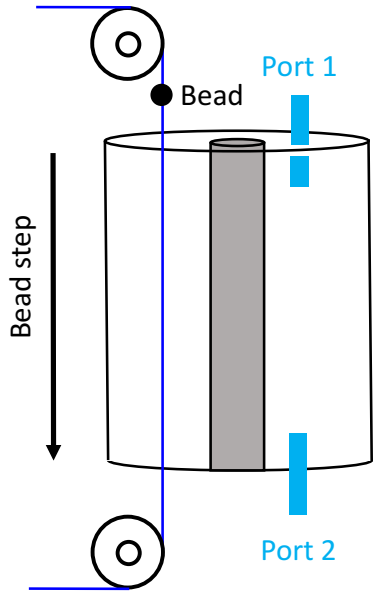

Figure 4.4: Bead perturbation technique setup.

our cylindrical cavities with central conductors are determined only by the cavity height and therefore do not change with rod rotation. These TEM modes in the current seven-rod cavity, based on designed dimensions, are at 5.91 GHz, 6.50 GHz, and 7.09 GHz, which correspond to the frequencies of the widest mode crossings in the seven-rod cavity. The other frequencies correspond to TE modes. Those that decrease in frequency with increasing rod angle, such as the mode in Fig. 4.9, do not appear in the single-rod cavity mode map since they are mostly confined to the space between the central rod and the outer rods. There are also TM modes that increase slowly with increasing rod rotation compared to the other TM modes. These are the TM_{31l} modes based on simulations and bead perturbation measurements.

Figure 4.7 shows a few select mode crossings in detail. The lowest-frequency line increasing in frequency with increasing rod angle corresponds to the TM_{010}-like mode, as before. Figures 4.7a, 4.7c, and 4.7f show crossings of the TM_{010}-like mode with TEM modes. These mode crossings occur over frequency ranges of approximately 60 MHz, 20 MHz, and 40 MHz at 5.90 GHz, 6.49 GHz, and 7.07 GHz, respectively. Figures 4.7d, 4.7d, and 4.7e show narrower mode crossings of approximately 5 MHz, 10 MHz, and 5 MHz, respectively. These correspond to mode crossing of the TM_{010}-like mode with TE modes. There are a few other narrow mode crossings throughout the tuning range. Conservatively, we can approximate that mode crossings affect approximately 170 MHz of the 1.9 GHz tuning range of the TM_{010}-like mode, which means that more than 90% of the tuning range $5.529 - 7.440$ GHz is clear of mode crossings.

Figure 3.1 shows a cartoon of what happens to our TM_{010}-like mode of interest when it

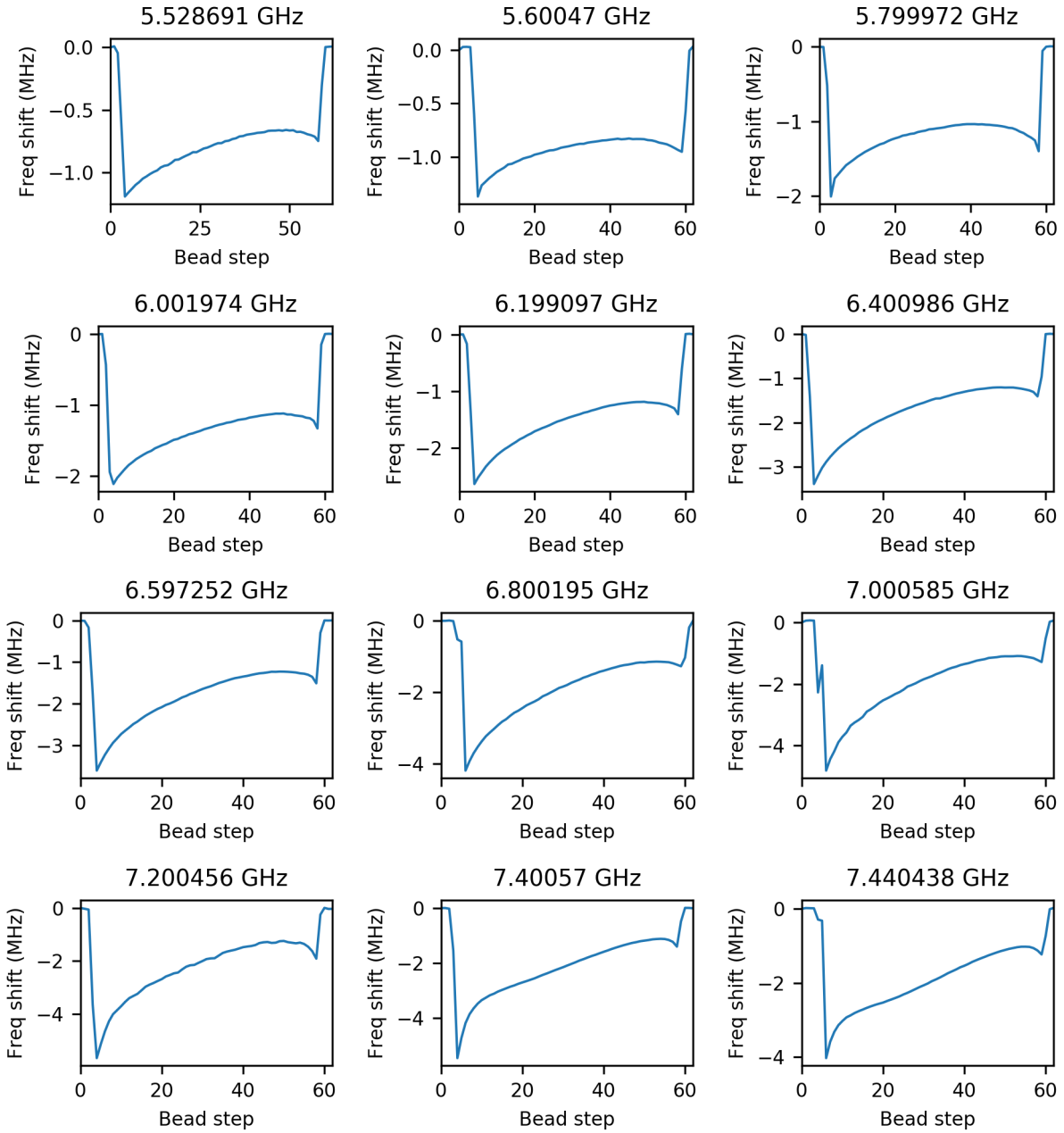

Figure 4.5: Measured frequency shift of the TM_{010}-like mode from bead perturbations at steps along the length of the seven-rod cavity. The plot title specifies the unperturbed TM_{010}-like mode resonance frequency corresponding to a frequency shift of zero. The dielectric bead decreases the resonance frequency when it enters the cavity.

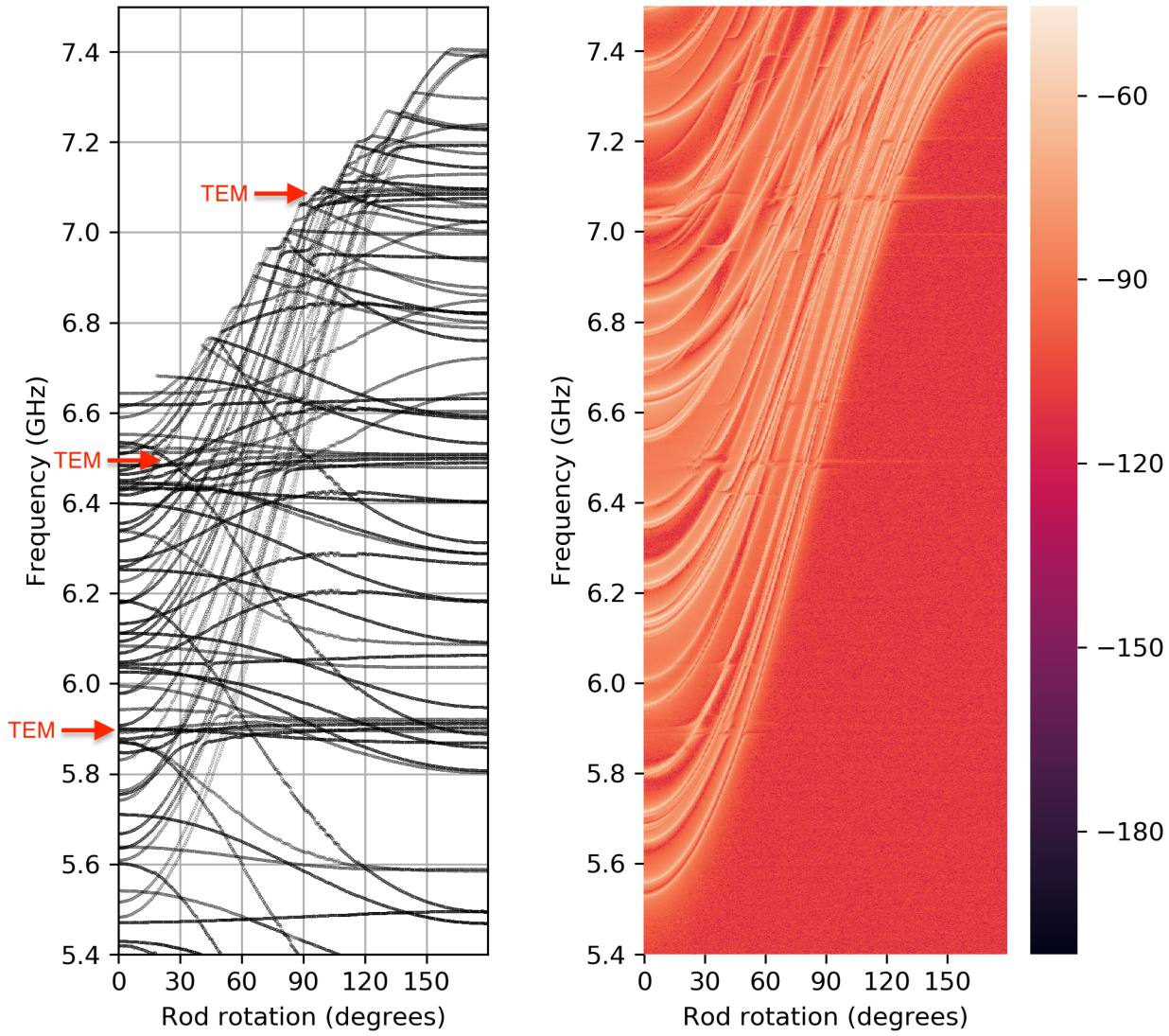

(a) Simulated mode map.

(b) Measured mode map.

Figure 4.6: Seven 0.625″ OD rod design mode map based on (a) eigenmode simulations and (b) measured S_{21} scattering parameters. TM modes are the most prominent types of modes in the measured mode map since TE and TEM modes do not couple to our antennas as well as the TM modes. Detailed maps of a few mode crossings are presented in Fig. 4.7.

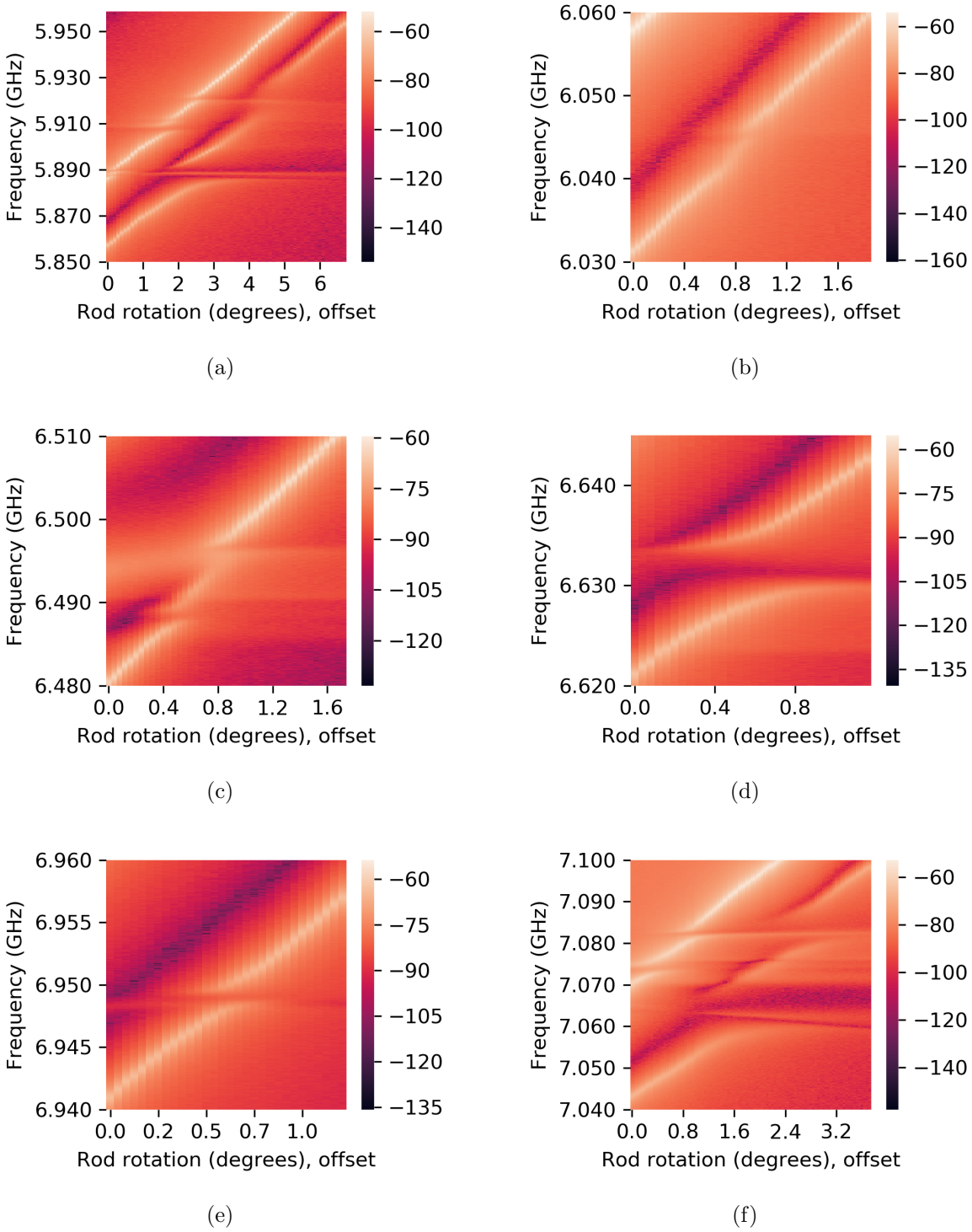

Figure 4.7: Detailed mode maps of mode crossings at (a) 5.90 GHz, (b) 6.04 GHz, (c) 6.49 GHz, (d) 6.63 GHz, (e) 6.95 GHz, and (f) 7.07 GHz. The rod rotations are presented in degrees with an arbitrary rotation offset. As before, the associated scale gives the magnitude of the S_{21} scattering parameters in units of dB. Some mode crossings are wider than others.

approaches an intruder mode. Using the bead pull technique, we can probe this interaction. Figure 4.8 shows the perturbation of the TM_{010}-like resonant mode frequency by a cylindrical dielectric alumina bead that is pulled through the length of the cavity in the third location available for antenna ports as represented by a black dot in Fig. 4.1. The left-side plots in Fig. 4.8 include the S_{21} scattering parameter showing the TM_{010}-like mode labeled 'a' at 5.860219 GHz and its perturbed frequency throughout the bead pull measurement. Ideally, the TM_{010}-like mode electric field does not change throughout the length of the cavity, but realistically, there is some mode localization at the endcaps most likely caused by the gaps between the rods and the endcaps. The localization does not have to be symmetric, and it is not in the present case. This asymmetry is seen by the difference in the frequency shift due to the bead perturbation in the top left plot labeled 'a' in Fig. 4.8 at bead steps of 5 and 75. Mode localization was shown not to significantly impact the form factor C [61]. The right-side plots also include the S_{21} scattering parameter in the same frequency range, but at a different rod rotation. This time, the TM_{010}-like mode labeled 'b' is at 5.881645 GHz and is mixed with the TEM mode labeled 'c' at 5.893791 GHz. These bead pull measurements show that the pure TM_{010}-like mode electric field shape is partially disrupted by the proximity of a TEM mode. These measurements help us confirm the mode we are investigating and help us determine the extent of disruption of the TM_{010}-like mode shape at mode crossings.

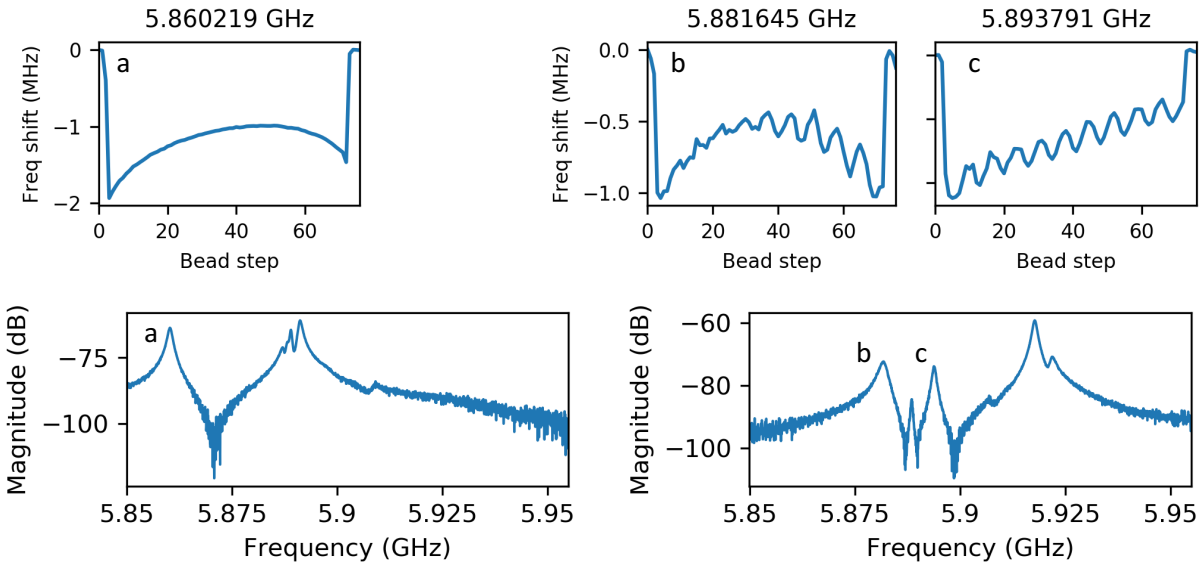

Figure 4.8: Top plots show the frequency shifts observed in bead perturbation measurements to map the electric field profile of the labeled resonant modes. Bottom plots show the S_{21} scattering parameter magnitude in units of dB at two rod rotations. The left-side plots give an example without mode mixing, while the right-side plots show the TM_{010}-like mode mixing with the tenth TEM mode at around 5.9 GHz. This mode crossing also appears in Fig. 4.7a.

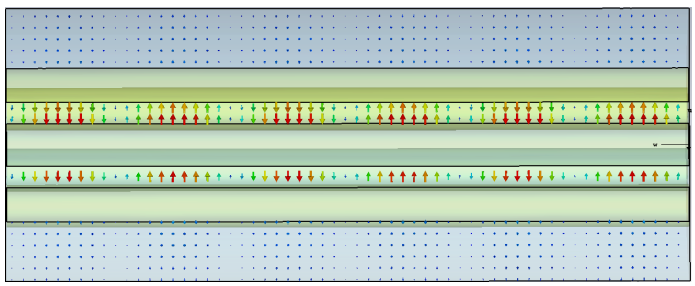

(a) Electric field of mode at 5.72 GHz.

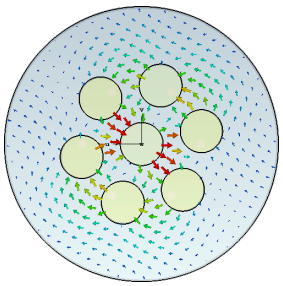

(b) Cut at $z = 5.83''$.

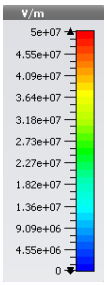

(c)

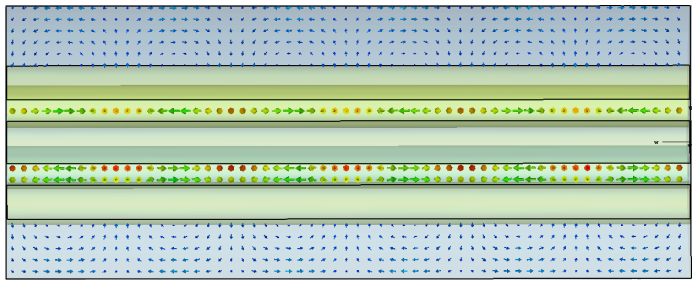

(d) Magnetic field of mode at 5.72 GHz.

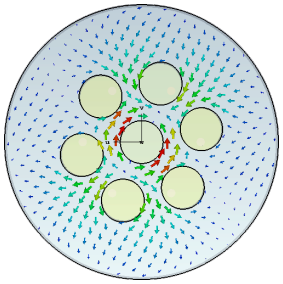

(e) Cut at $z = 5.00''$.

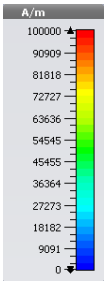

(f)

Figure 4.9: EM fields of a mode at 5.72 GHz with rods at rotation of 90° from innermost position. Scales for electric and magnetic fields are given in (c) and (f), respectively.

Chapter 5

Conclusion and future work

5.1 Conclusion

HAYSTAC is interested in searching for axions between 4 and 12 GHz. The TM_{010}-like mode in the one-rod cavity used in Phases I and II is tunable from 3.4 to 5.8 GHz. For the purpose of accessing higher frequencies, several cavity designs were considered, which are summarized in Fig. 5.1. The main considerations for comparing designs is the cavity figure of merit QC^2V^2, which depends on the quality factor, mode form factor, and cavity volume, and the severity of mode crossings throughout the tuning range of the mode of interest.

The TM_{010}-like mode in the two-rod designs did not reach higher frequencies effectively. The TM_{030}-like mode in the seven-rod design with a dielectric shell performed well in terms of the cavity figure of merit, but suffered from the high density of intruder modes in its tuning range. Perhaps using higher-order modes can be reconsidered if a photonic band gap structure is designed to act as the barrel. In the end, I found that the TM_{010}-like mode in the seven-rod cavity design is optimal for accessing 5.5 to 7.4 GHz. Based on the simulation results, the seven-rod cavity was designed, built, and tested. Throughout the tuning range, there are a few mode crossings, but the majority of the tuning range is clear.

5.2 Future work

The seven-rod cavity performs well mechanically and electromagnetically at room temperatures, but it is yet to be tested at cryogenic temperatures. Since HAYSTAC must reduce thermal noise contributions, the cavity must be cooled to below 100 mK. As discussed in Sec. 3.1, cooling will improve the quality factor of the TM_{010}-like mode in the cavity by approximately a factor of four. The effect of cooling on the mechanical motion must be tested, as well as the thermal linkage. The central rod is in contact with the endcap, and therefore is expected to cool efficiently. The other six rods have axles made of aluminum and alumina tubes. A detailed study of inserting 0.0625″ OD copper rods into each side of the six rod axles must be performed to test for changes in quality factor.

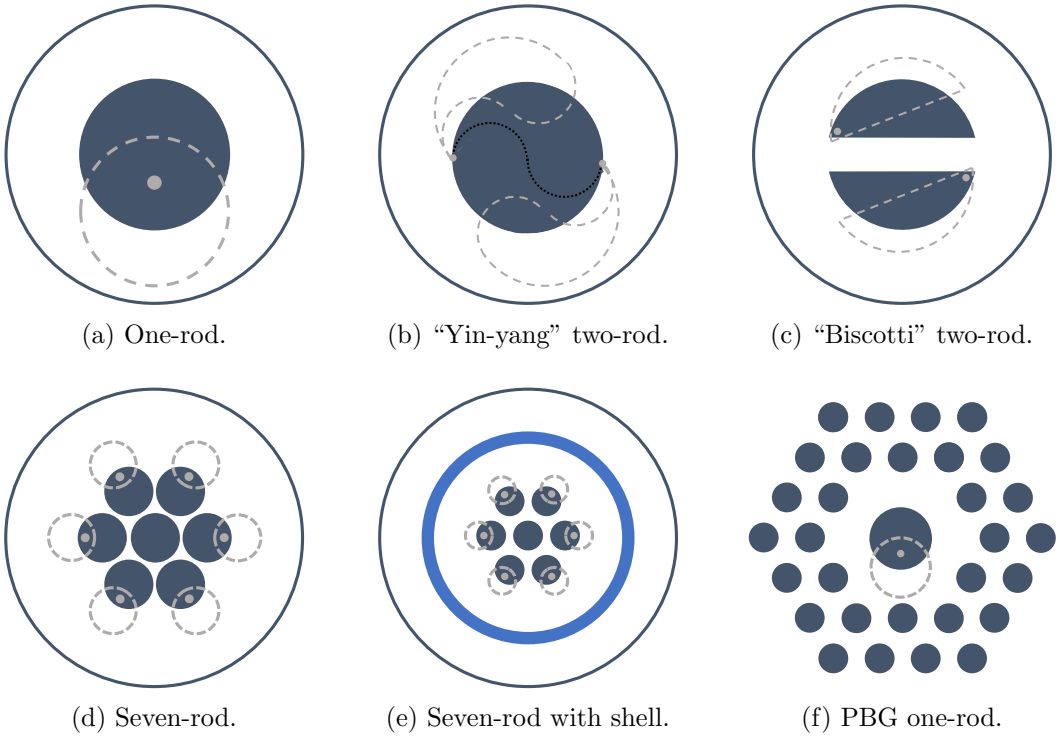

(a) One-rod. (b) "Yin-yang" two-rod. (c) "Biscotti" two-rod.

(d) Seven-rod. (e) Seven-rod with shell. (f) PBG one-rod.

Figure 5.1: Top views of selected cavity designs. Dark shapes are the conducting cavity barrel and rod outlines, small grey circles are axles around which the rods rotate, dashed lines mark rod tuning positions, and thicker blue circle in 5.1e represents the dielectric shell.

Although the seven-rod cavity provides a relatively clear tuning range of the TM_{010}-like mode, there are a few problematic mode crossings. In the one-rod cavity, we finely tune the TM_{010}-like mode resonance frequency by partially inserting a dielectric rod called the vernier. The vernier changes the frequencies of all modes and therefore the location of mode crossings. To gain access to frequencies affected by mode crossings, we must consider the possibility of incorporating a vernier into the seven-rod cavity.

The TM_{010}-like mode in the current design of the seven-rod cavity reaches a frequency of around 7.4 GHz, and further study will be necessary regarding the extendability of this scheme upward in frequency. HAYSTAC aims to find a highly optimized solution for up to 12 GHz. Future design ideas include a seven-rod design with the central rod a different size than the peripheral rods. After this, reaching beyond 12 GHz requires new ideas. One idea that our HAYSTAC group at UC Berkeley began investigating is using tunable cryogenic plasmas and matching the axion mass to a plasma frequency [71]. Since the plasma frequency does not depend on the size of the detector, large volumes are possible at higher frequencies.

Bibliography

[1] Matthias Bartelmann. "The dark Universe". In: *Rev. Mod. Phys.* 82 (1 2010), pp. 331–382. DOI: 10.1103/RevModPhys.82.331. URL: https://link.aps.org/doi/10.1103/RevModPhys.82.331.

[2] Gianfranco Bertone, Dan Hooper, and Joseph Silk. "Particle dark matter: evidence, candidates and constraints". In: *Physics Reports* 405.5 (2005), pp. 279 –390. ISSN: 0370-1573. DOI: https://doi.org/10.1016/j.physrep.2004.08.031. URL: http://www.sciencedirect.com/science/article/pii/S0370157304003515.

[3] Olivier Wantz and E. P. S. Shellard. "Axion cosmology revisited". In: *Phys. Rev. D* 82 (12 2010), p. 123508. DOI: 10.1103/PhysRevD.82.123508. URL: https://link.aps.org/doi/10.1103/PhysRevD.82.123508.

[4] G. G. Raffelt. *Stars as laboratories for fundamental physics*. 1996. ISBN: 9780226702728. URL: http://wwwth.mpp.mpg.de/members/raffelt/mypapers/199613.pdf.

[5] Stephen J. Asztalos et al. "Searches for Astrophysical and Cosmological Axions". In: *Annual Review of Nuclear and Particle Science* 56.1 (2006), pp. 293–326. DOI: 10.1146/annurev.nucl.56.080805.140513. eprint: https://doi.org/10.1146/annurev.nucl.56.080805.140513. URL: https://doi.org/10.1146/annurev.nucl.56.080805.140513.

[6] Peter W. Graham et al. "Experimental Searches for the Axion and Axion-Like Particles". In: *Annual Review of Nuclear and Particle Science* 65.1 (2015), pp. 485–514. DOI: 10.1146/annurev-nucl-102014-022120. eprint: https://doi.org/10.1146/annurev-nucl-102014-022120. URL: https://doi.org/10.1146/annurev-nucl-102014-022120.

[7] Yoshiaki Sofue and Vera Rubin. "Rotation Curves of Spiral Galaxies". In: *Annual Review of Astronomy and Astrophysics* 39.1 (2001), pp. 137–174. DOI: 10.1146/annurev.astro.39.1.137. eprint: https://doi.org/10.1146/annurev.astro.39.1.137. URL: https://doi.org/10.1146/annurev.astro.39.1.137.

[8] Vera C. Rubin and W. Kent Ford Jr. "Rotation of the Andromeda Nebula from a Spectroscopic Survey of Emission Regions". In: *Astrophys. J.* 159 (1970), pp. 379–403. DOI: 10.1086/150317.

[9] K. G. Begeman, A. H. Broeils, and R. H. Sanders. "Extended rotation curves of spiral galaxies: dark haloes and modified dynamics". In: *Monthly Notices of the Royal Astronomical Society* 249.3 (Apr. 1991), pp. 523–537. ISSN: 0035-8711. DOI: 10.1093/mnras/249.3.523. eprint: http://oup.prod.sis.lan/mnras/article-pdf/249/3/523/18160929/mnras249-0523.pdf. URL: https://doi.org/10.1093/mnras/249.3.523.

[10] M. Tanabashi et al. "Review of Particle Physics". In: *Phys. Rev. D* 98 (3 2018), p. 030001. DOI: 10.1103/PhysRevD.98.030001. URL: https://link.aps.org/doi/10.1103/PhysRevD.98.030001.

[11] Planck Collaboration et al. "Planck 2015 results - XIII. Cosmological parameters". In: *A&A* 594 (2016), A13. DOI: 10.1051/0004-6361/201525830. URL: https://doi.org/10.1051/0004-6361/201525830.

[12] Michael Dine. "Naturalness Under Stress". In: *Annual Review of Nuclear and Particle Science* 65.1 (2015), pp. 43–62. DOI: 10.1146/annurev-nucl-102014-022053. eprint: https://doi.org/10.1146/annurev-nucl-102014-022053. URL: https://doi.org/10.1146/annurev-nucl-102014-022053.

[13] Hai-Yang Cheng. "The strong CP problem revisited". In: *Physics Reports* 158.1 (1988), pp. 1 –89. ISSN: 0370-1573. DOI: https://doi.org/10.1016/0370-1573(88)90135-4. URL: http://www.sciencedirect.com/science/article/pii/0370157388901354.

[14] J. M. Pendlebury et al. "Revised experimental upper limit on the electric dipole moment of the neutron". In: *Phys. Rev. D* 92 (9 2015), p. 092003. DOI: 10.1103/PhysRevD.92.092003. URL: https://link.aps.org/doi/10.1103/PhysRevD.92.092003.

[15] R. D. Peccei and Helen R. Quinn. "CP Conservation in the Presence of Pseudoparticles". In: *Phys. Rev. Lett.* 38 (25 1977), pp. 1440–1443. DOI: 10.1103/PhysRevLett.38.1440. URL: https://link.aps.org/doi/10.1103/PhysRevLett.38.1440.

[16] R. D. Peccei and Helen R. Quinn. "Constraints imposed by CP conservation in the presence of pseudoparticles". In: *Phys. Rev. D* 16 (6 1977), pp. 1791–1797. DOI: 10.1103/PhysRevD.16.1791. URL: https://link.aps.org/doi/10.1103/PhysRevD.16.1791.

[17] Steven Weinberg. "A New Light Boson?" In: *Phys. Rev. Lett.* 40 (4 1978), pp. 223–226. DOI: 10.1103/PhysRevLett.40.223. URL: https://link.aps.org/doi/10.1103/PhysRevLett.40.223.

[18] F. Wilczek. "Problem of Strong P and T Invariance in the Presence of Instantons". In: *Phys. Rev. Lett.* 40 (5 1978), pp. 279–282. DOI: 10.1103/PhysRevLett.40.279. URL: https://link.aps.org/doi/10.1103/PhysRevLett.40.279.

[19] F. Wilczek. "The Birth of Axions". In: *Current Contents* 16 (1991), pp. 8–9.

[20] J. Gasser and H. Leutwyler. "Quark masses". In: *Physics Reports* 87.3 (1982), pp. 77 –169. ISSN: 0370-1573. DOI: https://doi.org/10.1016/0370-1573(82)90035-7. URL: http://www.sciencedirect.com/science/article/pii/0370157382900357.

[21] J. D. Bjorken et al. "Search for neutral metastable penetrating particles produced in the SLAC beam dump". In: *Phys. Rev. D* 38 (11 1988), pp. 3375–3386. DOI: 10.1103/PhysRevD.38.3375. URL: https://link.aps.org/doi/10.1103/PhysRevD.38.3375.

[22] Jihn E. Kim. "Weak-Interaction Singlet and Strong CP Invariance". In: *Phys. Rev. Lett.* 43 (2 1979), pp. 103–107. DOI: 10.1103/PhysRevLett.43.103. URL: https://link.aps.org/doi/10.1103/PhysRevLett.43.103.

[23] M.A. Shifman, A.I. Vainshtein, and V.I. Zakharov. "Can confinement ensure natural CP invariance of strong interactions?" In: *Nuclear Physics B* 166.3 (1980), pp. 493 –506. ISSN: 0550-3213. DOI: https://doi.org/10.1016/0550-3213(80)90209-6. URL: http://www.sciencedirect.com/science/article/pii/0550321380902096.

[24] A. R. Zhitnitsky. "On Possible Suppression of the Axion Hadron Interactions. (In Russian)". In: *Sov. J. Nucl. Phys.* 31 (1980). [Yad. Fiz.31,497(1980)], p. 260.

[25] Michael Dine, Willy Fischler, and Mark Srednicki. "A simple solution to the strong CP problem with a harmless axion". In: *Physics Letters B* 104.3 (1981), pp. 199 –202. ISSN: 0370-2693. DOI: https://doi.org/10.1016/0370-2693(81)90590-6. URL: http://www.sciencedirect.com/science/article/pii/0370269381905906.

[26] P. Sikivie. "The Pool-Table Analogy with Axion Physics". In: *Physics Today* 49 (12 1996), p. 22. DOI: 10.1063/1.881573.

[27] Peter W. Graham and Surjeet Rajendran. "New observables for direct detection of axion dark matter". In: *Phys. Rev. D* 88 (3 2013), p. 035023. DOI: 10.1103/PhysRevD.88.035023. URL: https://link.aps.org/doi/10.1103/PhysRevD.88.035023.

[28] Michael S. Turner. "Windows on the axion". In: *Physics Reports* 197.2 (1990), pp. 67 –97. ISSN: 0370-1573. DOI: https://doi.org/10.1016/0370-1573(90)90172-X. URL: http://www.sciencedirect.com/science/article/pii/037015739090172X.

[29] J. I. Read. "The local dark matter density". In: *Journal of Physics G: Nuclear and Particle Physics* 41 (2014), p. 063101. DOI: 10.1088/0954-3899/41/6/063101.

[30] John Preskill, Mark B. Wise, and Frank Wilczek. "Cosmology of the invisible axion". In: *Physics Letters B* 120.1 (1983), pp. 127 –132. ISSN: 0370-2693. DOI: https://doi.org/10.1016/0370-2693(83)90637-8. URL: http://www.sciencedirect.com/science/article/pii/0370269383906378.

[31] L.F. Abbott and P. Sikivie. "A cosmological bound on the invisible axion". In: *Physics Letters B* 120.1 (1983), pp. 133 –136. ISSN: 0370-2693. DOI: https://doi.org/10.1016/0370-2693(83)90638-X. URL: http://www.sciencedirect.com/science/article/pii/037026938390638X.

[32] Michael Dine and Willy Fischler. "The not-so-harmless axion". In: *Physics Letters B* 120.1 (1983), pp. 137 –141. ISSN: 0370-2693. DOI: https://doi.org/10.1016/0370-2693(83)90639-1. URL: http://www.sciencedirect.com/science/article/pii/0370269383906391.

[33] Peter W. Graham and Adam Scherlis. "Stochastic axion scenario". In: *Phys. Rev. D* 98 (3 2018), p. 035017. DOI: 10.1103/PhysRevD.98.035017. URL: https://link.aps.org/doi/10.1103/PhysRevD.98.035017.

[34] Fuminobu Takahashi, Wen Yin, and Alan H. Guth. "QCD axion window and low-scale inflation". In: *Phys. Rev. D* 98 (1 2018), p. 015042. DOI: 10.1103/PhysRevD.98.015042. URL: https://link.aps.org/doi/10.1103/PhysRevD.98.015042.

[35] P. Sikivie. "Experimental Tests of the "Invisible" Axion". In: *Phys. Rev. Lett.* 51 (1983), p. 1415. DOI: 10.1103/PhysRevLett.51.1415.

[36] Ben T. McAllister et al. "The ORGAN experiment: An axion haloscope above 15 GHz". English. In: *Physics Of The Dark Universe* 18 (Dec. 2017), pp. 67–72. ISSN: 2212-6864. DOI: 10.1016/j.dark.2017.09.010.

[37] S. DePanfilis et al. "Limits on the abundance and coupling of cosmic axions at $4.5 < m_a < 5.0\mu$eV". In: *Phys. Rev. Lett.* 59 (7 1987), pp. 839–842. DOI: 10.1103/PhysRevLett.59.839. URL: https://link.aps.org/doi/10.1103/PhysRevLett.59.839.

[38] C. Hagmann et al. "Results from a search for cosmic axions". In: *Phys. Rev. D* 42 (4 1990), pp. 1297–1300. DOI: 10.1103/PhysRevD.42.1297. URL: https://link.aps.org/doi/10.1103/PhysRevD.42.1297.

[39] Saptarshi Chaudhuri et al. "Radio for hidden-photon dark matter detection". In: *Phys. Rev. D* 92 (7 2015), p. 075012. DOI: 10.1103/PhysRevD.92.075012. URL: https://link.aps.org/doi/10.1103/PhysRevD.92.075012.

[40] Yonatan Kahn, Benjamin R. Safdi, and Jesse Thaler. "Broadband and Resonant Approaches to Axion Dark Matter Detection". In: *Phys. Rev. Lett.* 117 (14 2016), p. 141801. DOI: 10.1103/PhysRevLett.117.141801. URL: https://link.aps.org/doi/10.1103/PhysRevLett.117.141801.

[41] Saptarshi Chaudhuri et al. "Fundamental Limits of Electromagnetic Axion and Hidden-Photon Dark Matter Searches: Part I - The Quantum Limit". In: (2018). arXiv: 1803.01627 [hep-ph].

[42] Dmitry Budker et al. "Proposal for a Cosmic Axion Spin Precession Experiment (CASPEr)". In: *Phys. Rev. X* 4 (2 2014), p. 021030. DOI: 10.1103/PhysRevX.4.021030. URL: https://link.aps.org/doi/10.1103/PhysRevX.4.021030.

[43] Asimina Arvanitaki and Andrew A. Geraci. "Resonantly Detecting Axion-Mediated Forces with Nuclear Magnetic Resonance". In: *Phys. Rev. Lett.* 113 (16 2014), p. 161801. DOI: 10.1103/PhysRevLett.113.161801. URL: https://link.aps.org/doi/10.1103/PhysRevLett.113.161801.

[44] Allen Caldwell et al. "Dielectric Haloscopes: A New Way to Detect Axion Dark Matter". In: *Phys. Rev. Lett.* 118 (9 2017), p. 091801. DOI: 10.1103/PhysRevLett.118.091801. URL: https://link.aps.org/doi/10.1103/PhysRevLett.118.091801.

[45] R. Barbieri et al. "Searching for galactic axions through magnetized media: The QUAX proposal". In: *Physics of the Dark Universe* 15 (2017), pp. 135 –141. ISSN: 2212-6864. DOI: https://doi.org/10.1016/j.dark.2017.01.003. URL: http://www.sciencedirect.com/science/article/pii/S2212686417300031.

[46] K Barth et al. "CAST constraints on the axion-electron coupling". In: *Journal of Cosmology and Astroparticle Physics* 2013.05 (2013), pp. 010–010. DOI: 10.1088/1475-7516/2013/05/010. URL: https://doi.org/10.1088%2F1475-7516%2F2013%2F05%2F010.

[47] CAST Collaboration et al. "New CAST limit on the axion-photon interaction". In: *Nature Physics* 13 (2017), pp. 584 –590. DOI: 10.1038/nphys4109.

[48] E Armengaud et al. "Conceptual design of the International Axion Observatory (IAXO)". In: *Journal of Instrumentation* 9.05 (2014), T05002–T05002. DOI: 10.1088/1748-0221/9/05/t05002. URL: https://doi.org/10.1088%2F1748-0221%2F9%2F05%2Ft05002.

[49] R. Ballou et al. "New exclusion limits on scalar and pseudoscalar axionlike particles from light shining through a wall". In: *Phys. Rev. D* 92 (9 2015), p. 092002. DOI: 10.1103/PhysRevD.92.092002. URL: https://link.aps.org/doi/10.1103/PhysRevD.92.092002.

[50] R Bhre et al. "Any light particle search II — Technical Design Report". In: *Journal of Instrumentation* 8.09 (2013), T09001–T09001. DOI: 10.1088/1748-0221/8/09/t09001. URL: https://doi.org/10.1088%2F1748-0221%2F8%2F09%2Ft09001.

[51] B. M. Brubaker et al. "First Results from a Microwave Cavity Axion Search at 24 μeV". In: *Phys. Rev. Lett.* 118 (6 2017), p. 061302. DOI: 10.1103/PhysRevLett.118.061302. URL: http://link.aps.org/doi/10.1103/PhysRevLett.118.061302.

[52] L. Zhong et al. "Results from phase 1 of the HAYSTAC microwave cavity axion experiment". In: *Phys. Rev. D* 97 (9 2018), p. 092001. DOI: 10.1103/PhysRevD.97.092001. URL: https://link.aps.org/doi/10.1103/PhysRevD.97.092001.

[53] B. M. Brubaker et al. "HAYSTAC axion search analysis procedure". In: *Phys. Rev. D* 96 (12 2017), p. 123008. DOI: 10.1103/PhysRevD.96.123008. URL: https://link.aps.org/doi/10.1103/PhysRevD.96.123008.

[54] S. Al Kenany et al. "Design and operational experience of a microwave cavity axion detector for the 20-100 μeV range". In: *Nuclear Instruments and Methods in Physics Research Section A: Accelerators, Spectrometers, Detectors and Associated Equipment* 854 (2017), pp. 11 –24. ISSN: 0168-9002. DOI: https://doi.org/10.1016/j.nima.2017.02.012. URL: http://www.sciencedirect.com/science/article/pii/S0168900217301948.

[55] M. Malnou et al. "Squeezed Vacuum Used to Accelerate the Search for a Weak Classical Signal". In: *Phys. Rev. X* 9 (2 2019), p. 021023. DOI: 10.1103/PhysRevX.9.021023. URL: https://link.aps.org/doi/10.1103/PhysRevX.9.021023.

[56] H. Peng et al. "Cryogenic cavity detector for a large scale cold dark-matter axion search". In: *Nucl. Instrum. Meth.* A444 (2000), pp. 569–583. DOI: 10.1016/S0168-9002(99)00971-7.

[57] Robert Henry Dicke. "The measurement of thermal radiation at microwave frequencies". In: *Review of Scientific Instruments* 17.7 (1946), pp. 268–275.

[58] A. B. Pippard. "The surface of superconductors and normal metals at high frequencies II. The anomalous skin effect in normal metals". In: *Proc. R. Soc. Lond. A.* 191 (1947), pp. 385–399. DOI: https://doi.org/10.1098/rspa.1947.0122.

[59] C. Kittel. *Quantum Theory of Solids*. J. Wiley and Sons, 1987. ISBN: 978-0-471-62412-7.

[60] John David Jackson. *Classical electrodynamics*. 3rd ed. New York, NY: Wiley, 1999. ISBN: 9780471309321. URL: http://cdsweb.cern.ch/record/490457.

[61] Nicholas M. Rapidis, Samantha M. Lewis, and Karl A. van Bibber. "Characterization of the HAYSTAC axion dark matter search cavity using microwave measurement and simulation techniques". In: *Review of Scientific Instruments* 90.2 (2019), p. 024706. DOI: 10.1063/1.5055246.

[62] P. Sikivie. "Detection rates for "invisible"-axion searches". In: *Phys. Rev. D* 32 (11 1985), pp. 2988–2991. DOI: 10.1103/PhysRevD.32.2988.

[63] C. Hagmann et al. "Cavity design for a cosmic axion detector". In: *Review of Scientific Instruments* 61.3 (1990), pp. 1076–1085. DOI: 10.1063/1.1141427. URL: https://doi.org/10.1063/1.1141427.

[64] I. Stern et al. "Cavity design for high-frequency axion dark matter detectors". In: *Review of Scientific Instruments* 86.12 (2015), p. 123305. DOI: 10.1063/1.4938164. URL: https://doi.org/10.1063/1.4938164.

[65] C. A. Flory and R. C. Taber. "High performance distributed Bragg reflector microwave resonator". In: *IEEE Transactions on Ultrasonics, Ferroelectrics, and Frequency Control* 44.2 (1997), pp. 486–495. ISSN: 1525-8955. DOI: 10.1109/58.585133.

[66] E.I. Smirnova et al. "Simulation of photonic band gaps in metal rod lattices for microwave applications". In: *J. Appl. Phys.* 91 (2002), pp. 960–968. DOI: 10.1063/1.1426247.

[67] Samantha M. Lewis. "First Test of a Photonic Band Gap Structure for HAYSTAC". In: *Microwave Cavities and Detectors for Axion Research*. Ed. by Gianpaolo Carosi, Gray Rybka, and Karl van Bibber. Cham: Springer International Publishing, 2018, pp. 67–73. ISBN: 978-3-319-92726-8.

[68] Vincent B. Klaer and Guy D. Moore. "The dark-matter axion mass". In: *Journal of Cosmology and Astroparticle Physics* 2017.11 (2017), p. 049. URL: http://stacks.iop.org/1475-7516/2017/i=11/a=049.

[69] L. C. Maier and J. C. Slater. "Field Strength Measurements in Resonant Cavities". In: *Journal of Applied Physics* 23.1 (1952), pp. 68–77. DOI: 10.1063/1.1701980. URL: https://doi.org/10.1063/1.1701980.

[70] J. C. Slater. "Microwave Electronics". In: *Rev. Mod. Phys.* 18 (4 1946), pp. 441–512. DOI: 10.1103/RevModPhys.18.441. URL: https://link.aps.org/doi/10.1103/RevModPhys.18.441.

[71] Matthew Lawson et al. "Tunable Axion Plasma Haloscopes". In: *Phys. Rev. Lett.* 123 (14 2019), p. 141802. DOI: 10.1103/PhysRevLett.123.141802. URL: https://link.aps.org/doi/10.1103/PhysRevLett.123.141802.

Appendix A

Approximate calculations with a dielectric shell

Here we consider a cavity of height L and radius R_{cav} with a centered metal rod of radius R_{rod} and a dielectric shell with dielectric constant ϵ, inner radius R_{inner} and thickness t. The radial profile is detailed in Fig. A.1.

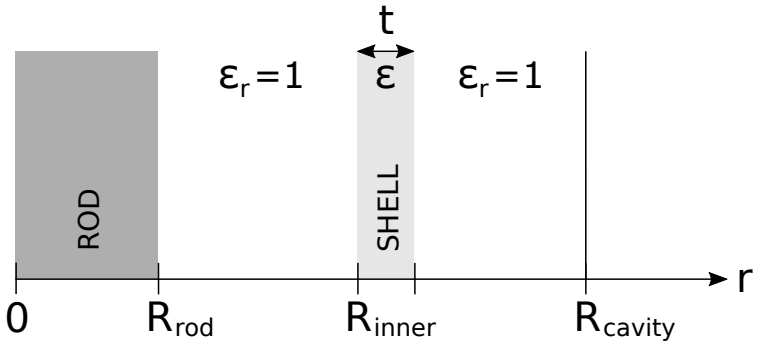

Figure A.1: Metal rod and dielectric shell positioning as a function of distance r from the cavity center at $r = 0$. Metal rod has a radius R_{rod}, dielectric shell has an inner radius R_{inner} and thickness t, and cavity has a radius R_{cav}.

A.1 Electric and Magnetic Fields

The electric field of a TM_{0n0} mode of frequency

$$\nu = \frac{c}{\lambda} = \frac{c\,2\pi}{\lambda\,2\pi} = \frac{c\,k_0}{2\pi} \tag{A.1}$$

can be approximated in the current Fig. A.1 geometry as $\vec{E} = E(r)\hat{z}$, where

$$E(r) = \begin{cases} 0 & \text{for } 0 < r < R_{\text{rod}} \\ E_1(r) = A_1 \sin\left(k_0 \left(r - R_{\text{rod}}\right)\right) & \text{for } R_{\text{rod}} < r < R_{\text{inner}} \\ E_2(r) = A_2 \sin\left(\sqrt{\epsilon}\, k_0 \left(r - R_{\text{rod}}\right) + \eta\right) & \text{for } R_{\text{inner}} < r < R_{\text{inner}} + t \\ E_3(r) = A_3 \sin\left(k_0 \left(r - R_{\text{cav}}\right)\right) & \text{for } R_{\text{inner}} + t < r < R_{\text{cav}}. \end{cases}$$

We can calculate the H-field from the E-field using the relation presented in Eq. 3.2. Then, to simplify things, we note that

$$\frac{k_0}{\mu_0\, \omega} = \frac{2\pi/\lambda}{\mu_0\, 2\pi\nu} = \frac{1}{\mu_0\, c} = \frac{\sqrt{\mu_0 \epsilon_0}}{\mu_0} = \sqrt{\frac{\epsilon_0}{\mu_0}}.$$

Then in the current geometry, the H-field is given by $\vec{H} = H(r)\hat{\phi}$ where

$$H(r) = \begin{cases} 0 & \text{for } 0 < r < R_{\text{rod}} \\ H_1(r) = A_1 \sqrt{\frac{\epsilon_0}{\mu_0}} \cos\left(k_0 \left(r - R_{\text{rod}}\right)\right) & \text{for } R_{\text{rod}} < r < R_{\text{inner}} \\ H_2(r) = A_2 \sqrt{\epsilon\, \frac{\epsilon_0}{\mu_0}} \cos\left(\sqrt{\epsilon}\, k_0 \left(r - R_{\text{rod}}\right) + \eta\right) & \text{for } R_{\text{inner}} < r < R_{\text{inner}} + t \\ H_3(r) = A_3 \sqrt{\frac{\epsilon_0}{\mu_0}} \cos\left(k_0 \left(r - R_{\text{cav}}\right)\right) & \text{for } R_{\text{inner}} + t < r < R_{\text{cav}}. \end{cases}$$

A.2 Boundary Conditions

We can solve for the unknown constants k_0, A_1, A_2, A_3, η by requiring continuous electric and magnetic fields at the boundaries of air and dielectric materials

$$\begin{aligned} E_1(R_{\text{inner}}) &= E_2(R_{\text{inner}}) \\ E_2(R_{\text{inner}} + t) &= E_3(R_{\text{inner}} + t) \\ B_1(R_{\text{inner}}) &= B_2(R_{\text{inner}}) \\ B_2(R_{\text{inner}} + t) &= B_3(R_{\text{inner}} + t). \end{aligned}$$

We plug in actual expressions to the boundary conditions

$$\begin{aligned} A_1 \sin\left(k_0 \left(R_{\text{inner}} - R_{\text{rod}}\right)\right) &= A_2 \sin\left(\sqrt{\epsilon}\, k_0 \left(R_{\text{inner}} - R_{\text{rod}}\right) + \eta\right) \\ A_2 \sin\left(\sqrt{\epsilon}\, k_0 \left(R_{\text{inner}} + t - R_{\text{rod}}\right) + \eta\right) &= A_3 \sin\left(k_0 \left(R_{\text{inner}} + t - R_{\text{cav}}\right)\right) \\ A_1 k_0 \cos\left(k_0 \left(R_{\text{inner}} - R_{\text{rod}}\right)\right) &= A_2 \sqrt{\epsilon} k_0 \cos\left(\sqrt{\epsilon}\, k_0 \left(R_{\text{inner}} - R_{\text{rod}}\right) + \eta\right) \\ A_2 \sqrt{\epsilon} k_0 \cos\left(\sqrt{\epsilon}\, k_0 \left(R_{\text{inner}} + t - R_{\text{rod}}\right) + \eta\right) &= A_3 k_0 \cos\left(k_0 \left(R_{\text{inner}} + t - R_{\text{cav}}\right)\right). \end{aligned}$$

We can combine the 1st with 3rd and 2nd with 4th conditions to get

$$\tan k_0 (R_{\text{inner}} - R_{\text{rod}}) = \frac{1}{\sqrt{\epsilon}} \tan \left(\sqrt{\epsilon}\, k_0 (R_{\text{inner}} - R_{\text{rod}}) + \eta \right)$$
$$\frac{1}{\sqrt{\epsilon}} \tan \left(\sqrt{\epsilon}\, k_0 (R_{\text{inner}} + t - R_{\text{rod}}) + \eta \right) = \tan k_0 (R_{\text{inner}} + t - R_{\text{cav}}).$$

Then we apply some trigonometric identities

$$\sqrt{\epsilon} \tan k_0 (R_{\text{inner}} - R_{\text{rod}}) = \frac{\tan \left(\sqrt{\epsilon}\, k_0 (R_{\text{inner}} - R_{\text{rod}}) \right) + \tan \eta}{1 - \tan \left(\sqrt{\epsilon}\, k_0 (R_{\text{inner}} - R_{\text{rod}}) \right) \tan \eta}$$
$$\frac{\tan \left(\sqrt{\epsilon}\, k_0 (R_{\text{inner}} + t - R_{\text{rod}}) \right) + \tan \eta}{1 - \tan \left(\sqrt{\epsilon}\, k_0 (R_{\text{inner}} + t - R_{\text{rod}}) \right) \tan \eta} = \sqrt{\epsilon} \tan k_0 (R_{\text{inner}} + t - R_{\text{cav}}).$$

Finally, we can solve for η in both expressions.

$$\begin{aligned} \tan \eta &= \frac{\sqrt{\epsilon} \tan k_0 (R_{\text{inner}} - R_{\text{rod}}) - \tan \left(\sqrt{\epsilon}\, k_0 (R_{\text{inner}} - R_{\text{rod}}) \right)}{1 + \sqrt{\epsilon} \tan k_0 (R_{\text{inner}} - R_{\text{rod}}) \tan \left(\sqrt{\epsilon}\, k_0 (R_{\text{inner}} - R_{\text{rod}}) \right)} \\ \tan \eta &= \frac{\sqrt{\epsilon} \tan k_0 (R_{\text{inner}} + t - R_{\text{rod}}) - \tan \left(\sqrt{\epsilon}\, k_0 (R_{\text{inner}} + t - R_{\text{cav}}) \right)}{1 + \sqrt{\epsilon} \tan k_0 (R_{\text{inner}} + t - R_{\text{rod}}) \tan \left(\sqrt{\epsilon}\, k_0 (R_{\text{inner}} + t - R_{\text{cav}}) \right)}. \end{aligned} \tag{A.2}$$

Now we can set both of these expressions equal to each other, plug in specific values of ϵ, R_{inner}, R_{rod}, R_{cav}, and t, then solve for k_0. There will be several possible solutions with the nth solution corresponding to the TM_{0n0} mode. The resonance frequency is given by

$$\nu = \frac{c\, k_0}{2\pi}.$$

Using the k_0 we found, we can now go back and apply the requirement of continuous electric and magnetic fields, set $A_1 = 1$ and solve for η, A_2 and A_3.

A.3 Evaluation

Now that we have outlined ways to calculate A_1, A_2, A_3, η, and k_0, we can choose values for the other parameters. For the following evaluations, we choose the parameter values consistent with a copper cavity, summarized in Table A.1.

For each selection of R_{rod}, R_{inner}, and t, we can calculate the resonance frequency ν, quality factor Q, and form factor C using Eq. A.1, Eq. 3.4, and Eq. 3.9, respectively. The quality factor is not well-predicted by the sinusoidal approximations, but other quantities are well-predicted, as shown in Table A.2.

We can choose, for example, a rod size, and vary shell position R_{inner} and thickness t to predict resonance frequency and optimize for form factor, as shown in Fig. A.2a and Fig. A.2b, respectively.

Table A.1: Constants and variables used in the calculations here.

Constant or Variable	Description	Value
R_{rod}	rod radius	varies
R_{inner}	shell inner radius	varies
t	shell thickness	varies
R_{cav}	cavity radius	$2''$
$\mu_{\text{Cu}} = \mu_0$	vacuum permeability	$4\pi \times 10^{-7}$ H/m
$\epsilon_{\text{Cu}} = \epsilon_0$	permittivity of free space	8.854×10^{-12} F/m
$c = 1/\sqrt{\mu_0\,\epsilon_0}$	speed of light	3×10^8 m/s
σ_{Cu}	conductivity	$1/\left(1.69\,\mu\Omega\,\text{cm}\right)$
$\epsilon = \epsilon_{\text{sapphire}}$	permittivity of sapphire	10

Table A.2: Predictions of the TM_{030}-like mode resonance frequency, quality factor, and form factor in a cavity with a dielectric shell. Comparison of values predicted by CST MWS simulations and calculations using a sinusoidal approximation.

R_{rod} (mm)	R_{inner} (mm)	t (mm)		ν_{030} (GHz)	Q_{030}	C_{030}
12.7	25.9	1	calculation	11.63	29623	0.135
12.7	25.9	1	simulation	11.61	21500	0.129
12.7	25.4	1	calculation	11.75	29556	0.107
12.7	25.4	1	simulation	11.72	22669	0.111
12.7	25.4	2	calculation	11.43	29947	0.163
12.7	25.4	2	simulation	11.38	22958	0.152
12.7	25.4	5	calculation	9.25	24933	0.443
12.7	25.4	5	simulation	9.23	36702	0.388

shell thickness (mm)	shell thickness (inch)	shell inner radius (mm)	shell inner radius (inch)	2.54	5.08	7.62	10.16	12.7	15.24	17.78	20.32	22.86	25.4
				0.10	0.2	0.3	0.4	0.5	0.6	0.7	0.8	0.9	1.0
		13.97	0.55	9.28	9.13	8.02	6.80	6.45	6.40	5.99	5.44	4.95	4.55
		15.24	0.6	9.35	9.16	7.64	6.67	6.52	6.36	5.82	5.26	4.80	4.42
		16.51	0.65	9.58	9.19	7.46	6.71	6.66	6.33	5.71	5.15	4.70	4.34
		17.78	0.7	9.89	9.21	7.41	6.86	6.81	6.30	5.64	5.08	4.64	4.29
		19.05	0.75	10.23	9.23	7.45	7.07	6.94	6.29	5.60	5.04	4.61	4.28
		20.32	0.8	10.60	9.24	7.55	7.32	7.05	6.28	5.57	5.02	4.60	4.29
		21.59	0.85	10.99	9.24	7.72	7.59	7.12	6.27	5.56	5.01	4.61	4.34
		22.86	0.9	11.34	9.23	7.95	7.86	7.17	6.27	5.55	5.02	4.64	4.42
		24.13	0.95	11.49	9.22	8.23	8.09	7.19	6.27	5.56	5.04	4.70	4.55
		25.4	1	11.13	9.20	8.55	8.24	7.20	6.27	5.57	5.08	4.80	x
		26.67	1.05	10.51	9.16	8.86	8.30	7.19	6.27	5.60	5.15	4.95	x
		27.94	1.1	9.91	9.13	9.02	8.24	7.17	6.28	5.65	5.26	x	x
		29.21	1.15	9.46	9.12	8.86	8.09	7.12	6.29	5.71	5.44	x	x
		30.48	1.2	9.27	9.13	8.55	7.86	7.05	6.30	5.82	x	x	x
		31.75	1.25	9.46	9.16	8.23	7.59	6.94	6.33	5.99	x	x	x
		33.02	1.3	9.91	9.20	7.95	7.32	6.81	6.36	x	x	x	x
		34.29	1.35	10.51	9.22	7.72	7.07	6.66	6.40	x	x	x	x
		35.56	1.4	11.13	9.23	7.55	6.86	6.52	x	x	x	x	x
		36.83	1.45	11.49	9.24	7.45	6.71	6.45	x	x	x	x	x
		38.1	1.5	11.34	9.24	7.42	6.67	x	x	x	x	x	x
		39.37	1.55	10.99	9.23	7.46	6.80	x	x	x	x	x	x
		40.64	1.6	10.60	9.21	7.64	x	x	x	x	x	x	x
		41.91	1.65	10.23	9.19	8.02	x	x	x	x	x	x	x
		43.18	1.7	9.89	9.16	x	x	x	x	x	x	x	x
		44.45	1.75	9.58	9.13	x	x	x	x	x	x	x	x
		45.72	1.8	9.35	x	x	x	x	x	x	x	x	x
		46.99	1.85	9.28	x	x	x	x	x	x	x	x	x

(a) Frequency f_{030} (GHz).

shell thickness (mm)	shell thickness (inch)	shell inner radius (mm)	shell inner radius (inch)	2.54	5.08	7.62	10.16	12.7	15.24	17.78	20.32	22.86	25.4
				0.10	0.2	0.3	0.4	0.5	0.6	0.7	0.8	0.9	1.0
		13.97	0.55	0.053	0.053	0.154	0.449	0.566	0.556	0.462	0.336	0.244	0.181
		15.24	0.6	0.050	0.059	0.244	0.517	0.566	0.527	0.404	0.290	0.212	0.159
		16.51	0.65	0.047	0.070	0.327	0.542	0.557	0.487	0.356	0.255	0.187	0.142
		17.78	0.7	0.044	0.089	0.395	0.549	0.543	0.445	0.316	0.227	0.168	0.129
		19.05	0.75	0.043	0.118	0.449	0.547	0.524	0.403	0.284	0.206	0.154	0.120
		20.32	0.8	0.043	0.159	0.487	0.542	0.500	0.366	0.258	0.189	0.143	0.114
		21.59	0.85	0.046	0.214	0.513	0.537	0.471	0.334	0.238	0.175	0.135	0.113
		22.86	0.9	0.060	0.283	0.528	0.534	0.441	0.308	0.222	0.166	0.131	0.115
		24.13	0.95	0.106	0.365	0.540	0.533	0.411	0.288	0.210	0.161	0.132	0.123
		25.40	1	0.191	0.453	0.553	0.531	0.387	0.275	0.204	0.159	0.138	x
		26.67	1.05	0.265	0.537	0.580	0.517	0.369	0.267	0.202	0.164	0.150	x
		27.94	1.1	0.356	0.598	0.603	0.481	0.357	0.266	0.206	0.175	x	x
		29.21	1.15	0.484	0.622	0.538	0.435	0.352	0.272	0.218	0.197	x	x
		30.48	1.2	0.577	0.599	0.465	0.398	0.350	0.285	0.240	x	x	x
		31.75	1.25	0.526	0.533	0.423	0.376	0.351	0.304	0.276	x	x	x
		33.02	1.3	0.444	0.438	0.395	0.366	0.353	0.329	x	x	x	x
		34.29	1.35	0.368	0.331	0.367	0.360	0.356	0.351	x	x	x	x
		35.56	1.4	0.271	0.226	0.328	0.355	0.360	x	x	x	x	x
		36.83	1.45	0.110	0.136	0.275	0.342	0.359	x	x	x	x	x
		38.10	1.5	0.014	0.068	0.208	0.308	x	x	x	x	x	x
		39.37	1.55	0.0001	0.0239	0.134	0.229	x	x	x	x	x	x
		40.64	1.6	0.0022	0.0031	0.064	x	x	x	x	x	x	x
		41.91	1.65	0.0069	0.0010	0.012	x	x	x	x	x	x	x
		43.18	1.7	0.0119	0.0099	x	x	x	x	x	x	x	x
		44.45	1.75	0.0162	0.0206	x	x	x	x	x	x	x	x
		45.72	1.8	0.0183	x	x	x	x	x	x	x	x	x
		46.99	1.85	0.0127	x	x	x	x	x	x	x	x	x

(b) Form factor C_{030}.

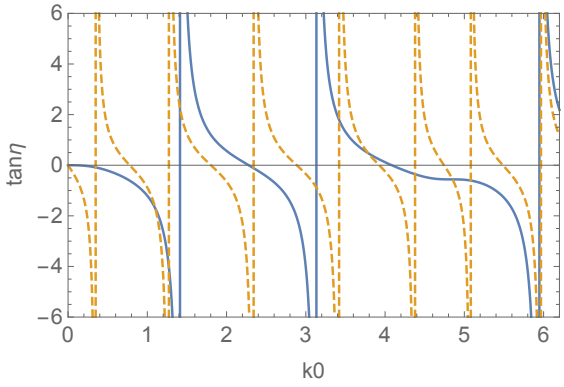

(c) $R_{\text{inner}} = 1.15''$ and $t = 0.2''$.

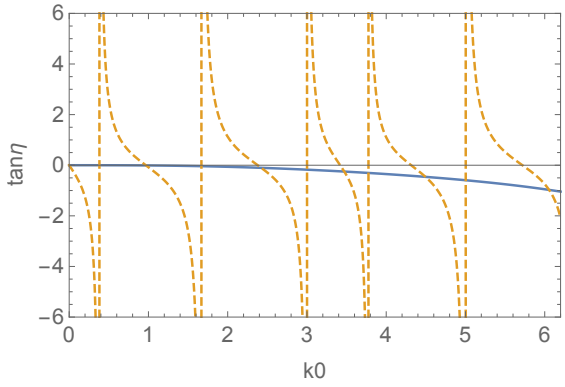

(d) $R_{\text{inner}} = 0.6''$ and $t = 0.5''$.

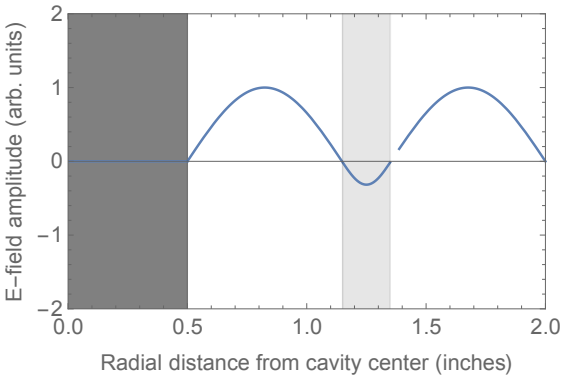

(e) $R_{\text{inner}} = 1.15''$ and $t = 0.2''$.

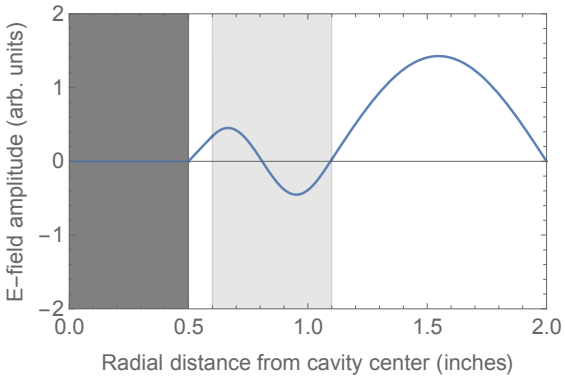

(f) $R_{\text{inner}} = 0.6''$ and $t = 0.5''$.

Figure A.2: Predictions of TM_{030}-like (a) frequency and (b) form factor with central rod $R_{\text{rod}} = 0.5''$ and varying shell inner radius R_{inner} and thickness t. Solutions in (c) and (d) plot the two expressions in Eq. A.2. The nth intersection of the expressions corresponds to the k_0 of the TM_{0n0}-like mode. Electric field amplitude as a function of radius is shown for (e) optimized C_{030} and (f) unoptimized C_{030}, corresponding to the 3rd intersections found in (c) and (d), respectively.

Appendix B

Assembly procedure for 7-rod cavity

Here I describe the standard operating procedure for assembling the seven-rod cavity described in Ch. 4. The trick is to have all bearings in place before connecting and engaging the gears. Although this order of operations complicates reaching through the top hat to adjust the gears, it ensures good alignment and prevents excessive stress on the delicate alumina axles. The instructions below use components described in Table B.1 and assume that all rods are already assembled; the six peripheral rods are glued to the alumina axles as well as the steel axles. Please handle all parts carefully, especially the brittle alumina axles.

1. Attach the bottom endcap onto the barrel with ten screws and washers (use a torque wrench to achieve < 5 in.-lbs.), placed in every other appropriate hole. The bearings on the bottom endcap should be in their place.

2. Position the cavity vertically (for example, on a ring platform) with the attached endcap on the bottom.

3. Insert the seven rods and the alignment tool into the cavity. Longer axles should be on top and shorter ones should go through holes in the bottom endcap. The central rod should fit in its designated middle groove. Your view should resemble that in Fig. 4.3g, except with the longer steel rods on top instead.

4. Carefully slip the top endcap onto the barrel. Make sure each of the tuning rods goes through its respective hole and both endcaps are aligned properly, especially with respect to each other. Dowel pins and bead pull thru holes should help guide alignment.

5. Attach the top endcap onto the barrel with two dowel pins and ten screws and washers (use two passes with a torque wrench to achieve 5 then 10 in.-lbs.). Make sure to tighten the screws in a star pattern.

6. Attach the anti-backlash gears onto the central shaft and place the shaft in the bearing on the top endcap.

7. Carefully screw the gears onto the rest of the rods in their roughly correct locations, without connecting them, but making sure to allow access to the gear set-screws through the top hat.

8. Screw the top hat onto the top endcap.

9. Attach the bearings and collars onto the rods near the top hat. If the gears don't connect, try unscrewing the top hat and wiggling.

10. With all sets of bearings in place (at the top and bottom of the cavity) and the top hat assembled, connect the gears.

11. Flip the cavity around, and remove the bottom endcap.

12. Remove the alignment device.

13. Re-attach the bottom endcap with two dowel pins and ten screws and washers (use two passes with torque wrench to achieve 5 then 10 in.-lbs.).

14. Attach the bearings and collars to the rods near the bottom endcap.

15. Flip the cavity around once again.

16. Fix all the rods to their desired vertical location to achieve desired gaps. One way to do this is to push the rods all the way down and tighten the top collars. Then insert a leaf gauge matching the desired bottom gap size between top collars and cavity top and tighten the bottom collars. Now the bottom gaps are set. Loosen the top collars, push the rods as far up as they will go, and retighten the top collars to set the top gaps.

17. Optional: string the bead through the cavity for performing bead perturbation measurements. It is easiest to get the spring through first.

18. Screw on the antenna ports and place the antennas in until they are weakly coupled.

19. Begin testing.

Table B.1: A detailed list of components that together make up the seven-rod cavity. The rods, barrel, endcaps, and top hat were coated with copper and annealed after machining.

Component	Dimensions / Description	Material
Six rods	0.625″ OD, 9.98″ length; details in Fig. B.1	6061 T6 Aluminum
- top axles	0.25″ OD, 2.25″ length; details in Fig. B.2	304 Stainless Steel
- bottom axles	0.25″ OD, 1″ length; details in Fig. B.3	304 Stainless Steel
- alumina axles	0.125″ OD, $\sim$ 1″ length; details in Fig. B.4	Nonporous Alumina
Central rod	0.625″ OD, 10.15″ length; details in Fig. B.5	6061 T6 Aluminum
Barrel	4″ ID, 4.5″ OD at the edges and 4.25″ OD at center, 10″ length and twenty No. 4 holes; details in Fig. B.6	304 Stainless Steel
Bottom endcap	4.5” OD with various holes; details in Fig. B.7	304 Stainless Steel
Top endcap	4.5” OD with various holes; details in Fig. B.8	304 Stainless Steel
Tophat	3.862″ OD, 1.5″ length; detailed drawing in Fig. B.9	304 Stainless Steel
Driveshaft	0.25″ OD, 3.5″ length; details in Fig. B.10	304 Stainless Steel
Gears	S1066Z-064S056 at SDP/SI (64 dia. pitch, 56 teeth, .125″ face width, .875″ pitch dia., .25″ bore), S9716A-Z7E056-P (St. St. body & hub)	303 Stainless Steel
Collars	.25″ ID with set screws	
Bearings	SR168(X) AF2 at Boca Bearing (.25″ ID, .375″ OD, .125″ width)	440C Stainless Steel
Screws	barrel: forty 4-40 (endcaps); top endcap: four 6-32 (top hat), six 8-32 (antenna mounts); top hat: three 1/4-28 (bead pull mount)	
Washers	At Yale, we’ll use Belville washers instead to mediate effects of changing temperature.	

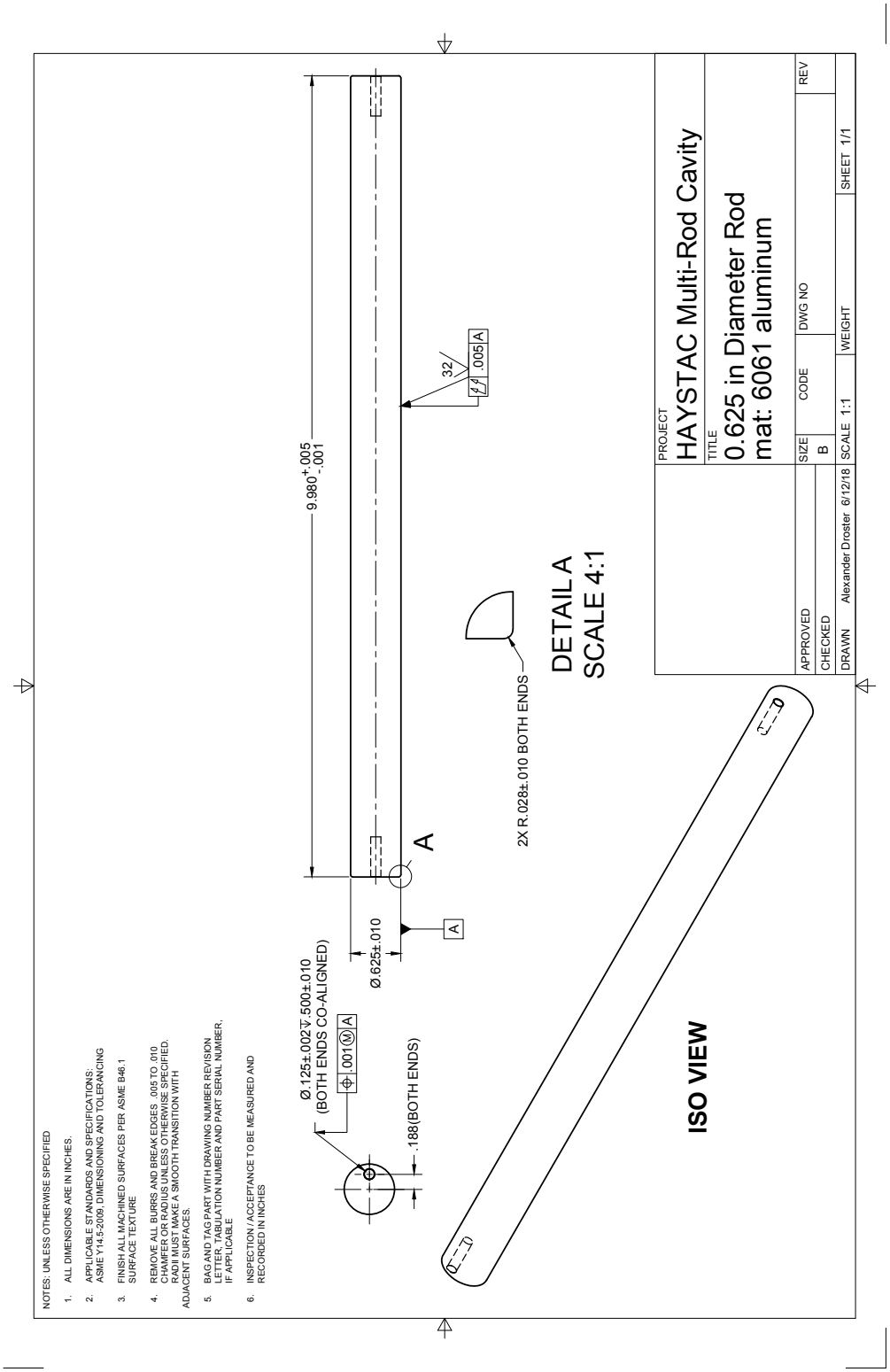

Figure B.1: CAD drawing of one of the six rods in the seven-rod cavity.

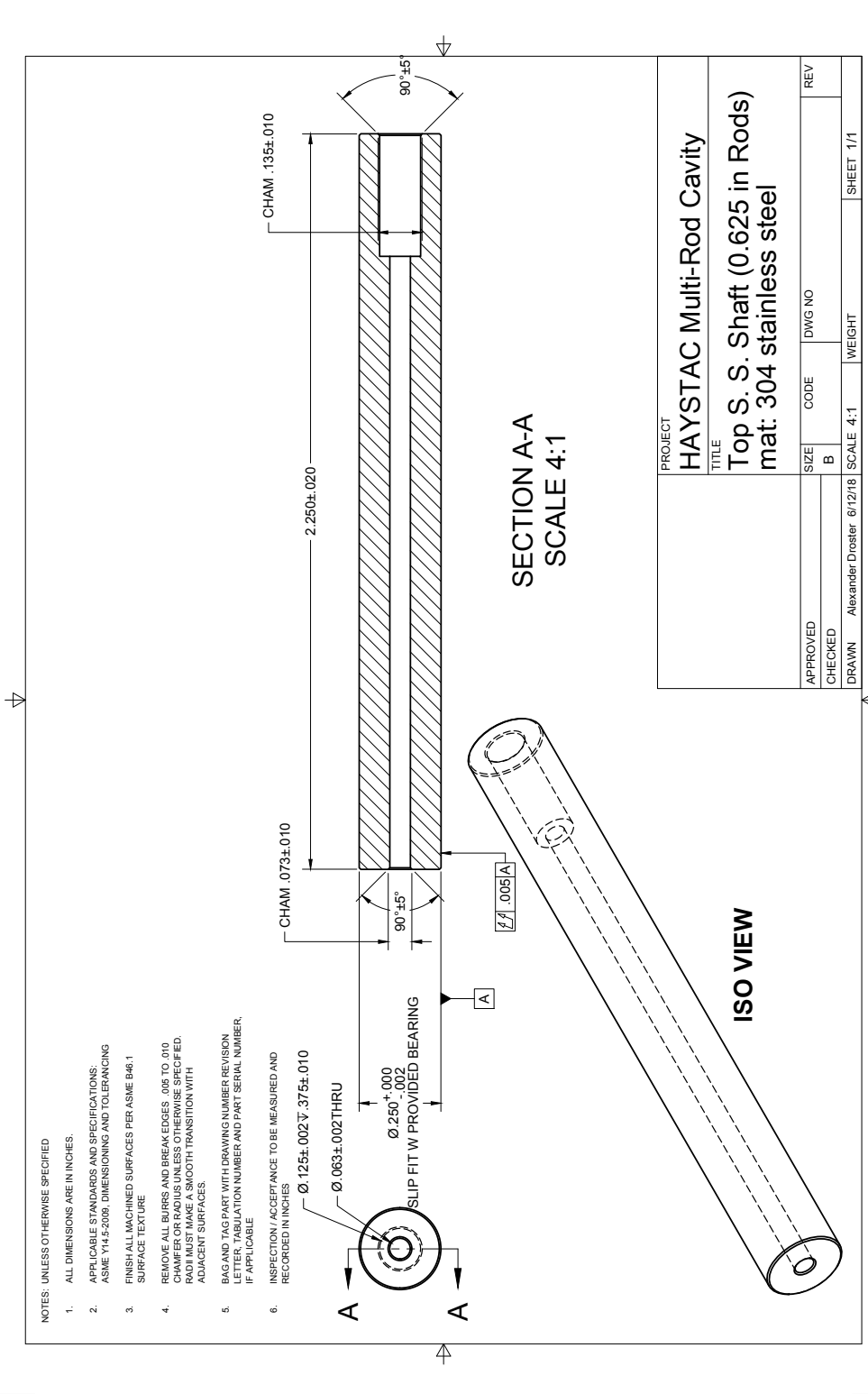

Figure B.2: CAD drawing of one of the six top aluminum axles in the seven-rod cavity.

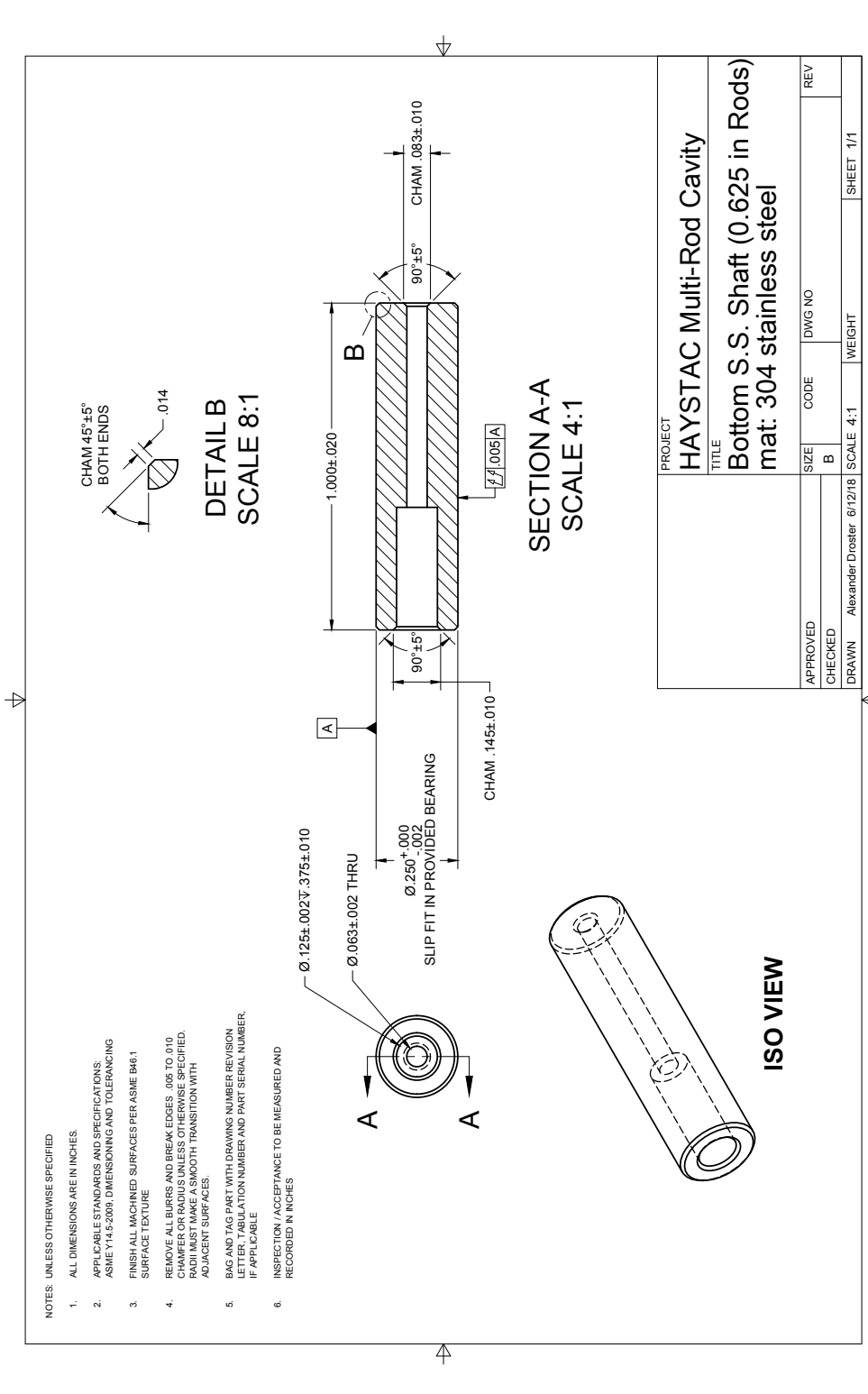

Figure B.3: CAD drawing of one of the six bottom aluminum axles in the seven-rod cavity.

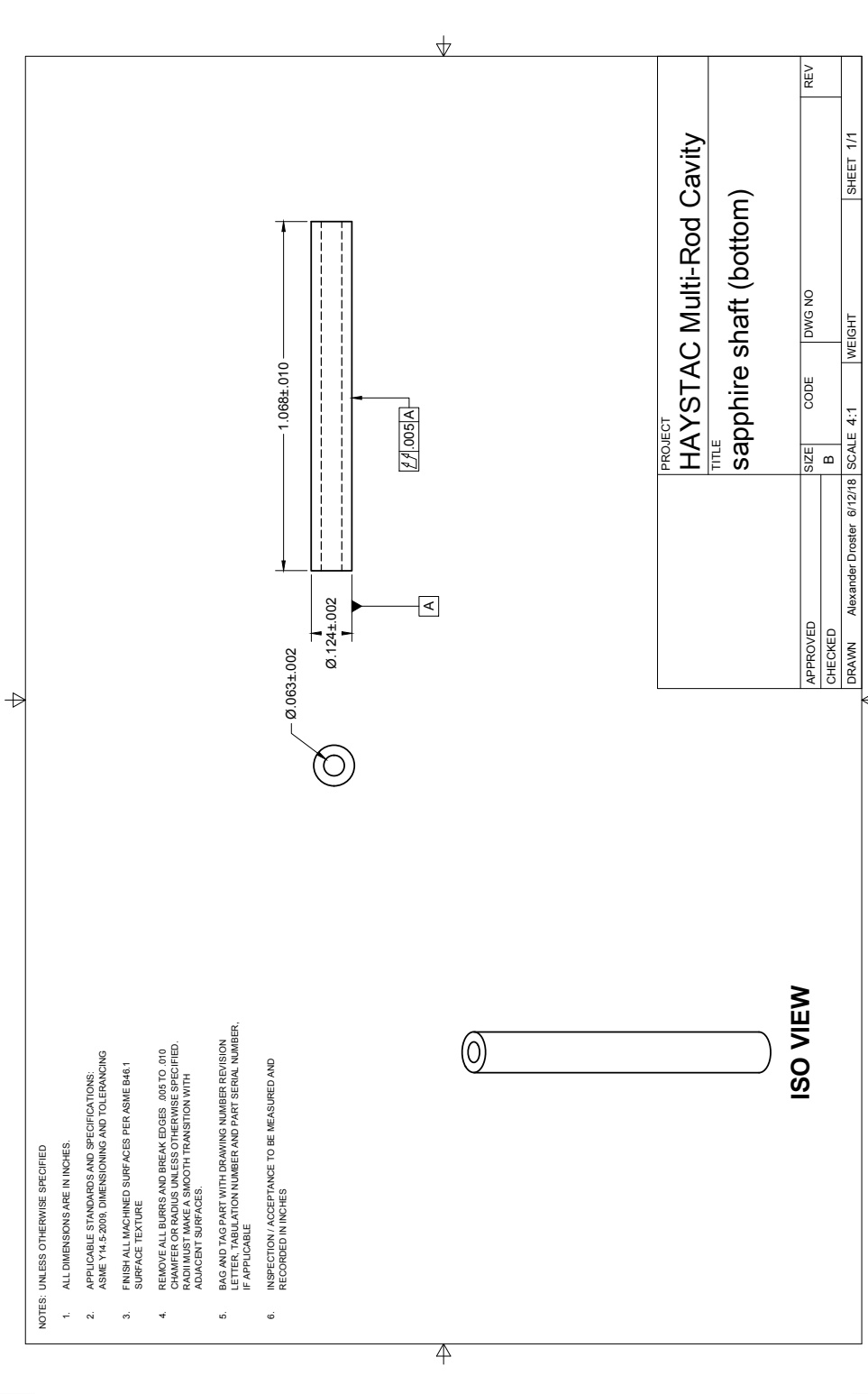

Figure B.4: CAD drawing of one of twelve alumina axles in the seven-rod cavity.

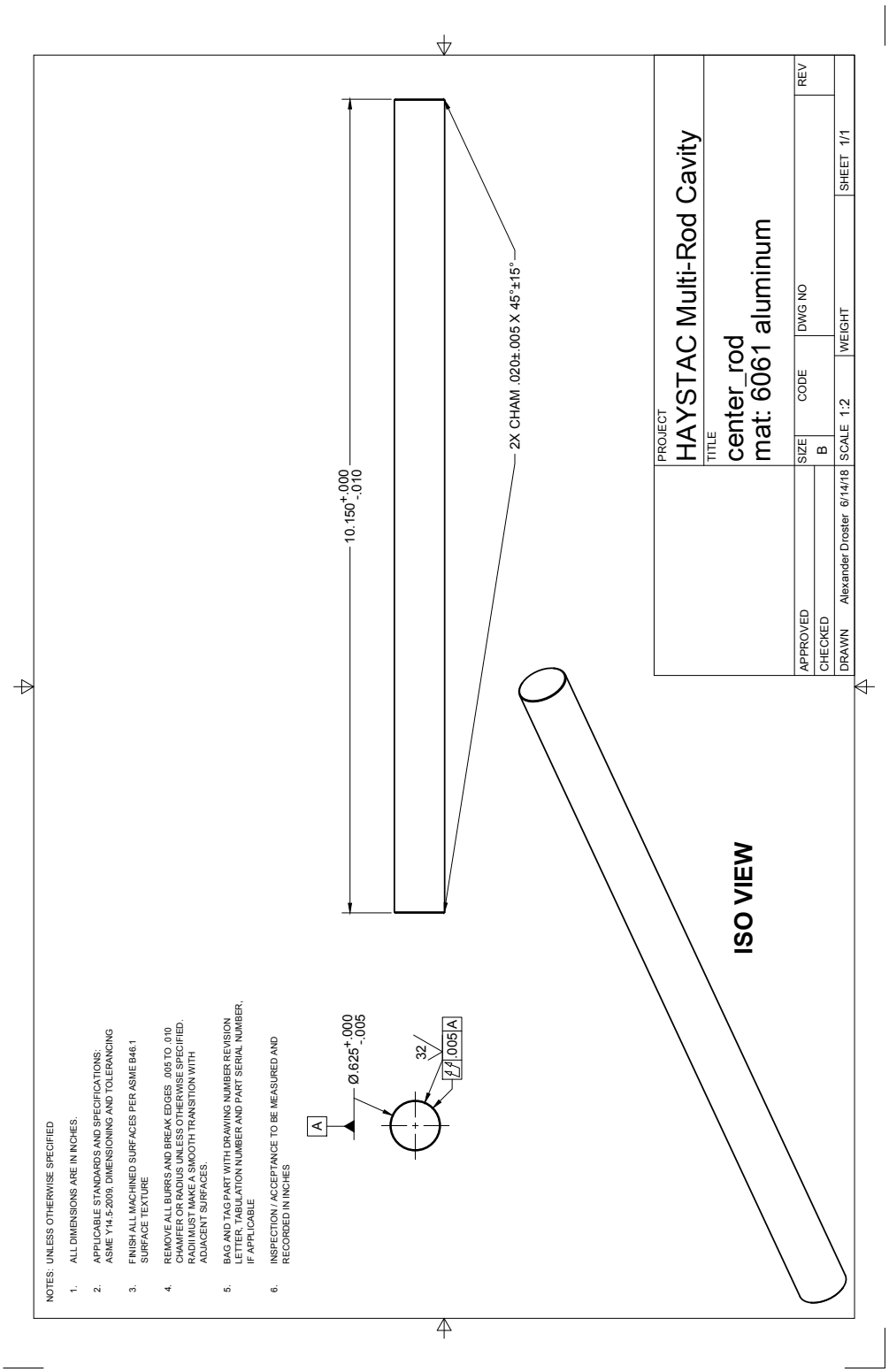

Figure B.5: CAD drawing of the central rod in the seven-rod cavity.

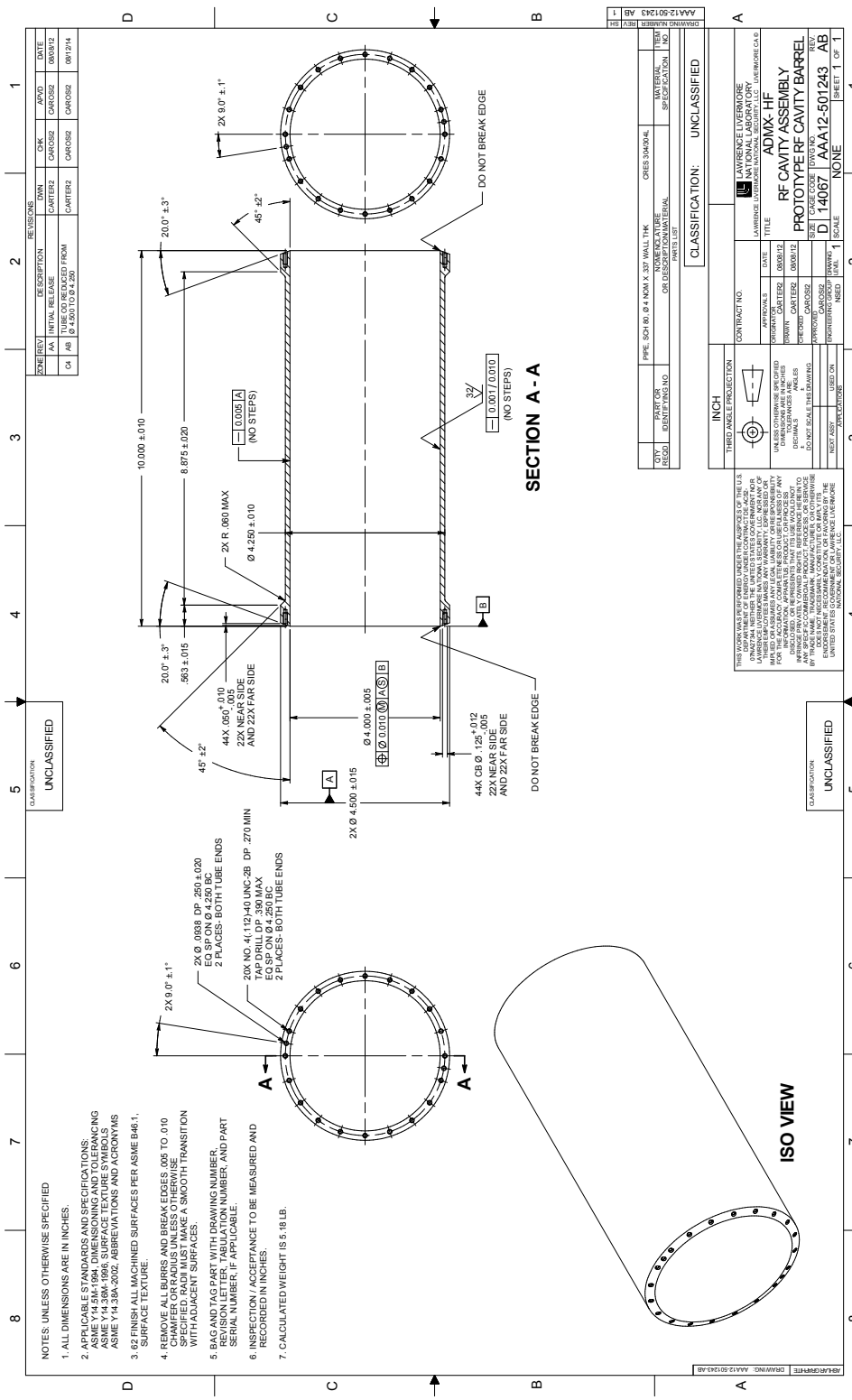

Figure B.6: CAD drawing of the seven-rod cavity barrel, which is the same as the barrel of the one-rod cavity used in Phases I and II of HAYSTAC.

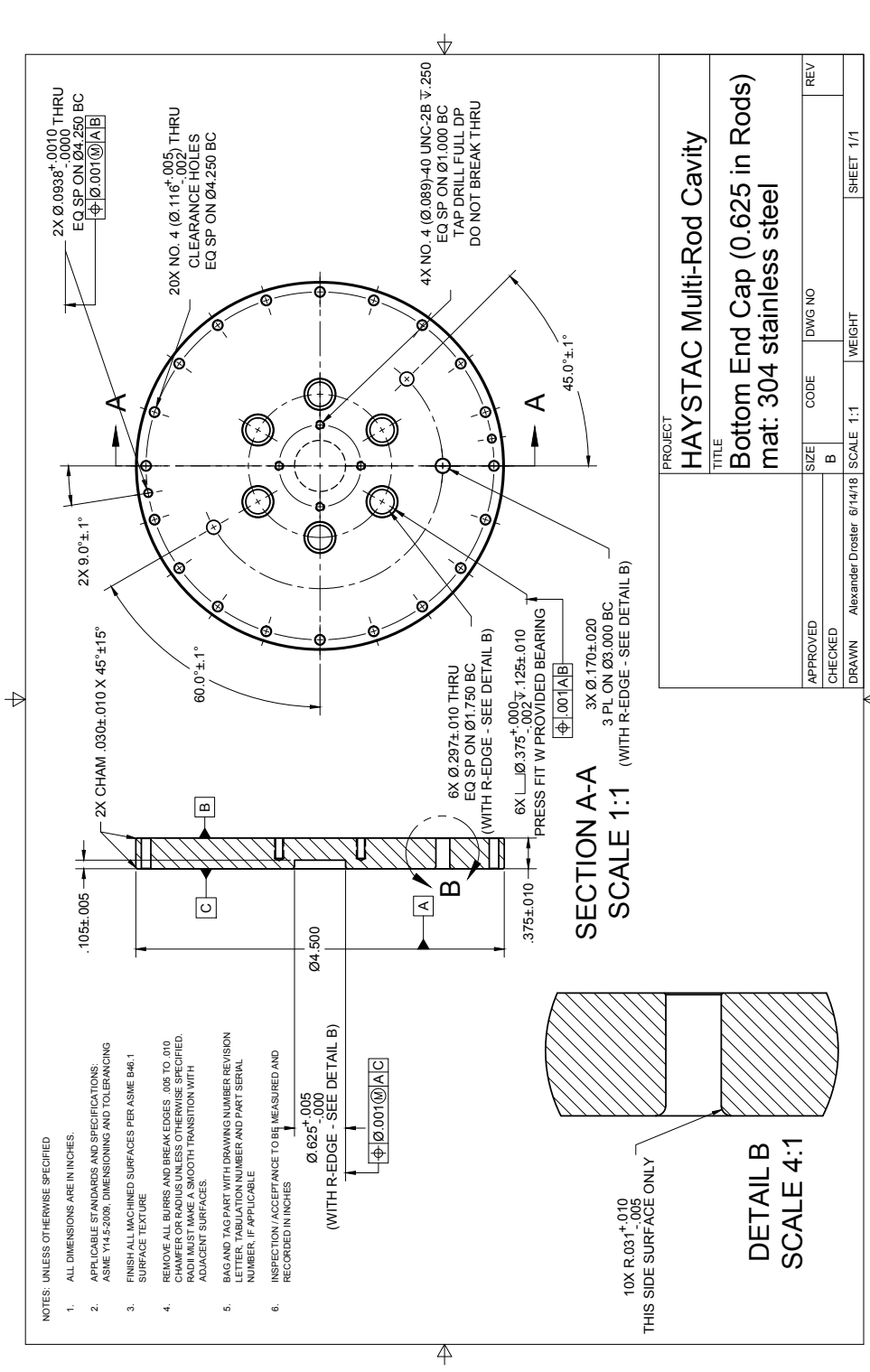

Figure B.7: CAD drawing of the bottom endcap in the seven-rod cavity.

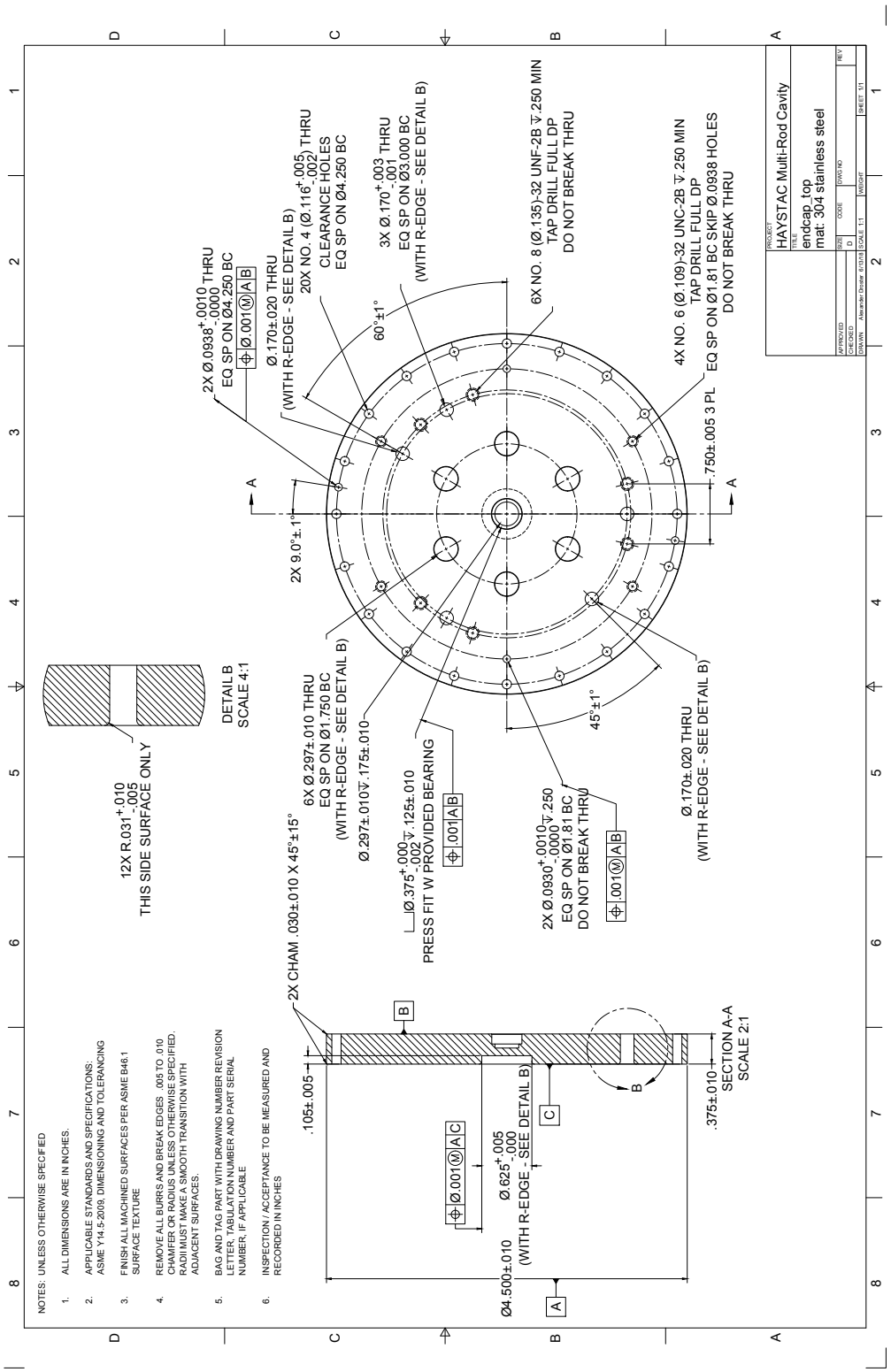

Figure B.8: CAD drawing of the top endcap in the seven-rod cavity.

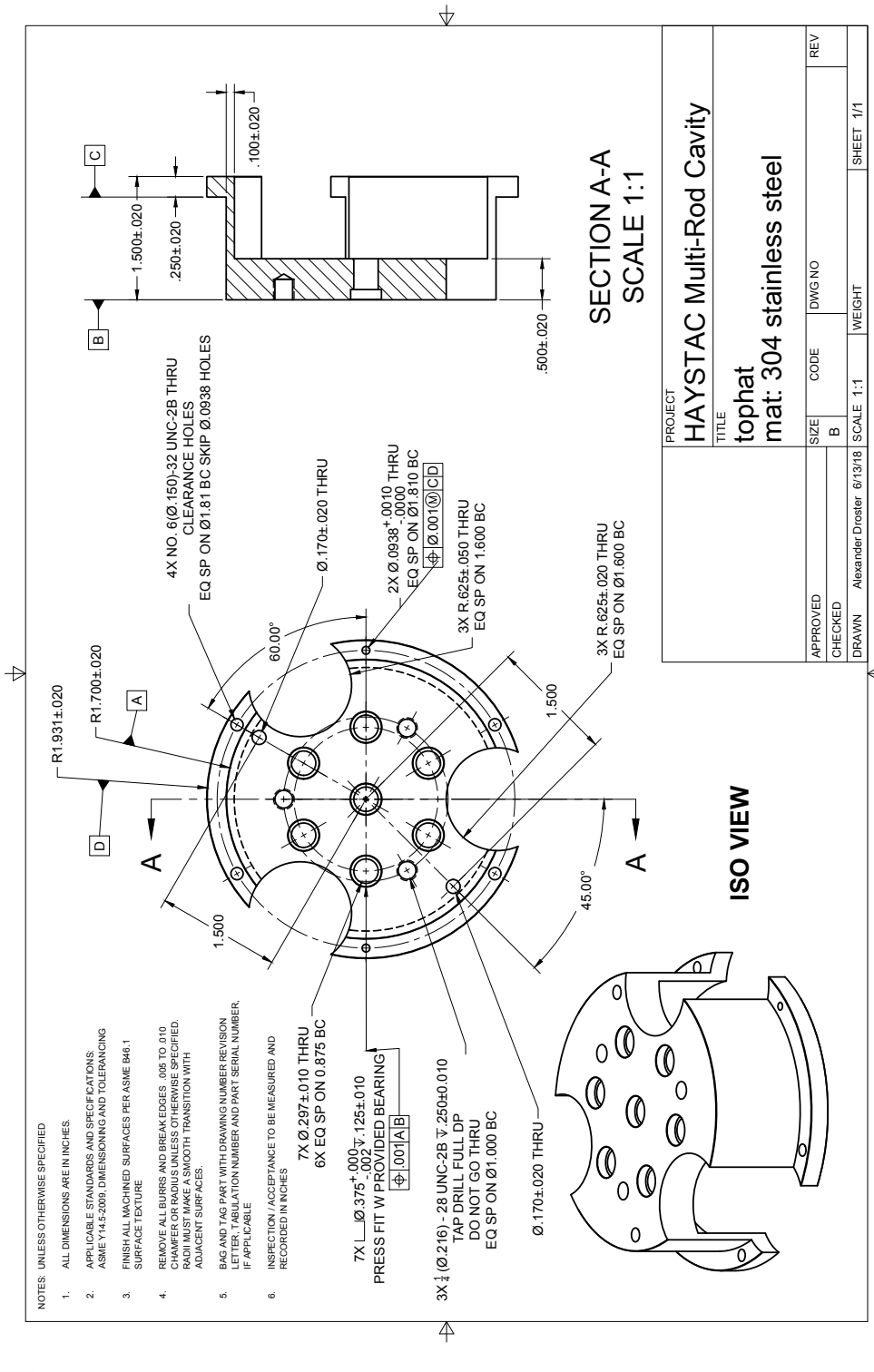

Figure B.9: CAD drawing of the top hat in the seven-rod cavity.

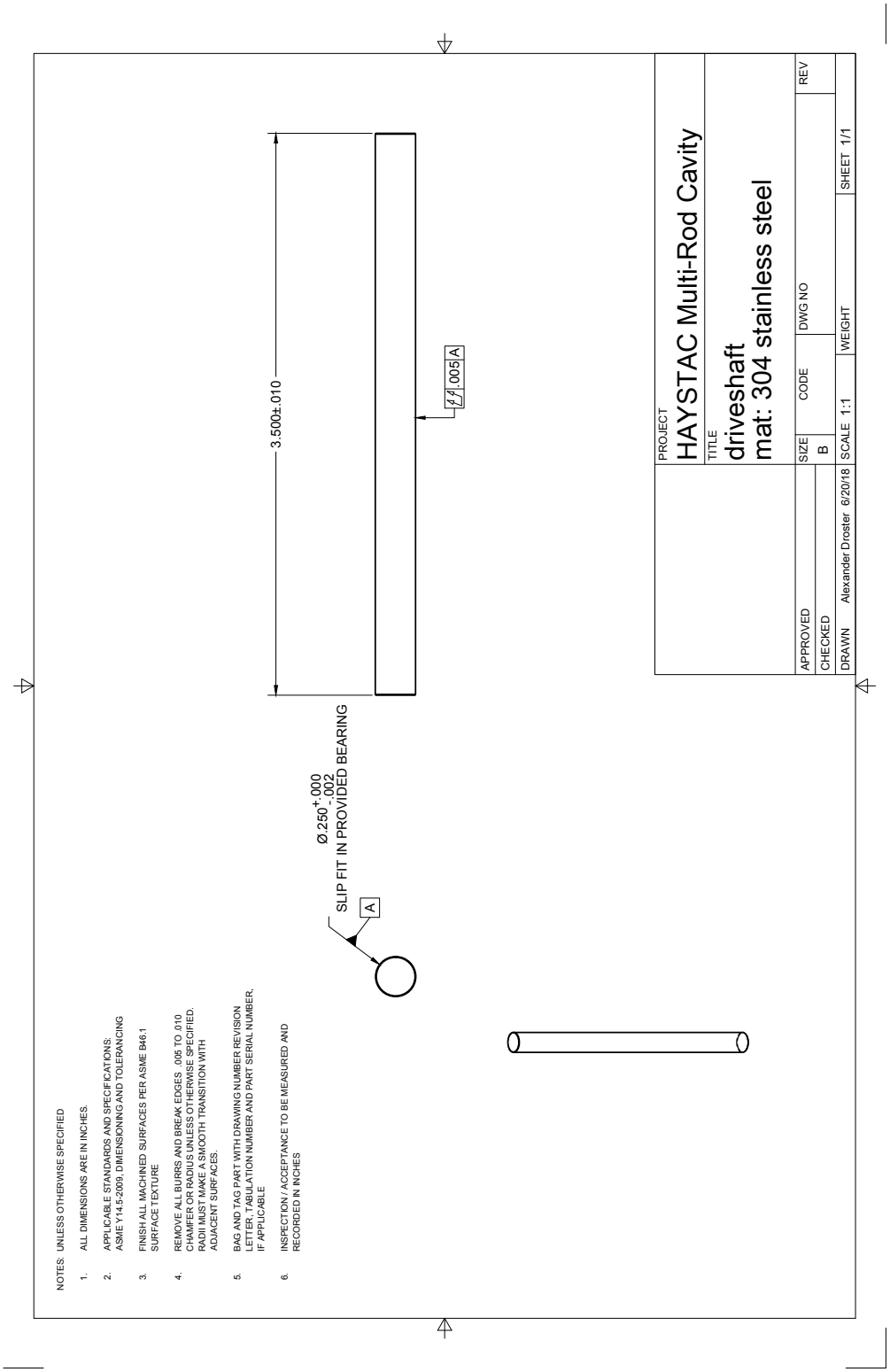

Figure B.10: CAD drawing of the driveshaft in the seven-rod cavity.